

ALMA MATER STUDIOURUM  
UNIVERSITÀ DI BOLOGNA

---

---

FACOLTÀ DI SCIENZE MATEMATICHE, FISICHE E NATURALI  
DIPARTIMENTO DI ASTRONOMIA

DOTTORATO DI RICERCA IN ASTRONOMIA - CICLO XX (2004–2007)

**Properties of gas and  
dark matter in X-ray galaxy clusters with  
Sunyaev Zel'dovich measurements**

TESI DI DOTTORATO  
DI

**Andrea Morandi**

RELATORE: **Ch.mo Prof. Lauro Moscardini**

COORDINATORE: **Ch.mo Prof. Lauro Moscardini**

CO-RELATORE: **Dr. Stefano Etori**

---

---

SCUOLA DI DOTTORATO IN SCIENZE MATEMATICHE, FISICHE E ASTRONOMICHE  
SETTORE SCIENTIFICO DISCIPLINARE: AREA 02 - SCIENZE FISICHE  
FIS/05 ASTRONOMIA E ASTROFISICA



*Alla mia Famiglia*



# Contents

<b>INTRODUCTION</b>	<b>1</b>
<b>1 Galaxy cluster formation</b>	<b>5</b>
1.1 Understanding galaxy cluster formation . . . . .	5
1.2 The formation of structures . . . . .	7
1.2.1 Linear evolution: the Jeans theory . . . . .	7
1.2.2 The perturbation spectrum . . . . .	9
1.2.3 Non-linear evolution: the cluster formation . . . . .	10
1.3 Current results on cosmology . . . . .	13
<b>2 Clusters of galaxies</b>	<b>15</b>
2.1 Introduction . . . . .	15
2.2 Optical properties of clusters . . . . .	17
2.3 X-ray properties of clusters . . . . .	18
2.3.1 Physical Properties of Hot Diffuse Plasma . . . . .	19
2.3.2 Thermal emission in the ICM . . . . .	20
2.3.3 Hydrostatic equilibrium in ICM . . . . .	22
2.3.4 The $\beta$ -Model for ICM Distribution . . . . .	22
2.3.5 Cooling in the ICM . . . . .	23
2.4 The Sunyaev-Zel'dovich effect . . . . .	25
2.5 Methods to estimate galaxy cluster mass . . . . .	27
2.5.1 The hydrostatic equilibrium equation . . . . .	27
2.5.2 The self-similar scaling . . . . .	28
2.6 An overview of Chandra and CBI . . . . .	29

2.6.1	The Chandra X-ray Observatory . . . . .	29
2.6.2	The Cosmic Background Imager . . . . .	31
<b>3</b>	<b>X-ray and Sunyaev-Zel'dovich scaling relations in galaxy clusters</b>	<b>33</b>
3.1	Introduction . . . . .	33
3.2	The dataset . . . . .	35
3.2.1	Data reduction . . . . .	35
3.2.2	Spatial and spectral analysis . . . . .	36
3.2.3	Spectral deprojection analysis . . . . .	39
3.2.4	Determination of the X-ray properties . . . . .	41
3.2.5	Determination of the Sunyaev-Zel'dovich properties . . . . .	43
3.3	The X-ray and SZ scaling relations: theory and fitting procedure . . . . .	44
3.3.1	The scaling relations in the self-similar model . . . . .	44
3.3.2	Fitting the scaling relations . . . . .	46
3.3.3	On the evolution of the scaling relations . . . . .	47
3.4	Discussion of the results . . . . .	47
3.4.1	The X-ray scaling relations . . . . .	50
3.4.2	The scaling relations involving the SZ effect . . . . .	53
3.5	Conclusions . . . . .	57
<b>4</b>	<b>Entropy profiles in X-ray luminous galaxy clusters at <math>z &gt; 0.1</math></b>	<b>61</b>
4.1	INTRODUCTION . . . . .	61
4.2	The dataset and the analysis . . . . .	64
4.2.1	Cooling core and Non-cooling core clusters . . . . .	65
4.2.2	On the gas entropy profile . . . . .	66
4.3	Entropy and temperature distribution . . . . .	68
4.3.1	The entropy-temperature relation . . . . .	68
4.3.2	Properties of the entropy profiles . . . . .	69
4.3.3	Gas and dark matter temperature profiles . . . . .	73
4.3.4	Relations between gas entropy and metallicity . . . . .	75
4.4	Discussion . . . . .	76
4.4.1	Preheating models . . . . .	78

4.4.2	Heating models . . . . .	79
4.4.3	Cooling models . . . . .	79
4.5	Summary and conclusions . . . . .	80
<b>5</b>	<b>Bayesian inference in X-ray galaxy clusters with Sunyaev Zel'dovich measurements - Physical properties of the gas out to <math>R_{200}</math></b>	<b>83</b>
5.1	INTRODUCTION . . . . .	83
5.2	The Sunyaev-Zel'dovich effect . . . . .	85
5.2.1	Determination of the Sunyaev-Zel'dovich quantities . . . . .	85
5.2.2	Why to study the outskirts through interferometric Sunyaev-Zel'dovich data? . . . . .	85
5.3	Bayesian inference . . . . .	87
5.3.1	The Bayes theorem . . . . .	87
5.3.2	Model fitting: the MCMC algorithm . . . . .	89
5.4	The dataset and analysis . . . . .	92
5.4.1	The prior: a X-ray analysis only . . . . .	93
5.4.2	The likelihood: a joint X-ray+SZ analysis . . . . .	94
5.4.3	Gas properties in the outskirts . . . . .	96
5.4.4	Constraints on the cosmology/geometry . . . . .	97
5.4.5	The unnormalized posterior: model fitting . . . . .	97
5.5	Application to mock clusters . . . . .	98
5.6	Results on the properties of the ICM . . . . .	99
5.6.1	Recovering the physical properties: prior versus posterior comparison . . . . .	99
5.6.2	Physical properties in the outskirts . . . . .	101
5.7	Summary and conclusions . . . . .	102
	<b>CONCLUSIONS</b>	<b>104</b>
<b>A</b>		<b>109</b>
A.1	Spectral deprojection technique . . . . .	109
A.2	Determining the Effective volume . . . . .	112

---

<b>B</b>	<b>115</b>
B.1 Generating correlated random numbers in the Component-Wise Hastings sampler . . . . .	115
<b>List of Figures</b>	<b>125</b>
<b>List of Tables</b>	<b>127</b>

# INTRODUCTION

In the last few years, the modeling of the formation of structures in the Universe through hydrodynamical numerical simulations and observational studies has made significant progresses. Even though the physics of the dark matter (DM) is adequately described by gravitational forces alone, a complete understanding of the relationships between the physical properties and the observables in galaxy clusters is yet unsolved.

Clusters of galaxies correspond to the largest scale of fully collapsed and virialized structures in the Universe and provide a powerful probe of the evolution of structure formation via dynamical collapse. As the most massive bound objects known, they are the ultimate manifestations of cosmic structure building and provide the most direct evidence for dark matter and baryon mass distribution on large scale.

They are typically composed of hundreds to thousands of galaxies, embedded in an intracluster medium (ICM) at hot temperature ( $T \sim 10^8 K$ ) and with low density ( $n_{\text{gas}} \sim 10^{-3} \text{ cm}^{-3}$ ) gas. From the observational point of view, there are two main ways to obtain information on the baryons in galaxy clusters. The first and most studied one is given by the emission in the X-ray band, mainly due to the free-free interaction between electrons and ions, of the ionized plasma. The other one is constituted by the Sunyaev-Zel'dovich (SZ) effect, which is the distortion of the cosmic microwave background (CMB) black-body spectrum due to the interaction between the photons and the electrons of the gas (Sunyaev & Zeldovich, 1970; Birkinshaw, 1999).

As nowadays we are living in the golden age of the X-ray satellites, most of the observational research in this field is focused just on X-ray observations, given the large amount of data available (e.g. Snowden et al., 2008; Maughan, 2007). On the X-ray observational side, the spatial resolution of the new generation of the X-ray satellites like Chandra and XMM-Newton, with their high sensitivity and large collecting area, has allowed us to study the complex interplay of the physical processes which happen in the internal regions. X-ray observations have proved that the so-called self-similar model (Kaiser, 1986), where the gravity is the only responsible for the physical properties of galaxy clusters, is not able to describe the scaling relations of galaxy clusters (e.g. the steeper slope observed in the luminosity-temperature relation), especially for low-mass systems: this indicates that gravitational collapse is not the only process that significantly influences the formation of structures. In a similar manner observations of the gas entropy profiles in groups and clusters of galaxies, and the analysis of simulated sources with an

extra non-gravitational energy injection have suggested that we have to account for further non-gravitational feedback beyond the gravitational energy. The measurements of the gas entropy  $S$  at a fixed fraction of the virial radius showed that it is higher than the expected one from the self-similar scenario, where  $S$  should scale simply with the mean temperature of the virialized systems. Instead, an excess in the entropy, with respect to the prediction of the adiabatic model, is observed in the inner regions of groups and poor clusters at some fraction of the virial radius (labeled as entropy “floor” or “ramp”). This energetic mechanism, not referable to the gravity only, falls into three main classes: preheating, where the gas collapsing into the dark matter potential well is preheated by some sources; local heating by, e.g., AGN activity, star formation or supernovae; cooling.

The complex mutual relation between the physical processes (AGNs, cooling, galactic winds, star formation, shocks) can affect the thermal history of the gas in a significant and complex way: this is one of the most interesting challenge of the extra-galactic astrophysics, involving different aspects of the research, such as hydrodynamical simulations, observations and semi-analytical models.

Nevertheless X-ray observations are subject to several limitations: i) clusters at high redshift  $z$  suffer from the cosmological dimming of the X-ray surface brightness ( $\sim (1+z)^{-4}$ ); ii) it is only possible to observe the central cluster regions ( $\lesssim 1/3 - 1/2$  of the virial radius); iii) difficult background subtraction and local inhomogeneities (the X-ray brightness depends on the squared density) may lead to systematics in the reconstructed physical properties.

All of these problems can be overcome by studying the SZ effect. Entering the last decade of SZ observations and with the incoming instruments of new generation (ALMA, APEX, the Cosmic Background Imager 2, the South Pole Telescope), we are now in position to fully exploit the power of the SZ effect by obtaining: i) detailed images of a set of clusters to understand the intracluster medium (ICM); ii) large SZ samples of clusters to obtain statistically robust estimates of the cosmological parameters and, most importantly, iii) large untargeted SZ surveys to probe the high redshift universe. These surveys will provide a direct view of the growth of large-scale structures and will provide large catalogs of clusters that extend past  $z \sim 2$  with remarkably uniform selection functions. Thanks to the development of new microwave instruments these aspects are providing the first important results and will likely receive a significant boost in the near future.

Advantages of dealing with SZ data are: i) the linear dependence of the SZ brightness on the density; ii) independence of the SZ signal of  $z$ ; iii) the lack of contamination of interferometric SZ data from sources (like filaments) on larger scales ( $\gtrsim$  a few arcminutes) and iv) the strong dependence of the SZ brightness on the outskirts of the clusters, i.e. till the virial radius.

In the work of this Thesis, we have considered a sample of galaxy clusters to describe the properties of the X-ray and SZ signals, focusing on the determination of the physical properties of the intracluster gas and of the DM and comparing our findings with results of numerical simulations discussed in the literature. This allowed us to make comparisons with the theoretical predictions in order to test the validity of the current models of galaxy clusters and to trace out the thermal history of the gas. In particular, we concentrated

on a joint analysis of X-ray data, whose high spatial resolution is capable to resolve the cluster core, and the SZ ones, more sensitive to the cluster outer volume: this allowed us to characterize the level and the gradient of the gas density, temperature and entropy distribution on the entire cluster, out to the virial radius. These constraints can break the degeneracy between the physical models describing the thermal history of the ICM.

This Thesis is organized as follows.

- In Chapter 1 we present an introduction to the picture of galaxy cluster formation and evolution, as well as their main properties. In all these aspects, we pay particular attention to the relationships between clusters and cosmological parameters, and then on the non-linear model leading to galaxy cluster formation.
- In Chapter 2 we will provide an overview of the main properties of galaxy clusters. We will discuss the optical, X-ray and SZ properties of galaxy clusters, in particular the emission processes and the physics of the ICM. At last we will outline methods to measure the mass of the clusters.
- In Chapter 3 we provide an analysis of the scaling relations between X-ray properties and Sunyaev-Zel'dovich (SZ) parameters for a sample of 24 X-ray luminous galaxy clusters observed with Chandra and with measured SZ effect. We can compare our results with expectations from analytical models and hydrodynamical numerical simulations.
- Chapter 4 is devoted to the study of the profiles and the scaling properties of the gas entropy in the sample of galaxy clusters presented in Chapter 3. We compare the current models in literature on the extra-gravitational energy which affects the thermal history of the ICM with our measurements of the entropy, metallicity and gas+dark matter temperature profiles.
- In Chapter 5 we present a Bayesian approach to combine X-ray and Sunyaev Zel'dovich (SZ) data. We will focus on the study of the physical properties of the ICM and DM in the outskirts of the clusters out to  $R_{200}$ , well beyond the regions accessible with X-ray observations ( $\leq 0.3 - 0.5 R_{200}$ ).



# Chapter 1

## Galaxy cluster formation

This chapter aims at providing an introduction to the picture of galaxy cluster formation and evolution, as well as their main properties. We start by briefly describing some physical bases of the Friedmann models and their connections with the formation of the structures in the Universe. We will concentrate on the relationships between clusters and cosmological parameters, and then on the non-linear model leading to galaxy cluster formation.

### 1.1 Understanding galaxy cluster formation

Our current understanding of cluster evolution is a result of the cosmological model, which depends on just a few parameters. As we will see, one set of parameters ( $H_0$ ,  $\Omega_M$ ,  $\Omega_b$ ,  $\Omega_R$ ,  $\Omega_\Lambda$ , and  $w$ ) characterizes the cosmological model, which describes the overall geometry of the universe, the mean density of its contents, and how its scale changes with time, while the other ones ( $\sigma_8$  and  $n_p$ ) specify the initial spectrum of density perturbations that grew into the galaxies, clusters of galaxies, and more in general in the cosmic structures we see today. Here we define both sets of parameters and their roles in the context of the global model.

#### Global Dynamics

To characterize the expansion of the universe one uses a scale factor  $a(t)$ , which is dependent on the cosmological time. The parameter is related to the Hubble's Law

$$v = H(t)d, \tag{1.1}$$

where  $d$  is the distance between two cosmic structures and  $v$  their recession velocity, and  $H(t) = \dot{a}/a$  is the Hubble parameter.

The general development of all modern cosmological theories is based on General Relativity. More precisely the *Einstein equations* describe the relationships between the

metric of the space-time  $g_{ij}(x_k)$  with the energy-momentum tensor  $T_{ij}(x_k)$  ( $i, j=0, 1, 2, 3$ , with 0 indicating the time coordinate):

$$R_{ij} - \frac{1}{2}g_{ij}R = -\frac{8\pi G}{c^4}T_{ij}, \quad (1.2)$$

where  $R_{ij}$  is the Ricci tensor and  $R$  the Ricci scalar.

A more general description has been provided by including the *cosmological constant*  $\Lambda$  in Eq. (1.2) as well:

$$R_{ij} - \frac{1}{2}g_{ij}R - \Lambda g_{ij} = -\frac{8\pi G}{c^4}T_{ij}, \quad (1.3)$$

which arises as an integration constant and allows to obtain static solutions of the Eq. (1.2) with suitable values of  $\Lambda$ .

The energy-momentum tensor with greater relevance in cosmology is that of a perfect fluid:

$$T_{ij} = -pg_{ij} + (p + \rho c^2)U_i U_j, \quad (1.4)$$

where  $p$  is the pressure,  $\rho c^2$  is the energy density, including also the rest-mass energy, and  $U_k$  is the four-velocity of the fluid.

Since the universe appears homogeneous and isotropic on very large scales, the Einstein equations yield the Friedmann-Lemaitre model of the universe, in which

$$\frac{\ddot{a}}{a} = -\frac{4}{3}\pi G \left( \rho + \frac{3p}{c^2} \right), \quad (1.5)$$

where  $\rho(t)c^2$  is the mean density of mass-energy and  $p(t)$  is the pressure owing to that energy density. The adiabatic expansion of the Universe requires that

$$d(\rho a^3) = -3\frac{p}{c^2}a^2 da. \quad (1.6)$$

Assuming that the equation of state has the form  $p = w\rho c^2$ , then density changes with the expansion as  $\rho \propto a^{-3(1+w)}$ . The cosmological redshift  $z$  is related to the scale factor  $a(t)$  of the expansion of the universe in such a way that  $a = (1+z)^{-1}$ : with this definition  $a(t) = 1$  at the present time  $t_0$  (hereafter the subscript '0' refers to quantities defined at present time). Then resolving equations (1.5) and (1.6), for a single mass-energy component with a constant value of  $w$ , we therefore have

$$\left( \frac{\dot{a}}{a} \right)^2 = H_0^2 [\Omega_0(1+z)^{3(1+w)} + (1-\Omega_0)(1+z)^2], \quad (1.7)$$

where  $\Omega_0$  is the current energy density  $\rho_0$  in units of the current critical density  $\rho_{\text{cr}0} = 3H_0^2/8\pi G$ .

The global expansion can be influenced by several kinds of components of the universe. The energy density  $\rho_R c^2$  in photons and relativistic particles contributes a pressure corresponding to  $w = 1/3$ . Einstein's cosmological constant acts like an energy density  $\rho_\Lambda c^2$  that remains constant while the universe expands and therefore gives a pressure

corresponding to  $w = -1$ . We can account for non-relativistic particles as well, with a mass density  $\rho_M$  and they contribute a pressure corresponding to  $w \simeq 0$ . Including each of these components, Eq. (1.7) then reads:

$$H^2(z) = \left(\frac{\dot{a}}{a}\right)^2 = H_0^2[\Omega_M(1+z)^3 + \Omega_R(1+z)^4 + \Omega_\Lambda + (1-\Omega_0)(1+z)^2] \quad (1.8)$$

where  $\Omega_x$  is the current mass-energy density in component  $x$  in units of  $\rho_{\text{cr}0}$  and  $\Omega_0 = \Omega_M + \Omega_R + \Omega_\Lambda$ . The value of  $\Omega_x$  at an arbitrary redshift is given by  $\Omega_x(z) = \Omega_x(1+z)^{3(1+w)}[H(z)/H_0]^{-2}$ .

Each of these mass-energy density parameters  $\Omega_M, \Omega_R, \Omega_\Lambda$  can be splitted in further components. The matter density parameter  $\Omega_M$  consists of a contribution  $\Omega_b$  from baryons and a contribution  $\Omega_{\text{CDM}}$  from non-baryonic cold dark matter. The radiation density parameter  $\Omega_R$  includes contributions from the photons of the microwave background,  $\Omega_{\text{CMB}}$ , and from relativistic neutrinos produced in the Big Bang,  $\Omega_\nu$ . The mass-energy density related to the cosmological constant  $\Omega_\Lambda$  can be generalized with the dark-energy term  $\Omega_\Lambda(1+z)^{3(1+w)}$ , in order to attempt to measure the value of  $w$ .

## 1.2 The formation of structures

One of the main goal of cosmology is the understanding of the formation of the structures that we observe at the present time. The Jeans theory of gravitational instability is able to explain the growth of the primordial linear density perturbations, leading to the formation of stars, galaxies and clusters of galaxies.

The small fluctuations of density are expected to be originated in the first instants after the big bang by quantum oscillations of the scalar field driving the expansion in the inflationary epoch. The CMB observations measured the amplitude of such density perturbations in the primordial Universe and their gravitational amplification can be linked to the formation of the large scale structures (LSS) of the Universe. According to the cold dark matter scenario of the hierarchical formation of the cosmic structures, galaxy clusters form from perturbations in the density field. Small subclumps of matter are the first pieces of the cluster to deviate from the Hubble flow and undergo gravitational relaxation because the density perturbations have larger amplitudes on smaller mass scales. These small structures then merge so as to produce larger and larger structures as perturbations on larger mass scales reach the non-linear regime, where the linear density perturbations theory cannot be applied anymore. In this picture stars and galaxies are the first objects which form, while larger structures like galaxy clusters grow through coalescence of smaller objects.

### 1.2.1 Linear evolution: the Jeans theory

We describe now the basis of the Jeans theory that is able to explain the growth of small density fluctuations in the linear regime. In this picture, the linear perturbations of an

uniform fluid are able to increase when the gravity starts to dominate on the fluid pressure.

The basic laws that describe the dynamics of a self-gravitating fluid are the continuity, the Euler and the Poisson equations:

$$\frac{\partial \rho}{\partial t} + \vec{\nabla} \cdot (\rho \vec{u}) = 0 \quad (1.9a)$$

$$\frac{\partial \vec{u}}{\partial t} + (\vec{u} \cdot \vec{\nabla}) \vec{u} = -\frac{1}{\rho} \vec{\nabla} p - \vec{\nabla} \Phi \quad (1.9b)$$

$$\nabla^2 \Phi = 4\pi G \rho, \quad (1.9c)$$

where  $\rho$ ,  $\vec{u}$  and  $p$  are the density, the velocity and the pressure of the fluid element and  $\Phi$  is the gravitational potential. If we neglect the effects of thermal conduction and viscosity, i.e. we are assuming the conservation of entropy per unit of mass  $S$ , we have a further continuity equation for the entropy:

$$\frac{\partial S}{\partial t} + \vec{u} \cdot \vec{\nabla} S = 0. \quad (1.10)$$

If now we introduce linear perturbations  $\delta$ ,  $\vec{v}$ ,  $\phi$ ,  $dp$  and  $dS$  to the physical variables  $\rho$ ,  $u$ ,  $\Phi$ ,  $p$  and  $S$ , respectively, so that

$$\rho = \rho_0 + \delta\rho_0 = \rho_0(1 + \delta) \quad (1.11a)$$

$$\vec{u} = \vec{u}_0 + \vec{v} \quad (1.11b)$$

$$\Phi = \Phi_0 + \phi \quad (1.11c)$$

$$p = p_0 + dp \quad (1.11d)$$

$$S = S_0 + dS, \quad (1.11e)$$

where the index '0' represents the zeroth-order solutions, solving the equations (1.9) and (1.10) we obtain the *dispersion equation*:

$$\ddot{\delta} + 2\frac{\dot{a}}{a}\dot{\delta} + (v_s^2 k^2 - 4\pi G \rho_0)\delta = 0, \quad (1.12)$$

being  $v_s$  the sound speed defined as  $v_s^2 \equiv (\partial\rho/\partial p)_S$ . Equation (1.12) represents the evolution with time of the density contrast  $\delta$  as a function of their wavelength. More precisely, if we can define the *Jeans length* as

$$\lambda_J \equiv v_s \left( \frac{\pi}{G\rho_0} \right)^{1/2}, \quad (1.13)$$

we have that for fluctuations with  $\lambda < \lambda_J$  the pressure term  $\propto v_s^2$  in equation (1.12) dominates and we have oscillating solutions, while for  $\lambda > \lambda_J$  the gravity term  $\propto 4\pi G\rho_0$  dominates leading to gravitational instability.

Under these hypotheses, in the case of  $\lambda \gg \lambda_J$ , when the DM component starts to dominate driving the growth of the density fluctuations we have two solutions for Eq. (1.12):

$$\delta_-(t) \propto t^{-1} \quad (1.14)$$

$$\delta_+(t) \propto t^{2/3} . \quad (1.15)$$

The first solution can be neglected because it vanishes with time. The second one represents the growing amplitudes of the fluctuations in this regime, leading to the hierarchical coalescence of the cosmic structures.

### 1.2.2 The perturbation spectrum

At any given position  $\vec{x}$  of space it is possible to define the density contrast (see Sect. 1.2.1) as

$$\delta(\vec{x}) \equiv \frac{\rho(\vec{x}) - \langle \rho \rangle}{\langle \rho \rangle} , \quad (1.16)$$

being  $\langle \rho \rangle$  is the average density, with Fourier components

$$\tilde{\delta}(\vec{k}) \equiv \int \delta(\vec{x}) e^{i\vec{k}\cdot\vec{x}} d^3\vec{x} , \quad (1.17)$$

where  $\vec{k}$  is the wavevector.

If we assume that the Universe is homogeneous and isotropic on sufficiently large scales (e.g.  $\gtrsim 100$  Mpc), which means that there is not any preferential position or direction (the Cosmological Principle),  $\delta(\mathbf{x})$  can be characterized by an isotropic power spectrum

$$P(k) \equiv \langle |\delta_k|^2 \rangle . \quad (1.18)$$

If  $\delta(\mathbf{x})$  is also a Gaussian random field, then  $P(k)$  is a complete statistical description of the initial perturbation spectrum.

The physical meaning of  $P(k)$  becomes clearer if we assume it has a power-law form

$$P(k) = Ak^n , \quad (1.19)$$

with  $n$  usually called *spectral index*, and we consider the variance in mass within identical volume elements corresponding to the length scale  $k^{-1}$ . If we consider the top-hat window function  $W(x)$  defined as having the constant value of 1 for  $x \leq 1$  and 0 otherwise, the mass perturbation smoothed over the above window is

$$\frac{\delta M}{M}(\mathbf{r}) = \int \delta(\mathbf{x}) W(|\mathbf{x} - \mathbf{r}|) d^3x . \quad (1.20)$$

Using the convolution theorem, we can then write the variance  $\sigma^2 \equiv \langle |\delta M/M|^2 \rangle$  on the mass scale as a function of the Fourier transform  $W_k$  of  $W(x)$ :

$$\sigma^2 = \frac{1}{(2\pi)^3} \int P(k) |W_k|^2 d^3k . \quad (1.21)$$

The quantity  $\sigma^2$  does not depend on spatial positions but on time, since  $\tilde{\delta}(k)$  evolves with time, therefore it represents a measure of the amplitude of the perturbations but it does not provide any information about their spatial structure. The convergence of the variance in equation (1.21) requires that  $n > -3$  for  $k \rightarrow 0$  and  $n > -3$  for  $k \rightarrow \infty$ .

The variance in mass on scale  $k$  for a power-law perturbation spectrum is therefore  $\sigma^2 \propto k^{n+3}$ , because the top-hat window function  $W(x)$  smooths out just the perturbations with wave-number  $k \gg x^{-1}$ . Thus, the typical mass fluctuation on mass scale  $M \propto k^{-3}$  is

$$\frac{\delta M}{M} \propto M^{-\frac{n+3}{6}} . \quad (1.22)$$

For what concerns the value  $A$  of the power spectrum normalization in equation (1.19), it can be demonstrated that it is proportional to the variance of the density contrast on a given scale. As a reference, it is usual to adopt  $\sigma_8$  defined as

$$\sigma_8^2 \equiv \frac{1}{2\pi^2} \int_0^\infty P(k) |\hat{W}(kR_8)|^2 k^2 dk , \quad (1.23)$$

where  $R_8 = 8h^{-1}$  Mpc. The scale of  $8 h^{-1}$  Mpc has been chosen to take into account the results of Davis & Peebles (1983) that found that at this radius the variance of galaxy counts is equal to unity.

### 1.2.3 Non-linear evolution: the cluster formation

The Jeans theory described in Section 1.2.1 is valid only for  $|\delta| \ll 1$ , while the structures observed nowadays correspond to overdensities  $|\delta| \gg 1$ , for example a cluster of galaxies corresponds to a value of  $\delta$  of several hundreds.

A full understanding of the details of how hierarchical merging process leads to the formation of virialized structures such as galaxies and clusters of galaxies, requires numerical simulations, but analytical models of cluster formation allow to address several important aspects of this picture. Here we will discuss how a cluster would grow from a spherically symmetric mass perturbation and then we will refine the details of that simplified approach by considering the results from numerical simulations.

#### The spherical collapse

The simplest approach to follow the non-linear evolution of the density perturbations is based on the spherical collapse model and its predictions for the properties of galaxy clusters. In this model the matter that goes on to form a cluster begins as a low-amplitude spherical density perturbation with density contrast in the range  $0 < \delta_p \ll 1$  and expanding with the background in such a way that the peculiar velocity at the edge of the perturbation is null. The perturbation's gravitational pull slows the expansion of that matter, eventually stopping and reversing the expansion. So, after reaching the maximum expansion (turn-around), the perturbation detaches itself from the general Hubble expansion and then recollapses, leading to the gravitational collapse of the matter

at the center of the perturbation. A cluster of matter then forms at the center of the perturbation.

The accretion process in real clusters is not spherical. Instead, gravitational forces between infalling clumps of matter yield a gravitational potential that depends on the time, leading at the virialization time  $t_{\text{vir}}$  a state of virial equilibrium in which the total kinetic energy  $K$  is related to the total gravitational potential energy  $U$  through the equation

$$U + 2K = 4\pi P r^3, \quad (1.24)$$

where  $P$  is the effective pressure owing to infalling matter at the boundary  $r$  of the collapsed system. Setting  $P$  to zero yields the usual form of the virial theorem  $E = K + U = -K$  for gravitationally bound systems. This process, known as “violent relaxation” (Lynden-Bell, 1967), leads to a state of the Maxwellian velocity distribution in which the temperature is proportional to the particle mass.

At the turn-around point, the perturbation has no kinetic energy, so that the total energy is

$$E_m = U = -\frac{3}{5} \frac{GM^2}{R_m}, \quad (1.25)$$

where we have used the expression for the potential energy of a uniform spherical density field of radius  $R_m$  and total mass  $M$ . In a similar manner, the total energy at the virialization is

$$E_{\text{vir}} = \frac{U}{2} = -\frac{13}{25} \frac{GM^2}{R_{\text{vir}}}. \quad (1.26)$$

Therefore, the condition of energy conservation in a dissipationless collapse gives  $R_m = 2R_{\text{vir}}$  for the relation between the radii at turn-around and at virial equilibrium.

The spherical top-hat model has actually led to several different definitions for the virial radius of a cluster. If one assumes that all the mass in the original top-hat perturbation ends up within  $r_{\text{ta}}/2$ , then the mass density in that region is  $6M/\pi r_{\text{ta}}^3$ . In a matter-dominated universe with zero dark energy, this density is equal to  $\Delta_v = 8\pi^2/(Ht)^2$  times the critical density  $\rho_{\text{cr}} \equiv 3H^2/8\pi G$ . Thus, for a flat, matter-dominated universe in which  $Ht = 2/3$ , the mean density of a perturbation that has just collapsed is taken to be  $18\pi^2 \approx 178$  times the critical density. A useful approximation for  $\Delta_v$  in a flat universe with a non-zero cosmological constant ( $w = -1$ ) is

$$\Delta_v = 18\pi^2 + 82[\Omega_M(z) - 1] - 39[\Omega_M(z) - 1]^2 \quad (1.27)$$

(Bryan & Norman, 1998). However, even if the above picture in which a cluster would grow from a spherically symmetric mass perturbation is able to describe many general properties of halo formation, this simple model does not fully reproduce the observed properties of galaxy clusters, being neglected different effects like merging, mass dissipation and other processes that affect the baryons during the collapse.

Because it is not easy to determine the outer radius of a real cluster, one pragmatic definition of the virial radius is then the radius  $r_v$  within which the mean matter density is  $\Delta_v \rho_{\text{cr}}$ . Another definition is that to consider  $\Delta_v = 200$ , i.e. the scale radius  $r_{200}$  within

which the mean matter density is  $200\rho_{\text{cr}}$ , neglecting its dependence on the cosmological parameters and on the redshift.

By an observational point of view it is easier to observe the properties of a cluster in regions where the density contrast is higher ( $\lesssim 1/2r_v$ ). The easiest way to link observations to theoretical models is through definitions taking the mass of a cluster to be  $M_\Delta$ , the amount of matter contained in a spherical region of radius  $r_\Delta$  whose mean density is  $\Delta \cdot \rho_{\text{cr}}$ . So observers often prefer to raise that threshold from  $\Delta_v$  given by Eq. (1.27) to  $\Delta = 2500$  ( $r_{2500} \approx 1/4r_v$ ) or  $\Delta = 500$  ( $r_{500} \approx 1/2r_v$ ).

### Cluster Mass Profiles

A fundamental question is the distribution of matter in bound systems (galaxies, galaxy clusters, dark matter halos) that form in an expanding universe. Observations of galaxy clusters have long shown that their velocity dispersion is roughly constant with distance from the cluster center, implying an underlying mass-density profile  $\rho_M(r) \propto r^{-2}$ . The simplest analytical cluster model consistent with such a density profile is the singular isothermal sphere, in which the velocity dispersion  $\sigma_v$  is constant and isotropic at every point, and the dark matter density  $\rho_{\text{DM}} \propto (1 + (r/r_c)^2)^{-3/2}$  in the internal regions and  $\rho_{\text{DM}} \propto r^{-2}$  in the outskirts.

Observers have widely used the King profile as a reasonable analytical approximation of the isothermal sphere in the internal regions accessible to the X-ray observations. This parameterization was successful for a long time, given the strict connection with the so called  $\beta$ -model (Cavaliere & Fusco-Femiano, 1976), which aimed at representing the distribution of isothermal gas sitting in hydrostatic equilibrium within a King-like potential: within such a DM profile, it is possible to show that there is a relationship between the kinetic energy  $\sigma_v^2$  of any tracer of the gravitational potential (e.g. galaxies) and the thermal energy of the gas,  $k_B T$ . Therefore this model was useful for making analytical estimates of cluster properties.

Nevertheless, numerical simulations of cluster formation have indicated that the density profiles of dark-matter halos is shallower (steeper) than isothermal at small (steeper) radii. Most of these profiles are referable to the so called  $(\alpha, \beta, \gamma)$  model, in which 2–5 parameters control a double power law behaviour:

$$\rho_{\text{DM}}(r) = \rho_s 2^{(\beta-\gamma)/\alpha} \left(\frac{r}{r_s}\right)^{-\gamma} \left[1 + \left(\frac{r}{r_s}\right)^\alpha\right]^{\alpha\gamma(\gamma-\beta)/\alpha}, \quad (1.28)$$

where  $\rho_s$  is the density at the scale radius,  $r_s$ , which determines the transition region between the inner and outer power law, having slopes of  $-\gamma$  and  $-\beta$ , respectively. The parameter  $\alpha$  controls the sharpness of the transition. Setting  $(\alpha, \beta, \gamma)$  equal to fixed values we obtain well known models in literature, such as King model (King, 1962) for  $(\alpha, \beta, \gamma)=(2,3,0)$ ; NFW model (Navarro et al., 1997), for  $(\alpha, \beta, \gamma)=(1,3,1)$ ; the RTM model (Rasia et al., 2004), for  $(\alpha, \beta, \gamma)=(1,2.5,1)$ ; the generalized NFW model for  $(\alpha, \beta, \gamma)=(1,3,\gamma)$  with an outer slope of  $-3$  and an inner slope of  $-\gamma$ .

Measurements of the inner slope  $\gamma$  is one the most interesting challenge of the observations, since the cuspsness of dark-matter density profiles at  $r = 0$  is one of the

critical tests of the cold dark matter (CDM) paradigm for structure formation (see Navarro et al., 2004, and references therein).

The transition of the density profile from shallow to steep can be characterized by considering the concentration parameter  $c = r_b/r_s$ , which links the bounding radius  $r_b$  (e.g.  $r_{200}$ ) of the cluster to  $r_s$ . Typical concentration parameters for simulated clusters are in the range  $c \sim 4 - 10$  with a mild dependence on the cluster mass: lower-mass objects tend to have higher halo concentrations because they formed earlier in time, when the overall density of the universe was greater (Navarro et al., 1997; Bullock et al., 2001).

### 1.3 Current results on cosmology

The overall cosmological model depends on just a few parameters. As already said, one set of parameters ( $H_0$ ,  $\Omega_M$ ,  $\Omega_b$ ,  $\Omega_R$ ,  $\Omega_\Lambda$ , and  $w$ ) specifies the global cosmological model, which describes the overall geometry of the universe, the mean density of its contents, and how its scale changes with time, while the other one ( $\sigma_8$  and  $n_p$ ) governs the initial density perturbation spectrum.

Current observational data suggest as a favorite scenario the so-called “*concordance*”  $\Lambda$ -Cold Dark Matter ( $\Lambda$ CDM) model, to characterize cold dark matter with a cosmological constant. In this picture the Universe is flat with the energy density at the present epoch dominated by a cosmological constant and the remaining fraction mainly due to non-baryonic, non-collisional dark matter with low primordial velocity dispersion. The fraction of density due to standard baryonic matter  $\Omega_b$  is only of few percent.

In the range of redshift  $10^4 \gtrsim z \gtrsim 10^3$  the DM component dominates driving the growth of the density fluctuations up to the epoch of recombination ( $z \sim 10^3$ ), when they become visible as gas temperature fluctuations imprinted in the CMB anisotropies  $\Delta T/T_{\text{CMB}} \approx 10^{-5}$ . In this scenario small objects form first because the typical perturbations that survive to the effect of free-streaming correspond to masses of the order of  $M \simeq M_J(z_{\text{rec}}) \simeq 10^5 M_\odot$ , thus to the typical scales of protogalaxies: bigger structures such as galaxy clusters form then hierarchically through merging of smaller objects.

The dark energy component became important in driving the expansion at  $z \lesssim 0.5$  and it has the effect of accelerating the expansion of the Universe. This kind of energy can be associated to the presence of a cosmological constant  $\Lambda \neq 0$ , which corresponds to  $w = -1$  in the equation of state  $p = w\rho c^2$ . Although the physical motivation of this constant is still far from being wholly understood, the presence of a cosmological constant is believed to be the most realistic explanation of current observational results.

The concordance  $\Lambda$ CDM cosmology is currently supported by many observations which allow a precise estimate of the cosmological parameters. These data include results from the  $d_L - z$  relation of high-redshift supernovae (see, e.g., Astier et al., 2006; Wood-Vasey et al., 2007), weak lensing (see, e.g., Heymans et al., 2005; Massey et al., 2005; Hoekstra et al., 2006) and galaxy clustering (see, e.g., Tegmark et al., 2006; Sánchez et al., 2006), CMB anisotropies observations made by the *Wilkinson Microwave Anisotropy Probe* satellite (*WMAP*, Spergel et al., 2003; Spergel et al., 2007).

**Table 1.1.** Main cosmological parameters as estimated by Spergel et al. (2007) using the data of the WMAP satellite together with other results from CMB data, galaxy clustering, SN-Ia and weak lensing analysis. These values have been obtained assuming a flat  $\Lambda$ CDM model. Errors correspond to  $1\sigma$ .

$\Omega_m$	$\Omega_\Lambda = 1 - \Omega_m$	$10^2\Omega_b h^2$	$h$	$\sigma_8$	$n_s$
$0.268 \pm 0.018$	$0.732 \pm 0.018$	$2.186 \pm 0.068$	$0.704^{+0.015}_{-0.016}$	$0.776^{+0.031}_{-0.032}$	$0.947 \pm 0.015$

We quote in Table 1.1 the estimates of the main cosmological parameters coming from WMAP together other observational results (Spergel et al., 2007).

In this Thesis we have assumed a flat concordance  $\Lambda$ CDM cosmology, with matter density parameter  $\Omega_{0m} = 0.3$ , cosmological constant density parameter  $\Omega_\Lambda = 0.7$ , and Hubble constant  $H_0 = 70 \text{ km/s/Mpc}$ , compatible to the values shown in this table.

## Chapter 2

# Clusters of galaxies

**T**his chapter aims at providing an overview of the main properties of galaxy clusters. After a brief summary about the historical studies on the clusters, we will discuss their optical properties. In the central part we will focus on the X-ray properties of galaxy clusters, in particular on the emission processes and on the physics of the ICM. At last we will outline methods to measure the mass of the clusters.

### 2.1 Introduction

As we discussed in the previous chapter, clusters of galaxies represent the largest virialized structures in the present universe, formed at relatively late times. The hierarchical scenario provides a picture in which the primordial density fluctuations generate proto-structures which are then subjected to gravitational collapse and mass accretion, producing larger and larger systems. Clusters of galaxies probe the high-density tail of the cosmic density field and their number density is highly sensitive to specific cosmological scenarios (e.g. Press & Schechter, 1974; Kofman et al., 1993; Bahcall & Cen, 1993). The space density of clusters in the local universe has been used to measure the amplitude of density perturbations on  $\sim 10$  Mpc scales.

Clusters form through the collapse of cosmic matter over a region of several megaparsecs. Cosmic baryons, which represent approximately 10–15% of the mass content of the Universe, follow the dynamically dominant dark matter during the collapse. They fall into the gravitational potential of the cluster dark matter halo so formed, while the collapse and the subsequent adiabatic compression and shocks heat the intra-cluster medium (ICM). A thin hot gas permeating the cluster gravitational potential well is then formed, reaching temperatures of several  $10^7$  K, becomes fully ionized and, therefore, emits via thermal bremsstrahlung in the X-ray band. Typically, clusters of galaxies have total masses which exceed  $5 \times 10^{14} M_{\odot}$ , contributed for  $\sim 85\%$  by dark matter,  $\sim 10\%$  by ICM and  $\sim 5\%$  by galaxies (e.g. Allen & Fabian, 1998).

Historically, clusters of galaxies were first identified by their optical properties as large concentrations in the projected galaxy distribution (e.g. Zwicky et al., 1966; Zwicky &

Kowal, 1968), containing hundreds to thousands galaxies, over a region of the order of  $\sim 1$  Mpc. The first observations showed that such structures are associated with deep gravitational potential wells.

Afterwards, observations of clusters in the X-ray band have been an efficient method of identification in the survey, being the X-ray luminosity much more pronounced in regions where the density contrast with respect to  $\rho_{\text{cr}}$  is higher, i.e. in the gravitational potential well of the clusters. The X-ray luminosity is also a good probe of the depth of the cluster gravitational potential and, moreover, retains information about non-radiative processes, like non-gravitational heating due to energy injection from supernovae, AGN, star formation or galactic winds, which characterize the physics of the gas besides its gravitational energy, tracing out its thermal history. For these reasons most of the studies based on clusters have used X-ray selected samples. X-ray studies of galaxy clusters provide: (1) by a cosmological point of view, an efficient way of mapping the overall structure and evolution of the Universe and (2) a robust means to understand their internal structure and the thermal history of cosmic baryons.

The first X-ray observations of clusters obtained by the *UHURU* satellite (e.g. Giacconi et al., 1972) and then by the *Einstein* satellite clearly indicated that the space between the galaxies is filled by hot X-ray emitting gas (e.g. Jones & Forman, 1984). X-ray cluster studies made substantial progress at the beginning of the 90s with the advent of new X-ray missions. Firstly, hundreds of new clusters have been discovered through the all-sky survey conducted by the *ROSAT* satellite. Afterwards, the *ASCA* and *Beppo-SAX* satellites have revealed the first view of the thermal structure of the ICM, involving star formation processes and energy feedback from supernovae. Nowadays, the spatial resolution of the new generation of the X-ray satellites like *Chandra* and *XMM-Newton*, with their high sensitivity and large collecting area, has allowed us to unveil the complex interplay of the physical processes which happen in the internal regions, casting new light on the interplay between the complex physics of the hot ICM and detailed processes of star formation associated with cool baryons.

Hot gas in clusters can also be observed through its effects on the cosmic microwave background. The background itself has a virtually perfect blackbody spectrum. Soon after the discovery of this background radiation, Sunyaev & Zeldovich (1970) predicted that hot gas in clusters of galaxies would distort the CMB spectrum by Compton scattering, now known as the Sunyaev-Zel'dovich (SZ) effect. Cosmological applications of the thermal SZ effect in clusters benefit greatly from the fact that the effect is independent of distance, unlike optical and X-ray surface brightness. Thus, a dedicated SZ cluster survey would find clusters efficiently out to arbitrarily high redshifts.

Two decades after this prediction, there were only a few marginal detections, but many clusters were detected at high significance in the following decade (Birkinshaw, 1999; Carlstrom et al., 2002). Entering the last decade of SZ observations and with the incoming instruments of new generation (ALMA, APEX, the Cosmic Background Imager 2, the South Pole Telescope), we are now in position to fully exploit the power of the SZ effect by obtaining i) detailed images of a set of clusters to understand the intracluster medium; ii) large SZ samples of clusters to determine statistically robust estimates of

the cosmological parameters and, most importantly, iii) large untargeted SZ surveys to probe the high redshift universe. These surveys will provide a direct view of the growth of large-scale structures and will provide large catalogs of clusters that extend past  $z \sim 2$  with remarkably uniform selection functions.

## 2.2 Optical properties of clusters

Historically, a great effort were made in studying clusters of galaxies by their optical properties. The galaxy distribution on the sky is not homogeneous: in fact, galaxies tend to clump together in clusters. Clusters of galaxies typically contain hundreds of galaxies, spread over a region of the order of  $\sim 1$  Mpc.

Abell (1958) provided the first extensive, statistically complete sample of rich galaxy clusters in the northern areas of the sky. Based on purely visual inspection, clusters were identified as enhancements in the galaxy surface density and were characterized by their richness and estimated distance. Afterwards, some further cluster catalogs became available (e.g. Zwicky & Kowal, 1968; Gunn et al., 1986).

The population of galaxies in clusters is substantially different from that in the field (e.g. Dressler, 1980): with respect to the field distribution, clusters are richer in ellipticals and spheroidals, and poorer in spirals. Rich clusters are often dominated by a single, central cD galaxy. Different cluster properties have been used to construct morphological classification systems which define a sequence of clusters running from regular to irregular. Regular clusters are almost spherical and symmetric, and have a core with a high concentration of galaxies at the center. They do not show strong evidence of substructures. On the contrary, irregular clusters have little symmetry or central concentration, and often show significant hints of substructures. This suggests that regular clusters are dynamically more evolved and relaxed than irregular clusters.

The first optical observations showed that such structures are associated with deep gravitational potential wells, containing galaxies with a typical velocity dispersion along the line-of-sight of  $\sigma_v \sim 10^3 \text{ km s}^{-1}$ . The crossing time for a cluster of size  $R_V$  can be defined as

$$t_{\text{cr}} = \frac{R_V}{\sigma_v} \simeq 1 \left( \frac{R_V}{1 \text{ Mpc}} \right) \left( \frac{\sigma_v}{10^3 \text{ km s}^{-1}} \right)^{-1} \text{ Gyr}. \quad (2.1)$$

Therefore, in a Hubble time,  $t_H \simeq 10 h^{-1} \text{ Gyr}$ , clusters have enough time in their internal regions (on scale  $\lesssim 1 \text{ Mpc}$ ) to dynamically relax, while in surrounding environment on scale of  $\sim 10 \text{ Mpc}$  this condition is probably not satisfied. Assuming virial equilibrium, the typical cluster mass is

$$M \simeq \frac{R_V \sigma_v^2}{G} \simeq \left( \frac{R_V}{1 h^{-1} \text{ Mpc}} \right) \left( \frac{\sigma_v}{10^3 \text{ km s}^{-1}} \right)^2 10^{15} h^{-1} M_{\odot}, \quad (2.2)$$

being  $R_V$  the virialization radius, which depends on the positions of the galaxies with

measured redshifts and recognized as true cluster members:

$$R_V = N^2 \left( \sum_{i>j} r_{ij}^{-1} \right)^{-1}, \quad (2.3)$$

where  $N$  is the total number of galaxies, and  $r_{ij}$  the projected separation between the  $i$ -th and  $j$ -th galaxies. Besides the assumption of virial equilibrium, which may be fulfilled to different degrees by different populations of galaxies (e.g., late vs. early type), a crucial aspect in the application of the dynamical mass estimator concerns the rejection of the back/foreground galaxies which lie along the line-of-sight of the cluster without belonging to it. A spurious inclusion of non-member galaxies in the analysis leads in general to an overestimate of the velocity dispersion and, therefore, of the resulting mass.

Through Eq. (2.2) Zwicky (1937) noticed in his study of the Virgo cluster that the mass retrieved by galaxy motions was greater than that associated with the optical light, and this was the first evidence of the presence of dark matter.

### 2.3 X-ray properties of clusters

Observations of galaxy clusters in the X-ray band have revealed that a substantial fraction ( $\sim 15$  per cent) of the cluster mass is in the form of hot diffuse gas, permeating its potential well. Clusters of galaxies are luminous X-ray sources, with typical luminosities in the range  $\sim 10^{43} - 10^{46}$  erg s $^{-1}$ . The X-ray emission is essentially due to thermal bremsstrahlung from the diffuse ICM, at a temperature of  $T \sim 10^7 - 10^8$  K and an atomic density of  $n \sim 10^{-1} - 10^{-4}$  cm $^{-3}$ , that fills the deep gravitational potentials. Among several emission mechanisms that were proposed, that of thermal emission from hot ICM revealed the most consistent with the X-ray spectra: in fact the detection of strong X-ray line emission from clusters, especially the 7 keV Fe line, cannot be explained with any other non-thermal model for the origin of the X-ray emission.

If this gas is subject to the same dynamics of galaxies, then we can expect it has a typical temperature of

$$k_B T \simeq \mu m_p \sigma_r^2 \simeq 6 \left( \frac{\sigma_r}{10^3 \text{ km s}^{-1}} \right)^2 \text{ keV}, \quad (2.4)$$

where  $m_p$  is the proton mass and  $\mu$  is the mean molecular weight ( $\mu \simeq 0.6$  for a primordial composition with a 76% fraction contributed by hydrogen). Observational data for nearby clusters (e.g. Wu et al., 1999) and for distant clusters (see Figure 2.1) actually follow this relation, although with some scatter and with a few outliers which reveal the presence of a more complex dynamics. The fact that temperature and galaxy dispersion were similar and proportional to one other suggests that both gas and galaxies were bound by the same gravitational potential, sharing the same dynamics.

We will discuss the basic properties of a hot diffuse plasma (Sect. 2.3.1), the physical processes responsible for the X-ray emission from the ICM (Sect. 2.3.2) and summarize the hydrostatic models for ICM distribution (Sect. 2.3.3).

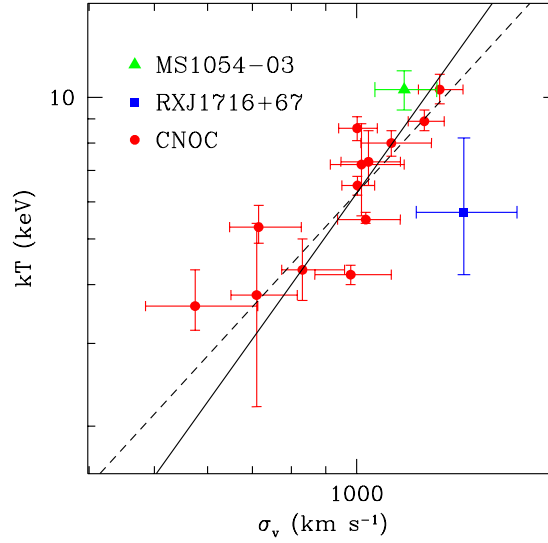


**Figure 2.1.** The relation between galaxy velocity dispersion,  $\sigma_v$ , and ICM temperature,  $T$ , for distant ( $z > 0.15$ ) galaxy clusters. The solid line shows the relation  $k_B T = \mu m_p \sigma_v^2$ , and the dashed line is the best-fit to the low- $z$   $T$ - $\sigma_v$  relation from Wu et al. (1999). (Figure from Rosati et al., 2002)

### 2.3.1 Physical Properties of Hot Diffuse Plasma

At its high energies ( $\sim 10^7 - 10^8$  K), the ICM behaves as a fully ionized plasma, whose emissivity is dominated by thermal bremsstrahlung. We are dealing with several simple assumptions (e.g. Sarazin, 1988) in studying the ionization state, line and continuum emission from a low density, optically thin hot plasma. These assumptions together constitute the 'coronal model'.

1. The ICM can be treated as a collisional fluid. In fact the mean free path of the electrons and ions

$$\lambda \approx 23 \text{ kpc} \left( \frac{T_e}{10^8 \text{ K}} \right)^2 \left( \frac{n_e}{10^{-3} \text{ cm}^{-3}} \right)^{-1} \quad (2.5)$$

is much shorter than the typical length scale in clusters ( $\sim 1$  Mpc), and therefore in the ICM the collisions are the dominant process.

2. The time scale for elastic Coulomb collisions between particles in the plasma is much shorter than the age or cooling time of the plasma, therefore the free particles obey the Maxwell-Boltzmann distribution at a given temperature  $T$ . In fact, it is possible to show (Spitzer, 1956; Spitzer, 1978) that homogeneous plasma with an initial non-Maxwellian particle distribution relaxes to a Maxwellian one through

Coulomb collisions on a time scale that is given by

$$t_{\text{eq}} \approx 3.3 \times 10^5 \text{ yr} \left( \frac{T_e}{10^8 \text{ K}} \right)^{3/2} \left( \frac{n_e}{10^{-3} \text{ cm}^{-3}} \right)^{-1} \quad (2.6)$$

for the electrons. The above time scale for the protons is about  $(m_p/m_e)^{1/2} \sim 40$  times longer than that for electrons. After this time, both the electrons and ions have a Maxwellian distribution, but generally at different temperatures, respectively  $T_e$  and  $T_i$ . The time scale for the electrons and ions to reach equipartition is  $\sim (m_p/m_e)t_{\text{eq}} \lesssim 6 \times 10^8$  years for typical values of the ICM temperature and density. So the above time scale is shorter than the age of the clusters: we can characterize the ICM by a single kinetic temperature.

3. The gas is optically thin and therefore stimulated radiative transitions can be neglected and the effect of the radiation field on the gas is insignificant.
4. The gas is at low density and therefore the transport of the radiation field can be ignored.
5. At these low densities, collisional excitation and de-excitation processes are much slower than radiative decays, and thus any ionization or excitation process is assumed to be initiated from the ground state of an ion. Three (or more) body collisional processes are ignored because of the low density.

Under these conditions, ionization and emission result primarily from collisions of ions with electrons, and collisions with other ions can be ignored. Moreover, the time scales for ionization and recombination are generally considerably shorter than the age of the cluster or any relevant hydrodynamic time scale, therefore the plasma is assumed to be in ionization equilibrium. The equilibrium ionization state of a diffuse plasma depends only on the electron temperature: since in nearly all astrophysical plasmas most of the electrons originate in hydrogen and helium atoms, and these are fully ionized under the conditions considered here, the ICM is generally treated as a fully ionized plasma.

### 2.3.2 Thermal emission in the ICM

The X-ray continuum emission from a hot diffuse plasma, such as the ICM, is due primarily to two processes: thermal bremsstrahlung (free-free emission) and recombination (free-bound) emission. Processes that contribute to X-ray line emission (bound-bound radiation) from a diffuse plasma include collisional excitation of valence or inner shell electrons, radiative and dielectric recombination, inner shell collisional ionization and radiative cascades following any of these processes.

At the high temperatures typical of clusters (in particular at  $T \gtrsim 2.5$  keV), thermal bremsstrahlung is the predominant X-ray emission process. The emissivity for this process at frequency  $\nu$  scales as

$$J_{\text{br}}(\nu, T) = 6.8 \times 10^{-38} Z^2 n_e n_i T^{-1/2} e^{-h\nu/kT} g(\nu, T) , \quad (2.7)$$

where  $n_e$  and  $n_i$  are the number density of electrons and ions, respectively, and  $g(\nu, T) \propto \ln(k_B T / h\nu)$  is the Gaunt factor, which accounts for quantum mechanical effects (Rybicki & Hummer, 1978).

If the ICM is mainly at a single temperature, then Eq. (2.7) indicates that the X-ray spectrum behaves as an exponential (as a function of the frequency), and this is generally observed.

By integrating the above equation over the energy range of the X-ray emission and over the gas distribution, one obtains the total power per unit volume:

$$J_{br}(T) = 1.4 \times 10^{-27} n_e n_i T^{1/2} Z^2 g(T) , \quad (2.8)$$

where  $g(T)$  is a frequency average of  $g(\nu, T)$  and it is of the order of the unity.

Even if the pure bremsstrahlung emissivity is a good approximation for  $T \gtrsim 3$  keV clusters, a further contribution from the strong lines (high equivalent width) in the 7 keV iron line complex must be considered and, when considering cooler systems, from other metal emission lines at  $T \lesssim 1$  keV should be also taken into account. Compilations of the different emissivities for X-ray lines and continua can be found in the literature (e.g. Raymond & Smith, 1977). The emissivities at the frequency  $\nu$  increase in proportion to the ion and electron densities, and depend otherwise on the temperature only, so that:

$$J_X(\nu, T) = \sum_{K,i} \Lambda_\nu(K^i, T) n(K^i) n_e , \quad (2.9)$$

where  $\Lambda_\nu$  is the emission per ion at unit electron density at the frequency  $\nu$ .

Integrating Eq. (2.9) on all the frequencies, the bolometric emissivity at a temperature  $T$  can be written as:

$$J_X(T) = \Lambda(T) n_e n_p \text{ erg s}^{-1} \text{ cm}^{-3} \quad (2.10)$$

where  $\Lambda(T)$  is the cooling function, which depends on the mechanism of the emission. For thermal bremsstrahlung,  $\Lambda(T) \propto T^{1/2}$ .

The observed X-ray luminosity is related to the Eq. (2.10) through:

$$L_X = \int J_X(T) dV = \Lambda(T) \int n_e n_p dV , \quad (2.11)$$

where the quantity  $EI = \int n_e n_p dV$  is known as emission integral. Since the projection on the sky of the plasma emissivity gives the X-ray surface brightness or luminosity, the latter can be geometrically deprojected or fitted with a model of the assumed distribution of the gas density by applying Eq. (2.11), in order to constrain the physical parameters of the ICM, such as its density and temperature. The metal content of the ICM can be investigated through X-ray spectroscopy instead. Measurements of tens nearby clusters have yielded a mean metallicity  $Z \sim 1/3 Z_\odot$ , largely independently of the cluster temperature, while the spatial distribution of metals has been started to be studied in detail with the first spatially-resolved spectroscopic data obtained with *ASCA* and *Beppo-SAX* (e.g. White, 2000; De Grandi & Molendi, 2001).

### 2.3.3 Hydrostatic equilibrium in ICM

Given a plasma with sound speed  $c_s^2 = \gamma kT / \mu m_p$ , where  $\gamma = 5/3$  for a monoatomic gas, one finds that the time required for a sound wave in the ICM to cross the cluster is given by:

$$t_s \approx 6.6 \times 10^8 \left( \frac{T}{10^8 \text{ K}} \right)^{-1/2} \left( \frac{D}{1 \text{ Mpc}} \right) \text{ yr} , \quad (2.12)$$

where  $D$  is the cluster diameter. Since this time is considerably shorter than the age of the cluster, the plasma is assumed to be in hydrostatic equilibrium, unless the cluster gravitational potential varies on a shorter time scale or the gas is heated or cooled more rapidly than this. The cooling time due to thermal bremsstrahlung is much longer than the above time scale, so the gas distribution is generally assumed to be hydrostatic:

$$\nabla P = -\rho \nabla \phi \quad (2.13)$$

where  $P = \rho kT / \mu m_p$  is the gas pressure,  $\rho$  is the gas density and  $\phi$  is the gravitational potential of the cluster.

If the cluster is assumed to be spherically symmetric, Eq. (2.13) reads:

$$\frac{1}{\rho} \frac{dP}{dr} = -\frac{d\phi}{dr} = -\frac{GM(< r)}{r^2} , \quad (2.14)$$

where  $r$  is the radial coordinate (clustercentric distance) and  $M(< r)$  is the total mass contained within  $r$ .

### 2.3.4 The $\beta$ -Model for ICM Distribution

A common description of the gas density profile is the so called  $\beta$ -model,

$$\rho_g(r) = \rho_{g,0} \left[ 1 + \left( \frac{r}{r_c} \right)^2 \right]^{-3\beta/2} , \quad (2.15)$$

which was introduced by Cavaliere & Fusco-Femiano (1976) to describe an isothermal gas in hydrostatic equilibrium within the potential well associated with a King dark-matter density profile. In the above equation,  $r_c$  is the core radius, while the parameter  $\beta$  is the ratio between the kinetic energy of any tracer of the gravitational potential (e.g. galaxies) and the thermal energy of the gas:

$$\beta = \frac{\sigma_r^2}{kT / \mu m_p} . \quad (2.16)$$

In its original derivation, the  $\beta$ -model was aimed at representing the distribution of isothermal gas sitting in hydrostatic equilibrium within a King-like potential, which is a reasonable approximation of the isothermal sphere: in this case it is possible to show that there is a relationship between the mass density in galaxies  $\rho_{\text{gal}}$  and the gas density  $\rho$

$$\rho \propto \rho_{\text{gal}}^\beta \quad (2.17)$$

The surface brightness profile observed at a projected radius  $b$ ,  $I(b)$ , is obtained by integrating along the line-of-sight the plasma emissivity. The functional form of the surface brightness profile reads:

$$I(b) = I_0 \left[ 1 + \left( \frac{b}{r_{\text{core}}} \right)^2 \right]^{\frac{1}{2} - 3\beta} . \quad (2.18)$$

This parametrization is widely used in the X-ray astronomy to recover the gas density profile by fitting the surface brightness profile in galaxy clusters. Nevertheless, the improved angular resolution and large field of view of the Chandra and Newton-XMM satellites has shown that the  $\beta$ -model cannot always describe properly the surface brightness profile of clusters.

The  $\beta$ -model is an useful means for interpreting cluster emissivity, although over limited dynamical ranges. In fact, if the gravitational behaviours of the gas and galaxies were identical, we expect that  $\beta = 1$ . However, since the galaxies can be considered as a collisionless system while the gas is a collisional fluid, these two components will be partially separated during the cluster formation. For example, the infalling gas will typically be stopped by the passage of a shock while the galaxies continue to fall inwards: this causes the gas to be less tightly bound than the galaxies, indicating that gas and galaxies in clusters do not exactly share the same dynamics. Therefore, one could expect  $\beta \lesssim 1$ , as observed (e.g. Jones & Forman, 1984; Bahcall & Lubin, 1994). This indicates that the gas density should fall off less rapidly with radius than the galaxy density, as observed, and that the energy per unit mass is higher in the gas than in the galaxies.

Nevertheless, this does not agree with the determinations of the X-ray spectral temperatures and the galaxy velocity dispersion of clusters (Eq. 2.4): the observed correlation between  $\sigma_r^2$  and  $kT$  implies that the average value  $\beta$  determined by gas temperature and gas velocity dispersion (Eq. 2.16) is  $\beta_{\text{spec}} \approx 1 - 1.3$ , which is about a factor of two larger than the value  $\beta_{\text{fit}}$  determined by fits on the X-ray surface brightness ( $\beta_{\text{fit}} \approx 0.6 - 0.8$ ). The  $\beta$ -discrepancy shows how the assumptions of this model, such as isothermality of the gas, isotropic galaxy velocity distribution, King-like gravitational potential well, are too simplistic.

### 2.3.5 Cooling in the ICM

The X-rays emitted from clusters of galaxies represent a loss of energy of the ICM. Thermal emissivity due to bremsstrahlung and line emission depends on the square of the gas density (Eq. 2.7), which strongly rises towards the cluster center, i.e. the emissivity is much more pronounced in the internal regions over scales  $\lesssim 100$  kpc. In the core region the cooling rate of the ICM is sufficiently high that the particles loose a significant fraction of their thermal energy via radiation. In order to understand the role of cooling in the ICM one defines the cooling time-scale, which is given by

$$t_{\text{cool}} = \frac{k_B T}{n_e \Lambda(T)} \approx 2.7 \times 10^8 (n_e / 10^{-1} \text{cm}^{-3})^{-1} (T / 10^7 \text{K})^{1/2} \text{yr} , \quad (2.19)$$

$n_e(r)$  being the number density of electrons and where in the second equality we have considered a pure bremsstrahlung emission (e.g. Sarazin, 1988). Therefore, the cooling time in central cluster regions can be shorter than the Hubble time. A substantial fraction of gas undergoes cooling in these regions, and consequently drops out of the hot diffuse, X-ray emitting phase. The density of the gas in the core regions then increases to maintain the pressure required to support the weight of the overlying gas in the rest of the cluster, leading to a slow subsonic inflow of material towards the cluster center. This simple picture describes the physics of the process known as a cooling flow (Fabian, 1994).

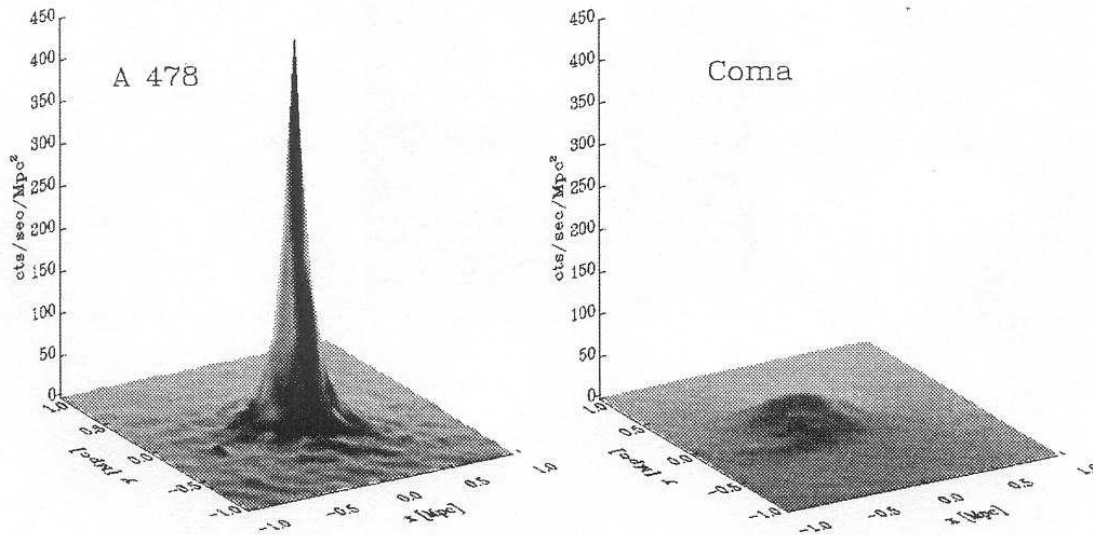


**Figure 2.2.** A comparison of the X-ray surface brightness profile of A478 (a cool core cluster) and Coma (a non-cool core cluster). The figures have been scaled to simulate the appearance of the systems when viewed at the same redshift, being the two objects with similar overall X-ray luminosities. From Allen & Fabian (1997).

The canonical picture of cooling flows predicted that the lack of pressure support due to gas cooling in the core region causes overlying external gas to flow towards the center, creating a superpositions of many gas phases at different temperature. The improved spectral resolution and sensitivity of the XMM satellite has shown that the soft X-ray spectra of several cooling flow clusters of galaxies are inconsistent with standard cooling flow models as the gas cools down to about 2 – 3 keV (e.g. Peterson et al., 2002), but not to lower temperatures as expected in the canonical picture (e.g. Böhringer et al., 2002; Fabian et al., 1991).

The solution to this problem is quite ticklish. Numerical simulations (Muanwong et al., 2002) have shown that cooling in itself is a runaway process, leading to a large fraction of gas that cools down ( $\sim 50\%$ ), whereas observational data indicate that only  $\lesssim 10\%$  of the cluster baryons are locked into stars (e.g. Balogh et al., 2001; Bower et al., 2001). This calls for the presence of further sources of non-gravitational energy, such as local heating by, e.g., AGN activity (e.g. Valageas & Silk, 1999; Wu et al., 2000; Yamada &

Fujita, 2001; Brighenti & Mathews, 2006), star formation or supernovae (Bialek et al., 2001; Brighenti & Mathews, 2006; Babul et al., 2002; Borgani et al., 2002), which might be able to provide sufficient amount of extra energy to balance overcooling.

The effects of gas cooling are well known to influence the X-ray emission from clusters of galaxies (Fabian, 1994), as inferred from X-ray images of the cores of many clusters which show strongly peaked surface brightness distributions (Fig. 2.2). Cooling flows may be present in as many as 70 per cent of clusters (Peres et al., 1998), particularly amongst older, relaxed systems, where merger-induced mixing of gas is not a significant effect.

## 2.4 The Sunyaev-Zel’dovich effect

The thermal Sunyaev-Zel’dovich effect is a very small distortion of the spectra of the cosmic microwave background, due to the Inverse Compton between the photons of the CMB and the hot ( $\sim 10^7 - 10^8$  K) electrons of the ICM trapped into the gravitational potential well of the dark matter halo (Sunyaev & Zeldovich, 1970; Birkinshaw, 1999). The CMB photons have a very low probability  $\tau$  ( $\tau \sim 0.01$ ) of interaction with the hot electrons of the ICM, which increases statistically their energy by a factor  $\approx k_B T_e / m_e c^2$ , producing the distortion of the black-body spectrum of the CMB: this appears as a decrease of the monochromatic flux of the CMB at frequencies smaller than 218 GHz and as an increase at frequencies larger than 218 GHz. We can parameterize the amplitude of this effect by considering the Compton parameter  $y(\theta)$ , which is expressed by the following relation:

$$y(\theta) \equiv \frac{\sigma_T}{m_e c^2} \int P_e(\vec{r}) dl , \quad (2.20)$$

where  $\theta$  is the angular distance from the cluster centre,  $\sigma_T$  is the Thomson cross-section, and  $P_e(\mathbf{r}) \equiv n_e(\mathbf{r}) k_B T_e(\mathbf{r})$  is the pressure of the electrons of the ICM at the volume element of coordinate  $\mathbf{r}$ ,  $k_B$  is the Boltzmann constant;  $l$  is the line of the sight.

In an equivalent way we can think the SZ effect as a small variation in the brightness temperature ( $\Delta T_{sz}$ ) or in the brightness ( $\Delta I_{sz}$ ) of the CMB:

$$\Delta T_{sz} = f_{(x, T_e)} T_{\text{cmb}} y , \quad (2.21)$$

$$\Delta I_{sz} = g_{(x, T_e)} I_0 y , \quad (2.22)$$

where  $I_0 = 2(kT_{\text{cmb}})^3 / (hc)^2$ ,  $x = h\nu / kT_{\text{cmb}}$ ;  $f_{(x, T_e)}$  e  $g_{(x, T_e)}$  are given by:

$$f_{(x, T_e)} = \left( x \frac{e^x + 1}{e^x - 1} - 4 \right) (1 + o(x, T_e)), \quad (2.23)$$

$$g_{(x, T_e)} = \frac{x^4 e^x}{(e^x - 1)^2} \left( x \frac{e^x + 1}{e^x - 1} - 4 \right) (1 + o(x, T_e)). \quad (2.24)$$

and account for the frequency dependence of the SZ effect, and for the relativistic corrections related to the term  $o(x, T_e)$  (Itoh et al. (1998)), which we consider in our

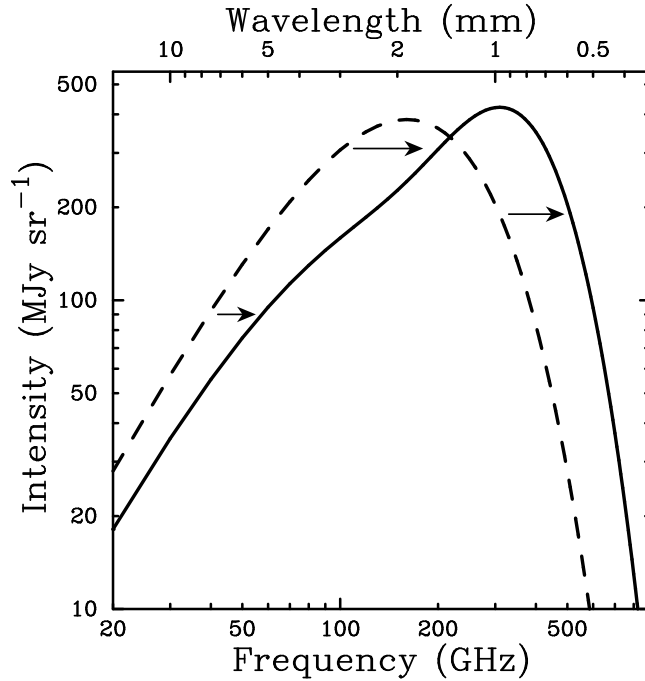


**Figure 2.3.** The Cosmic Microwave Background (CMB) spectrum, undistorted (dashed line) and distorted by the thermal Sunyaev-Zel'dovich effect (solid line). The SZ distortion shown is for a fictional cluster 1000 times more massive than a typical massive galaxy cluster. The SZ effect causes a decrease in the CMB intensity at frequencies smaller than 218 GHz and an increase at higher frequencies (from Carlstrom et al., 2002).

treatment up to the 5-th order, even though they are  $\ll 1$  for all clusters with temperature  $\lesssim 10$  keV. Figure 2.3 shows the spectral distortion of the CMB due to the thermal SZ effect for a fictional cluster that is over 1000 times more massive than a typical cluster to illustrate the small effect. The SZ effect causes a decrease in the CMB intensity at frequencies  $\lesssim 218$  GHz and an increase at higher frequencies.

Because the instruments suitable for the observations are usually interferometers, the best fit models are computed using visibilities (i.e. data in the Fourier domain) instead of intensity (i.e. data in the image domain). In fact, we know that the visibility  $V(\vec{u}) = V(u, v)$  in the  $uv$ -plane is the Fourier transform ( $\mathcal{FT}$ ) of the brightness  $I(\vec{\phi})$ ,  $\vec{\phi} = (\phi, \theta)$ ,  $\phi = R/D_a$ , with  $D_a$  diameter distance and  $R^2 = r^2 + l^2$ :

$$\begin{aligned}
 V(\vec{u}) &= \int_{-\infty}^{\infty} d\vec{\phi} B(\vec{\phi}) I(\vec{\phi}) e^{i2\pi\vec{\phi}\cdot\vec{u}} = \\
 &2\pi \int_0^{\infty} B(\phi) I(\phi) J_0^k(2\pi\phi u) \phi d\phi ,
 \end{aligned} \tag{2.25}$$

where the last equality is true in the case of radial symmetry, where the  $\mathcal{FT}$  transform became the Hankel transform ( $\mathcal{HT}$ ); here  $J_0^k$  indicates the  $K$  Bessel function of the zero order,  $B(\phi)$  is a specific numerical function, normalized to one, that describes the primary beam of the telescope (Pearson et al., 2003).

Due to the poor coverage of the  $uv$ -plane of the SZ data, which actually inhibits the

above Fourier inversion, the best way to constrain the physical parameter is to work in the Fourier domain, by performing a  $\mathcal{HT}$  of the X-ray model and comparing it with the observed visibilities.

## 2.5 Methods to estimate galaxy cluster mass

### 2.5.1 The hydrostatic equilibrium equation

In addition to providing an efficient method to detect clusters, X-ray studies of the ICM allow one to measure the total gravitating cluster mass, which is the quantity predicted by theoretical models for cosmic structure formation. The condition of hydrostatic equilibrium (Eq. 2.13) determines the balance between the pressure force and the gravitational force. By inserting the equation of state for a perfect gas,  $P = \rho_{\text{gas}} k_B T / \mu m_p$  into Eq. (2.13), one can express  $M(< R)$ , the total gravitating mass within  $R$  under the assumption of a spherically symmetric gas distribution as

$$M(< r) = -\frac{r k_B T}{G \mu m_p} \left( \frac{d \ln \rho_{\text{gas}}}{d \ln r} + \frac{d \ln T}{d \ln r} \right), \quad (2.26)$$

where  $\mu$  is the mean molecular weight of the gas ( $\mu \simeq 0.6$  for primordial composition) and  $m_p$  is the proton mass. An often used mass estimator is based on assuming the  $\beta$ -model for the gas density profile (Eq. 2.15). By further assuming a polytropic equation of state  $\rho_{\text{gas}} \propto P^\gamma$ , being  $\gamma$  the polytropic index, Eq. (2.26) becomes

$$M(< r) \simeq 1.11 \times 10^{14} \beta \gamma \frac{T(r)}{\text{keV}} \frac{r}{h^{-1} \text{Mpc}} \frac{(r/r_c)^2}{1 + (r/r_c)^2} h^{-1} M_\odot, \quad (2.27)$$

where  $T(r)$  is the temperature at the radius  $r$ . The mass corresponding to a  $\beta$ -model parametrization under the isothermal assumption is recovered from Eq. (2.27) by setting  $\gamma = 1$  and replacing  $T(r)$  with the overall ICM temperature. In the absence of accurately resolved temperature profiles from X-ray observations, Eq. (2.27) has been used to estimate cluster masses both in its isothermal and in its polytropic form. In Figure 2.4 we present the relation between dynamical optical masses (Eq. 2.2) and masses derived from the X-ray temperature by assuming hydrostatic equilibrium (Eq. 2.27).

The improved angular resolution and sensitivity of the Chandra and Newton-XMM satellites has allowed to recover temperature profiles with high accuracy through the application of more general methods of mass estimation, not necessarily based on the assumptions of  $\beta$ -model and of a polytropic form for the equation of state (Allen et al., 2001; Ettori et al., 2002).

The crucial a-priori assumptions underlying any mass measurements concern the hydrostatic equilibrium, spherical geometry and the absence of substructures. Some of these assumptions have been tested through hydrodynamical numerical simulations (see Rasia et al., 2006, for a study of the systematics on the recovered mass profiles) or through a parametric combination of X-ray and Sunyaev-Zel'dovich effect measurements (see De Filippis et al., 2005, for a study of the systematics related to spherical assumption).

Local deviations from isothermality due to the presence of cold substructures can bias the spectroscopic temperature (and therefore the mass estimates) with respect to the actual electron temperature (Mazzotta et al., 2004; Rasia et al., 2006).

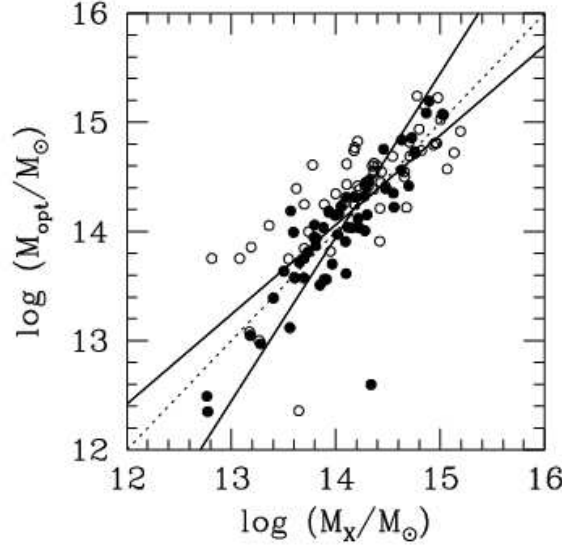


**Figure 2.4.** The relation between dynamical optical masses and masses derived from the X-ray temperature by assuming hydrostatic equilibrium (from Girardi et al., 1998).

### 2.5.2 The self-similar scaling

The self-similar model (see, e.g., Kaiser, 1986) gives a simple picture of the process of cluster formation in which the ICM physics is driven by the infall of cosmic baryons into the gravitational potential of the cluster DM halo. The collapse and subsequent shocks heat the ICM up to the virial temperature. Since gravity has not a preferred scale, we expect clusters of different sizes to be the scaled version of each other as long as gravity only determines the ICM evolution. This is the reason why the ICM model based on the effect of gravity only is said to be self-similar. Thanks to this model, which assumes that gravity is the only responsible for the observed values of the different physical properties of galaxy clusters, we have a simple way to establish theoretical analytic relations between them.

Assuming the spherical collapse model (Sect. 1.2.3) for the DM halo and the equation of hydrostatic equilibrium to describe the distribution of baryons into the DM potential well, in the self-similar model the cluster mass and temperature are related by:

$$E_z \Delta_v^{1/2} M_{\text{tot}} \propto T^{3/2}; \quad (2.28)$$

where  $E_z = (H(z)/H_0)^2$ ,  $H(z)$  and  $\Delta_v$  are given by Eq. (1.8) and (1.27), respectively. So we have  $R_{\Delta_v} \propto (M/(\rho_{c,z} \Delta_v))^{1/3} \propto T^{1/2} E_z^{-1} \Delta_v^{-1/2}$ . From the previous equations we can

easily obtain further relations (see, e.g., Markevitch, 1998; Allen & Fabian, 1998; Ettori et al., 2004; Arnaud et al., 2005; Vikhlinin et al., 2005; Pratt & Arnaud, 2005), such as:

$$E_z^{-1}(\Delta_v/\Delta)^{-1/2}L \propto T_{\text{gas}}^2, \quad (2.29)$$

$$E_z^{-1}(\Delta_v/\Delta)^{-1/2}L \propto (E_z(\Delta_v/\Delta)^{1/2}M_{\text{tot}})^{4/3} \quad (2.30)$$

Eq. (2.28) and (2.30) are unique predictions for the scaling relations among ICM physical quantities and, in principle, they provide a way to relate the cluster masses to observables at different redshifts. Nevertheless, it was soon recognized that X-ray clusters do not completely obey these scaling relations. The observed luminosity–temperature relation for clusters is  $L_X \propto T^3$  for  $T \gtrsim 2$  keV, and possibly even steeper for  $T \lesssim 1$  keV groups. Deviations with respect to these relations witness the presence of more complex physical processes, beyond gravitational dynamics only, which affect the thermodynamical properties of the diffuse baryons and, therefore, the relation between observables and cluster masses. We will discuss in detail the scaling relations among cluster observables in Chapter 3.

## 2.6 An overview of Chandra and CBI

Nowadays the improved angular resolution and sensitivity of the new generation of the X-ray satellites like Chandra and XMM-Newton has allowed us to unveil the complex interplay of the physical processes which happen in the internal regions of galaxy clusters. On the other hand, thanks to the development of incoming microwave instruments (ALMA, APEX, the Cosmic Background Imager 2, the South Pole Telescope), we are now in the position to obtain large untargeted SZ surveys, which will provide a direct view of the high redshift universe.

As outlined in the Introduction, in the work of this Thesis we have considered a sample of galaxy clusters to characterize the properties of the X-ray and SZ signals, focusing on the determination of the physical properties of intracluster gas and DM. In particular, we have constructed a sample of 24 X-ray galaxy clusters observed with Chandra, having a central Compton parameter  $y_0$  (Eq. 2.20) taken from the literature or interferometric SZ data obtained with the Cosmic Background Imager (CBI).

Here we briefly describe the main characteristics of Chandra and CBI instruments.

### 2.6.1 The Chandra X-ray Observatory

The Chandra X-ray Observatory is the U.S. follow-on to the Einstein Observatory. Chandra was formerly known as AXAF, the Advanced X-ray Astrophysics Facility, but renamed by NASA in December, 1998. The Chandra spacecraft carries a high resolution mirror, two imaging detectors, and two sets of transmission gratings. The main characteristics of this satellite are: very high spatial resolution ( $\simeq 0.5$  arcseconds), good sensitivity from 0.1 to 10 keV, and high spectral resolution over most of this range. Chandra was designed to have considerable collecting area between 0.5 and 7 keV,

allowing the detection of iron lines emitted by many astrophysical sources. Therefore, a wide variety of high-energy phenomena in an all-encompassing range of astronomical objects are being observed.

Chandra is in an elliptical high-earth orbit allowing uninterrupted observing intervals of more than 48 hours in length. This satellite consists of 4 pairs of concentric thin-walled, grazing-incidence Wolter Type-I mirrors called the High Resolution Mirror Assembly (HRMA, see Figure 2.5). The front mirror of each pair is a paraboloid and the back a hyperboloid. The eight mirrors were fabricated from Zerodur glass, polished, and coated with iridium on a binding layer of chromium. The high energy response is achieved by using relatively small reflection angles and by coating the mirrors with iridium. The combination of high resolution, large collecting area, and sensitivity to higher energy X-rays makes it possible for Chandra to study extremely faint sources, sometimes strongly absorbed, in crowded fields.

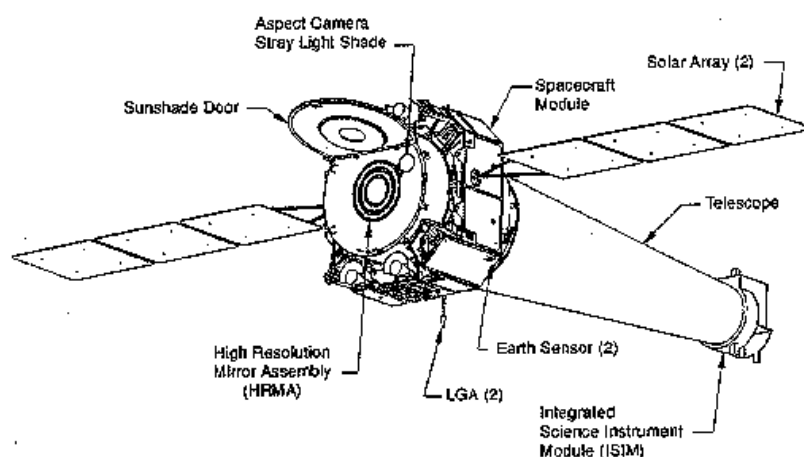


**Figure 2.5.** An image of the Chandra X-ray Observatory.

There are two transmission grating spectrometers, formed by sets of gold gratings placed just behind the mirrors. One set is optimized for low energies (LETG) and the other for high energies (HETG). Spectral resolving powers ( $E/\Delta E$ ) in the range 100 to over 1000 can be achieved with good efficiency. These produce spectra dispersed in space at the focal plane.

Chandra has two focal plane instruments: the High Resolution Camera (HRC), and the Advanced CCD Imaging Spectrometer (ACIS). The HRC has small pore size, large microchannel plate (MCP), low background, charged particle anticoincidence, and high energy resolution, which make this instrument useful for high resolution imaging, fast timing measurements, and for observations requiring a combination of both.

The ACIS instrument is an array of charged coupled devices. A two-dimensional array of these small detectors does simultaneous imaging and spectroscopy. Pictures of extended objects can be obtained with both high spatial resolution along and spectral information from each element of the picture. ACIS is comprised of two CCD arrays, a 4-chip array, ACIS-I; and a 6-chip array, ACIS-S. The CCDs are flat, but the chips in each array are

positioned (tilted) to approximate the relevant focal surface: that of the HRMA for ACIS-I and that of the HETG Rowland circle for ACIS-S. ACIS-I was designed for CCD imaging and spectrometry; ACIS-S can be used both for CCD imaging spectrometry and also for high-resolution spectroscopy in conjunction with the HETG grating. There are two types of CCD chips. ACIS-I is comprised of front-illuminated (FI) CCDs. ACIS-S is comprised of 4 FI and 2 back-illuminated (BI) CCDs, one of which is at the best focus position. The efficiency of the ACIS instrument has been discovered to be slowly changing with time, most likely as a result of molecular contamination build-up on the optical blocking filter. The BI CCDs response extends to lower energies than the FI CCDs and the energy resolution is mostly independent of position. The low-energy response of the BI CCDs is partially compromised by the contaminant build-up. The FI CCD response is more efficient at higher energies but the energy resolution varies with position due to radiation damage caused by protons reflecting through the telescope during radiation-zone passages in the early part of the mission.

Chandra’s capabilities provide unprecedented science and Chandra users are making important contributions to all areas of astronomy, including the solar system, stars, interacting binaries, compact objects, supernovae, galaxies, AGN and galaxy clusters.

### 2.6.2 The Cosmic Background Imager

The Cosmic Background Imager (CBI) is a radio telescope designed to study the cosmic microwave background radiation. The CBI is located at an altitude of 5080 meters near San Pedro de Atacama, in the Andes in northern Chile: this high and dry site minimizes the effects of Earth’s atmosphere and guarantees good sensitivity levels in a reasonable observing time.

It is an instrument primarily designed to measure both the temperature and polarization properties of the CMB, including the SZ effect in clusters of galaxies, in the frequency range 26-36 GHz and on angular scales from 5 arcminutes to one degree (spherical harmonic scales from  $l = 3000$  down to  $l = 300$ ). This instrument is a 13-element interferometer mounted on a 6 meter platform operating in ten 1-GHz frequency bands from 26 GHz to 36 GHz. The instantaneous field of view of the instrument is 44 arcmin and its resolution ranges from 4.5 to 10 arcmin.

The CBI consists of 13 separate radio antennas, each 90 cm in diameter, mounted on a single altazimuth platform (see Figure 2.6), giving interferometer baselines  $d$ , i.e. the distance between a pair of antenna in  $\lambda$  unit (where  $\lambda$  is the wavelength,  $\lambda \sim 1$  cm), that can be adjusted in length from  $1/\lambda$  to  $5.5/\lambda$ . An interferometer of baseline  $d$  is sensitive to cosmic microwave background radiation structure with multipole  $l = 2\pi d/\lambda$ . The orientation of the baselines can be changed by rotating the platform. The CBI measures 10 channels for each of 78 baselines simultaneously, while the field of view is basically given by the primary beam, i.e. the diffraction figure of the antennas. Larger fields can be imaged by assembling data from multiple pointings (called “mosaicing”).

Each antenna is a 90-cm parabolic reflector enclosed in a shield can and protected by a teflon cover that is transparent to radio radiation. The signals from each pair of antennas are combined in a correlator: the function of this computer machine is that to remove the



**Figure 2.6.** An image of the Cosmic Background Imager.

so-called spillover, i.e. the constant part of the microwave background and radiation from the ground and the atmosphere, and to compute the real and imaginary parts of the cross-correlation between the signal detected by the  $i$ -th and  $j$ -th antenna. Once these data are further analyzed by convenient software, the resulting output are processed to extract the physical information: this output basically represents a sample of Fourier transform (the visibilities) of the temperature properties of the CMB (Eq. 2.25)

In 2006, the CBI was upgraded to CBI2. The original 0.9m dishes were upgraded to 1.4m dishes each with a new foam cone supporting the new secondaries. The array was re-configured to maximize the number of long baselines. As well as increasing the sensitivity to CMB fluctuations on small angular scales ( $l > 900$ ), this upgrade makes the CBI much more suited to SZ observations, by both increasing the flux sensitivity and reducing the relative contamination from primordial CMB anisotropies.

## Chapter 3

# X-ray and Sunyaev-Zel'dovich scaling relations in galaxy clusters

This Chapter aims at presenting an analysis of the scaling relations between X-ray properties and Sunyaev-Zel'dovich parameters for a sample of 24 X-ray luminous galaxy clusters observed with Chandra and with measured SZ effect. The combined analysis of the SZ and X-ray scaling relations is a powerful tool to investigate the physical properties of the clusters and their evolution in redshift, by tracing out their thermodynamical history. We observe that the correlations among X-ray quantities only are in agreement with previous results obtained for samples of high- $z$  X-ray luminous galaxy clusters. On the relations involving SZ quantities, we obtain that they correlate with the gas temperature with a logarithmic slope significantly larger than the predicted value from the self-similar model. Our results on the X-ray and SZ scaling relations show a tension between the quantities more related to the global energy of the system (e.g. gas temperature, gravitating mass) and the indicators of the structure of the ICM (e.g. gas density profile, central Compton parameter  $y_0$ ). These relations consistently show a negative evolution suggesting a scenario in which the ICM at higher redshift has lower both X-ray luminosity and pressure in the central regions than the expectations from self-similar model. This Chapter is mainly based on the refereed paper "X-ray and Sunyaev-Zel'dovich scaling relations in galaxy clusters", Morandi A., Ettori S., Moscardini L. 2007, MNRAS, 379, 518-534.

### 3.1 Introduction

In Chapter 2 we have seen that the so-called self-similar scenario is the simplest model to explain the physics of the ICM, assuming that gravity only determines the thermodynamical properties of the hot diffuse gas (see, e.g., Kaiser , 1986). Since gravity has not a preferred scale, we expect clusters of different sizes to be the scaled version of each other as long as gravity only determines the ICM evolution and there are no preferred scales in the underlying cosmological model. This allows to build a very simple model to relate the physical parameters of clusters: the so-called self-similar model (Kaiser , 1986; Evrard & Henry, 1991). Based on that, we can derive scaling relations (see Sect. 3.3) between X-ray quantities (like temperature  $T$ , mass  $M$ , entropy  $S$  and luminosity  $L$ ), and between X-ray and Sunyaev-Zel'dovich measurements

(like the Compton- $y$  parameter), thanks to the assumption of spherical collapse for the DM halo and hydrostatic equilibrium of the gas within the DM gravitational potential. These relations provide a powerful test for the adiabatic scenario. In particular, in the recent years the studies about the X-ray scaling laws (see, e.g., Allen & Fabian, 1998; Markevitch, 1998; Ettori et al., 2004; Arnaud et al., 2005; Vikhlinin et al., 2005; Voit & Donahue, 2005), together with observations of the entropy distribution in galaxy clusters (see, e.g., Ponman et al., 1999, 2003) and the analysis of simulated systems including cooling and extra non-gravitational energy injection (see, e.g., Borgani et al., 2004) have suggested that the simple adiabatic scenario is not giving an appropriate description of galaxy clusters. In particular the most significant deviations with respect to the self-similar predictions are: (i) a lower (by  $\sim 30 - 40$  per cent) normalization of the  $M - T$  relation in real clusters with respect to adiabatic simulations (Evrard et al., 1996); (ii) steeper slopes for the  $M - T$  and  $L - T$  relations; (iii) an entropy ramp in the central regions of clusters (see, e.g., Ponman et al., 1999, 2003). These deviations are likely the evidence of non-radiative processes, like non-gravitational heating due to energy injection from supernovae, AGN, star formation or galactic winds (see, e.g., Pearce et al., 2001; Tozzi & Norman, 2001; Bialek et al., 2001; Babul et al., 2002; Borgani et al., 2002; Brighenti & Mathews, 2006) or cooling (see, e.g., Bryan, 2000). More recently some authors pointed out that there is a mild dependence of the X-ray scaling relations on the redshift, suggesting that there should be an evolution of these non-gravitational processes with  $z$  (Ettori et al., 2004).

An additional and independent method to evaluate the role of radiative processes is the study of the scaling relations based on the thermal SZ effect (Sunyaev & Zeldovich, 1970), which offers a powerful tool for investigating the same physical properties of the ICM, being the electron component of cosmic baryons responsible of both the X-ray emission and the SZ effect. The advantage of the latter on the former is the possibility of exploring clusters at higher redshift, because of the absence of the cosmological dimming. Moreover, since the SZ intensity depends linearly on the density, unlike the X-ray flux, which depends on the squared density, with the SZ effect it is possible to obtain estimates of the physical quantities of the sources reducing the systematic errors originated by the presence of sub-clumps and gas in multi-phase state and to study in a complementary way to the X-ray analysis the effects of extra-physics on the collapse of baryons in cluster dark matter halos, both via numerical simulations (White et al., 2002; da Silva et al., 2004; Diaferio et al., 2005; Nagai, 2006) and observationally (Cooray 1999; McCarthy et al. (2003a,b); Benson et al. (2004); LaRoque et al. (2006); Bonamente et al. (2006)).

The main purpose of this Chapter is to understand how these SZ and X-ray scaling relations evolve with redshift. In particular we want to quantify how much they differ from the self-similar expectations in order to evaluate the amplitude of the effects of the non-gravitational processes on the physical properties of ICM. Another issue we want to debate is which relations can be considered a robust tool to link different cluster physical quantities: this has important consequences on the possibility of using clusters as probes for precision cosmology. To do that, we have assembled a sample of 24 galaxies clusters, for which measurements of the Compton- $y$  parameter are present in the literature. Respect

the previous works we have done our own spatially resolved X-ray analysis recovering X-ray and SZ quantities necessary to investigate scaling relations. We have performed a combined spatial and spectral analysis of the X-ray data, which allows us to derive the radial profile for temperature, pressure, and density in a robust way. These results, which have high spatial resolution, rely only on the hydrostatic equilibrium hypothesis and spherical geometry of the sources. Moreover we can compare the observed physical quantities with the results of hydrodynamical numerical simulations in a consistent way.

This Chapter is organized as follows. In Sect. 3.2 we introduce our cluster sample and we describe the method applied to determine the X-ray properties (including the data reduction procedure) and the corresponding SZ quantities. In Sect. 3.3 we report our results about the scaling relations here considered, including the presentation of the adopted fitting procedure. Sect. 3.4 is devoted to a general discussion of our results, while in Sect. 3.5 we summarize our main conclusions. We leave to the appendices the discussion of some technical details of our data reduction procedure.

## 3.2 The dataset

### 3.2.1 Data reduction

We have considered a sample of galaxy clusters for which we have SZ data from the literature and X-ray data from archives (see Tables 3.1 and 3.2, respectively). In particular, we have considered the original sample of McCarthy et al. (2003b), to which we added two more objects from the sample discussed by Benson et al. (2004). For all these clusters we have analyzed the X-ray data extracted from the *Chandra* archive. In total we have 24 galaxy clusters with redshift ranging between 0.14 and 0.82, emission-weighted temperature in the range 6–12 keV and X-ray luminosity between  $10^{45}$  and  $10^{46}$  erg s<sup>-1</sup>. In the whole sample we have 11 cooling core clusters and 13 no-cooling core ones (hereafter CC and NCC clusters, respectively) defined according to the criterion that their cooling time in the inner regions is lower than the Hubble time at the cluster redshift.

We summarize here the most relevant aspects of the X-ray data reduction procedure. Most of the observations have been carried out using ACIS–I, while for 4 clusters (A1835, A370, MS0451.6-0305, MS1137.5+6625) we have data from the Back Illuminated S3 chip of ACIS–S. We have reprocessed the event 1 file retrieved from the *Chandra* archive with the CIAO software (version 3.2.2) distributed by the *Chandra* X-ray Observatory Centre. We have run the tool `aciss_proc_events` to apply corrections for charge transfer inefficiency (for the data at 153 K), re-computation of the events grade and flag background events associated with collisions on the detector of cosmic rays. We have considered the gain file provided within CALDB (version 3.0) in this tool for the data in FAINT and VFAINT modes. Then we have filtered the data to include the standard events grades 0, 2, 3, 4 and 6 only, and therefore we have filtered for the Good Time Intervals (GTIs) supplied, which are contained in the `flt1.fits` file. We checked for unusual background rates through the script `analyze_ltcsv`, so we removed those points falling outside  $\pm 3\sigma$  from the mean value. Finally, we have applied a filter to the energy

**Table 3.1.** The SZ parameters for the galaxy clusters in our sample. For each object different columns report the name, the central value ( $y_0$ ) of the Compton  $y$ -parameter, the SZ flux integrated up to an overdensity of 2500 and over a fixed solid angle  $\Omega = 1$  arcmin ( $y_{2500}$  and  $y_\Omega$ , respectively) divided by the function  $g_{(x,T_e)}$  (see Eq. 2.24), and the parameter  $\eta$  (see text). For two objects (namely A1914 and RXJ2228+2037) the corresponding errors are not provided by McCarthy et al. (2003b): in the following analysis we will assume for them a formal  $1\sigma$  error of 20 per cent.

name	$y_0$ ( $\times 10^4$ )	$y_{2500}$ (mJy)	$y_\Omega$ (mJy)	$\eta$
A1413	$1.61^{0.20}_{-0.22}$	$40.3 \pm 5.2$	$7.67 \pm 1.00$	0.99
A2204	$1.80^{0.46}_{-0.62}$	$53.1 \pm 16.0$	$7.91 \pm 2.38$	0.79
A1914	1.59	$26.2 \pm 5.2$	$6.41 \pm 1.28$	1.20
A2218	$1.37^{0.18}_{-0.26}$	$25.7 \pm 4.1$	$6.62 \pm 1.04$	1.03
A665	$1.37^{0.26}_{-0.31}$	$37.1 \pm 7.7$	$8.12 \pm 1.69$	0.92
A1689	$3.24^{0.22}_{-0.20}$	$56.8 \pm 3.7$	$13.34 \pm 0.86$	0.94
A520	$1.24^{0.17}_{-0.19}$	$38.8 \pm 5.6$	$7.53 \pm 1.08$	1.10
A2163	$3.56^{0.25}_{-0.27}$	$142.6 \pm 10.5$	$22.69 \pm 1.67$	0.74
A773	$2.37^{0.28}_{-0.32}$	$34.8 \pm 4.4$	$10.99 \pm 1.41$	0.95
A2261	$3.18^{0.35}_{-0.40}$	$39.5 \pm 4.6$	$12.40 \pm 1.46$	0.92
A2390	$3.57^{0.42}_{-0.42}$	$78.4 \pm 9.2$	$17.39 \pm 2.05$	0.75
A1835	$4.70^{0.31}_{-0.29}$	$48.3 \pm 3.1$	$16.44 \pm 1.06$	0.80
A697	$2.65^{0.32}_{-0.32}$	$44.1 \pm 5.3$	$13.88 \pm 1.66$	0.96
A611	$1.60^{0.24}_{-0.24}$	$11.2 \pm 1.7$	$5.39 \pm 0.82$	1.02
Zw3146	$1.61^{0.25}_{-0.29}$	$15.8 \pm 2.6$	$5.67 \pm 0.93$	0.92
A1995	$1.92^{0.14}_{-0.16}$	$18.6 \pm 1.5$	$8.22 \pm 0.65$	1.06
MS1358.4+6245	$1.47^{0.16}_{-0.18}$	$13.4 \pm 1.5$	$5.87 \pm 0.68$	0.75
A370	$2.36^{0.84}_{-0.45}$	$18.9 \pm 5.2$	$10.42 \pm 2.84$	1.19
RXJ2228+2037	2.40	$14.9 \pm 3.0$	$10.76 \pm 2.15$	0.88
RXJ1347.5-1145	$7.41^{0.63}_{-0.68}$	$44.4 \pm 3.9$	$19.60 \pm 1.74$	0.70
MS0015.9+1609	$2.33^{0.19}_{-0.20}$	$11.5 \pm 1.0$	$10.55 \pm 0.89$	0.97
MS0451.6-0305	$2.69^{0.17}_{-0.19}$	$12.5 \pm 0.8$	$9.04 \pm 0.60$	1.31
MS1137.5+6625	$1.53^{0.17}_{-0.19}$	$2.4 \pm 0.3$	$2.73 \pm 0.32$	1.16
EMSS1054.5-0321	$3.87^{1.19}_{-1.12}$	$11.8 \pm 3.5$	$13.93 \pm 4.16$	1.04

(300-9500 keV) and CCDs, so as to obtain an events 2 file.

### 3.2.2 Spatial and spectral analysis

The images have been extracted from the events 2 files in the energy range (0.5-5.0 keV), corrected by using the exposure map to remove the vignetting effects, by masking out the point sources. So as to determine the centroid ( $x_c, y_c$ ) of the surface brightness we have fitted the images with a circular one-dimensional (1D) isothermal  $\beta$ -model (Cavaliere & Fusco-Femiano, 1976), by adding a constant brightness model, and leaving  $x_c$  and  $y_c$  free as parameters in the best fit. We constructed a set of  $n$  ( $n \sim 15 - 40$ ) circular annuli around the centroid of the surface brightness up to a maximum distance  $R_{\text{spat}}$  (also reported in Table 3.2), selecting the radii according to the following criteria: the number

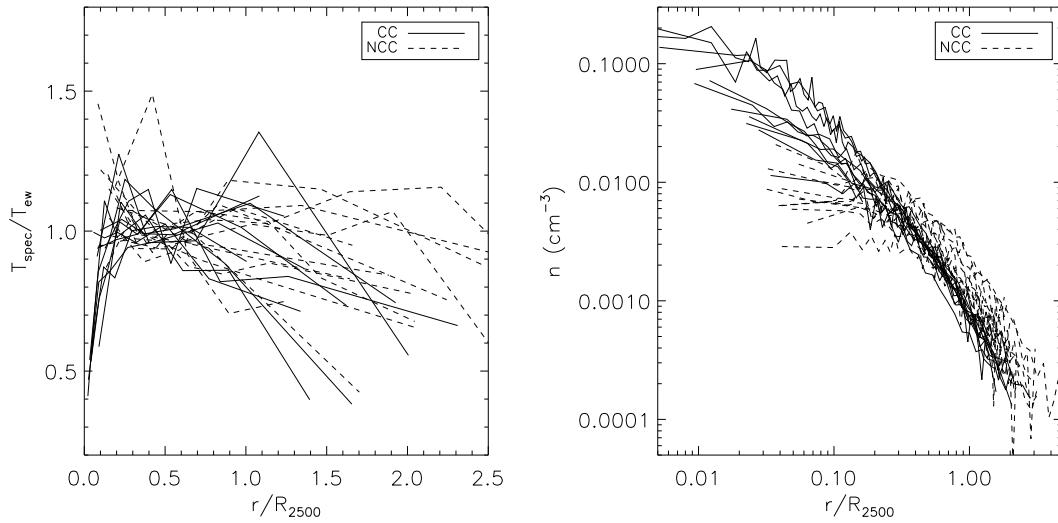


**Figure 3.1.** The radial profiles for the projected temperature  $T_{\text{spec}}$ , normalized using the cooling-core corrected temperature  $T_{\text{ew}}$ , and for density are shown for all objects of our sample in the left and right panels, respectively. Solid and dashed lines refer to clusters with or without a central cooling flow, respectively

of net counts of photons from the source in the (0.5-5.0 keV) band is at least 200-1000 per annulus and the signal-to-noise ratio is always larger than 2. The background counts have been estimated from regions of the same exposure which are free from source emissions.

The spectral analysis has been performed by extracting the source spectra from  $n^*$  ( $n^* \sim 3 - 8$ ) circular annuli of radius  $r_m$  around the centroid of the surface brightness. We have selected the radius of each annulus out to a maximum distance  $R_{\text{spec}}$  (reported in Table 3.2), according to the following criteria: the number of net counts of photons from the source in the band used for the spectral analysis is at least 2000 per annulus and corresponds to a fraction of the total counts always larger than 30 per cent.

The background spectra have been extracted from regions of the same exposure in the case of the ACIS-I data, for which we always have some areas free from source emission. Conversely, for the ACIS-S data we have considered the ACIS-S3 chip only and we have equally used the local background, but we have checked for systematic errors due to possible source contamination of the background regions. This is done considering also the ACIS “blank-sky” background files, which we have re-processed if their gain file does not match the one of the events 2 file; then we have applied the aspect solution files of the observation to the background dataset by using `reproject_events`, so as to estimate the background for our data. We have verified that the spectra produced by the two methods are in good agreement, and at last we decided to show only the results obtained using the local background.

All the point sources has been masked out by visual inspection. Then we have calculated the redistribution matrix files (RMF) and the ancillary response files (ARF) for each annulus: in particular we have used the tools `mkacisrmf` and `mkrmf` (for the data at 120 K and at 110 K, respectively) to calculate the RMF, and the tool `mkarf` to derive

**Table 3.2.** The X-ray properties of the galaxy clusters in our sample. For each object different columns report the name, the redshift  $z$ , the identification number of the *Chandra* observation, the used ACIS mode, the exposure time  $t_{\text{exp}}$ , the neutral hydrogen absorption  $N_{\text{H}}$  (the labels  $f$  and  $t$  refer to objects for which  $N_{\text{H}}$  has been fixed to the Galactic value or thawed, respectively), the physical scale corresponding to 1 arcmin, the maximum radii used for the spatial and for the spectral analysis ( $R_{\text{spat}}$  and  $R_{\text{spec}}$ , respectively), the emission-weighted temperature  $T_{\text{ew}}$ , the metallicity  $Z$  (in solar units), a flag for the presence or not of a cooling core (labeled CC and NCC, respectively), the mass-weighted temperature  $T_{\text{mw}}$ , the gas mass  $M_{\text{gas}}$ , and the bolometric X-ray luminosity  $L$ . The last three columns refer to an overdensity of 2500. Sources extracted from the McCarthy et al. (2003b) sample and from the Benson et al. (2004) sample are indicated by apices (1) and (2), respectively.

name	$z$	obs. ACIS mode	$t_{\text{exp}}$ (ks)	$N_{\text{H}}$ ( $10^{20}\text{cm}^{-2}$ )	1' scale (kpc)	$R_{\text{spat}}$ (kpc)	$R_{\text{spec}}$ (kpc)	$T_{\text{ew}}$ (keV)	$Z$ ( $Z_{\odot}$ )	CC/ NCC	$T_{\text{mw}}$ (keV)	$M_{\text{gas}}$ ( $10^{13}M_{\odot}$ )	$L$ ( $10^{45}\text{erg/s}$ )
A1413 <sup>(1)</sup>	0.143	1661 I	9.7	2.2( $f$ )	151	1111	1359	$6.25^{+0.36}_{-0.33}$	$0.45^{+0.11}_{-0.10}$	CC	$6.58 \pm 0.42$	$2.87 \pm 0.09$	$1.28 \pm 0.03$
A2204 <sup>(1)</sup>	0.152	6104 I	9.6	5.7( $f$ )	159	1183	1262	$9.18^{+0.75}_{-0.65}$	$0.49^{+0.14}_{-0.13}$	CC	$10.52 \pm 0.62$	$5.64 \pm 0.18$	$4.21 \pm 0.14$
A1914 <sup>(1)</sup>	0.171	3593 I	18.8	0.9( $f$ )	175	1449	1576	$8.93^{+0.48}_{-0.45}$	$0.23^{+0.07}_{-0.07}$	NCC	$8.90 \pm 0.43$	$3.94 \pm 0.09$	$1.88 \pm 0.05$
A2218 <sup>(1)</sup>	0.176	1666 I	36.1	3.2( $f$ )	179	1231	1320	$6.88^{+0.33}_{-0.30}$	$0.27^{+0.06}_{-0.06}$	NCC	$6.67 \pm 0.24$	$2.42 \pm 0.07$	$0.84 \pm 0.02$
A665 <sup>(1)</sup>	0.182	3586 I	29.1	4.2( $f$ )	184	1589	1476	$7.14^{+0.33}_{-0.31}$	$0.28^{+0.06}_{-0.06}$	NCC	$7.02 \pm 0.20$	$2.61 \pm 0.08$	$1.22 \pm 0.03$
A1689 <sup>(1)</sup>	0.183	1663 I	10.6	1.8( $f$ )	185	1446	1059	$8.72^{+0.63}_{-0.56}$	$0.23^{+0.10}_{-0.10}$	CC	$6.97 \pm 1.19$	$5.24 \pm 0.14$	$3.15 \pm 0.09$
A520 <sup>(1)</sup>	0.199	4215 I	66.2	3.5( $t$ )	197	1327	1455	$8.24^{+0.31}_{-0.28}$	$0.32^{+0.05}_{-0.05}$	NCC	$9.70 \pm 0.55$	$3.47 \pm 0.09$	$0.92 \pm 0.02$
A2163 <sup>(1)</sup>	0.203	1653 I	71.1	17.5( $t$ )	200	1846	1807	$12.00^{+0.28}_{-0.26}$	$0.24^{+0.03}_{-0.03}$	NCC	$11.70 \pm 0.41$	$6.71 \pm 0.07$	$4.80 \pm 0.05$
A773 <sup>(1)</sup>	0.217	5006 I	19.8	1.4( $f$ )	211	1105	1384	$7.23^{+0.62}_{-0.52}$	$0.37^{+0.12}_{-0.12}$	NCC	$7.09 \pm 0.36$	$2.34 \pm 0.11$	$1.13 \pm 0.04$
A2261 <sup>(1)</sup>	0.224	5007 I	24.3	3.3( $f$ )	216	1588	1595	$7.47^{+0.53}_{-0.47}$	$0.37^{+0.10}_{-0.10}$	CC	$7.56 \pm 0.38$	$3.28 \pm 0.08$	$2.02 \pm 0.07$
A2390 <sup>(2)</sup>	0.232	4193 S	92.0	8.3( $t$ )	222	1205	873	$10.18^{+0.23}_{-0.21}$	$0.29^{+0.03}_{-0.03}$	CC	$10.02 \pm 0.16$	$6.98 \pm 0.08$	$4.66 \pm 0.05$
A1835 <sup>(1)</sup>	0.253	495 S	10.3	2.3( $f$ )	237	914	970	$8.62^{+0.60}_{-0.54}$	$0.44^{+0.12}_{-0.12}$	CC	$8.75 \pm 0.80$	$5.89 \pm 0.60$	$5.58 \pm 0.22$
A697 <sup>(1)</sup>	0.282	4217 I	19.5	1.0( $t$ )	256	1865	1679	$10.21^{+0.83}_{-0.75}$	$0.36^{+0.11}_{-0.11}$	NCC	$9.89 \pm 0.67$	$4.21 \pm 0.21$	$2.52 \pm 0.09$
A611 <sup>(1)</sup>	0.288	3194 S	35.1	5.0( $f$ )	260	969	1172	$6.06^{+0.38}_{-0.34}$	$0.31^{+0.09}_{-0.08}$	CC	$6.32 \pm 0.37$	$2.46 \pm 0.07$	$1.25 \pm 0.03$
Zw3146 <sup>(1)</sup>	0.291	909 I	46.0	3.0( $f$ )	262	1061	1287	$7.35^{+0.27}_{-0.26}$	$0.26^{+0.05}_{-0.05}$	CC	$8.48 \pm 0.30$	$5.56 \pm 0.15$	$4.32 \pm 0.11$
A1995 <sup>(1)</sup>	0.319	906 S	44.5	1.4( $f$ )	279	877	914	$7.56^{+0.45}_{-0.41}$	$0.38^{+0.09}_{-0.09}$	CC	$7.75 \pm 0.48$	$3.39 \pm 0.11$	$1.51 \pm 0.05$
MS1358.4+6245 <sup>(1)</sup>	0.327	516 S	34.1	3.2( $t$ )	283	796	813	$7.51^{+0.70}_{-0.61}$	$0.38^{+0.15}_{-0.14}$	CC	$8.05 \pm 0.58$	$2.98 \pm 0.15$	$1.37 \pm 0.06$
A370 <sup>(1)</sup>	0.375	515 S	48.6	3.1( $f$ )	310	926	762	$7.37^{+0.58}_{-0.53}$	$0.28^{+0.10}_{-0.10}$	NCC	$7.73 \pm 0.41$	$3.35 \pm 0.14$	$1.11 \pm 0.04$
RXJ2228+2037 <sup>(1)</sup>	0.421	3285 I	19.8	4.9( $f$ )	332	1320	1636	$6.86^{+0.89}_{-0.71}$	$0.35^{+0.15}_{-0.15}$	NCC	$7.48 \pm 0.81$	$2.36 \pm 0.15$	$1.64 \pm 0.08$
RXJ1347.5-1145 <sup>(1)</sup>	0.451	3592 I	57.7	4.9( $f$ )	346	1558	1560	$13.92^{+1.14}_{-0.93}$	$0.19^{+0.08}_{-0.09}$	CC	$15.32 \pm 0.83$	$8.99 \pm 0.19$	$8.84 \pm 0.38$
MS0015.9+1609 <sup>(1)</sup>	0.546	520 I	67.4	4.1( $f$ )	383	1889	849	$8.29^{+0.49}_{-0.43}$	$0.32^{+0.06}_{-0.06}$	NCC	$8.00 \pm 0.37$	$3.13 \pm 0.09$	$2.46 \pm 0.06$
MS0451.6-0305 <sup>(1)</sup>	0.550	902 S	41.1	5.1( $f$ )	385	1092	1325	$9.09^{+0.70}_{-0.61}$	$0.29^{+0.10}_{-0.09}$	NCC	$8.99 \pm 1.15$	$6.21 \pm 0.72$	$3.92 \pm 0.12$
MS1137.5+6625 <sup>(1)</sup>	0.784	536 I	116.4	3.5( $t$ )	447	706	880	$5.48^{+0.89}_{-0.71}$	$0.25^{+0.25}_{-0.22}$	NCC	$6.28 \pm 0.57$	$1.73 \pm 0.10$	$1.00 \pm 0.06$
EMSS1054.5-0321 <sup>(2)</sup>	0.823	512 S	71.1	3.6( $f$ )	455	763	895	$9.00^{+1.39}_{-1.10}$	$0.25^{+0.17}_{-0.17}$	NCC	$9.38 \pm 1.31$	$2.55 \pm 0.18$	$1.35 \pm 0.13$

the ARF of the regions.

For each of the  $n^*$  annuli the spectra have been analyzed by using the package XSPEC (Arnaud, 1996) after grouping the photons into bins of 20 counts per energy channel (using the task `grppha` from the FTOOLS software package) and applying the  $\chi^2$ -statistics. The spectra are fitted with a single-temperature absorbed MEKAL model (Kaastra, 1992; Liedahl et al., 1995) multiplied by a positive absorption edge as described in Vikhlinin et al. (2005): this procedure takes into account a correction to the effective area consisting in a 10 per cent decrement above 2.07 keV. The fit is performed in the energy range 0.6–7 keV (0.6–5 keV for the outermost annulus only) by fixing the redshift to the value obtained from optical spectroscopy and the absorbing equivalent hydrogen column density  $N_{\text{H}}$  to the value of the Galactic neutral hydrogen absorption derived from radio data (Dickey & Lockman, 1990), except for A520, A697, A2163, MS1137.5+6625, MS1358.4+6245 and A2390, where we have decided to leave  $N_{\text{H}}$  free due to the inconsistency between the tabulated radio data and the spectral fit result. Apart for these objects where also the Galactic absorption is left free, we consider three free parameters in the spectral analysis for  $m$ -th annulus: the normalization of the thermal spectrum  $K_m \propto \int n_e^2 dV$ , the emission-weighted temperature  $T_{\text{proj},m}^*$ ; the metallicity  $Z_m$  retrieved by employing the solar abundance ratios from Anders & Grevesse (1989). The best-fit spectral parameters are listed in Table 3.2.

The total (cooling-core corrected) temperature  $T_{\text{ew}}$  has been extracted in a circular region of radius  $R$ , with  $100 \text{ kpc} < R < R_{\text{spec}}$ , centred on the symmetrical centre of the brightness distribution. In the left panel of Fig. 3.1 we present for all clusters of our sample the projected temperature profile ( $T_{\text{spec}}$ ) normalized by  $T_{\text{ew}}$  as a function of the distance from the centre  $R$ , given in units of  $R_{2500}$ , where  $R_{2500}$  is the radius corresponding to an overdensity of 2500.

### 3.2.3 Spectral deprojection analysis

To measure the pressure and gravitating mass profiles in our clusters, we deproject the projected physical properties obtained with the spectral analysis by using an updated and extended version of the technique presented in Ettori et al. (2002) and discussed in full detail in Appendix A. Here we summarize briefly the main characteristics of the adopted technique: (i) the electron density  $n_e(r)$  is recovered both by deprojecting the surface brightness profile and the spatially resolved spectral analysis obtaining a few tens of radial measurements; (ii) once a functional form of the DM density profile  $\rho = \rho(\mathbf{r}, \mathbf{q})$ , where  $\mathbf{q} = (q_1, q_2, \dots, q_h)$  are free parameters of the DM analytical model, and the gas pressure  $P_0$  at  $R_{\text{spec}}$  are assumed, the deprojected gas temperature,  $T(\mathbf{q}, P_0)$ , is obtained by integration of the hydrostatic equilibrium equation:

$$P(r, \mathbf{q}, P_0) = P_0 - \int_{R_{\text{spec}}}^r n_{\text{gas}}(s) \mu m_H \frac{G M(\mathbf{q}, s)}{s^2} ds, \quad (3.1)$$

where  $\mu = 0.6$  is the average molecular weight,  $m_H$  is the proton mass. So  $T(\mathbf{q}, P_0) = P(\mathbf{q}, P_0)/n_{\text{gas}}$  expressed in keV units. In the present study, to parametrize the cluster mass

distribution, we consider two models: the universal density profile proposed by Navarro et al. (1997) (hereafter NFW) and the one suggested by Rasia et al. (2004) (hereafter RTM).

The NFW profile is given by

$$\rho(x) = \frac{\rho_{c,z} \delta_{c,\text{NFW}}}{(x/x_s)(1+x/x_s)^2}, \quad (3.2)$$

where  $\rho_{c,z} \equiv 3H(z)^2/8\pi G$  is the critical density of the universe at redshift  $z$ ,  $H_z \equiv E_z H_0$ ,  $E_z = [\Omega_M(1+z)^3 + (1 - \Omega_M - \Omega_\Lambda)(1+z)^2 + \Omega_\Lambda]^{1/2}$ , and

$$\delta_{c,\text{NFW}} = \frac{\Delta}{3} \frac{c^3}{\ln(1+c) - c/(1+c)}, \quad (3.3)$$

where  $c \equiv r_{\text{vir}}/r_s$  is the concentration parameter,  $r_s$  is the scale radius,  $x \equiv r/r_{\text{vir}}$ ,  $x_s \equiv r_s/r_{\text{vir}}$ .

The RTM mass profile is given by:

$$\rho(x) = \frac{\rho_{c,z} \delta_{c,\text{RTM}}}{x(x+x_s^*)^{3/2}}, \quad (3.4)$$

with  $x_s^* \equiv r_s^*/r_{\text{vir}}$ , where  $r_s^*$  is a reference radius and  $\delta_{c,\text{RTM}}$  is given by:

$$\delta_{c,\text{RTM}} \equiv \frac{\Delta}{6 [(1+2x_s^*)/(1+x_s^*)^{1/2} - 2x_s^{*1/2}]}. \quad (3.5)$$

So we have  $\mathbf{q} = (c, r_s)$  and  $\mathbf{q} = (x_s, r_{200})$  for the NFW and RTM models, respectively.

The comparison of the observed projected temperature profile  $T_{\text{proj},m}^*$  (Sect. 3.2.2) with the deprojected  $T(\mathbf{q}, P_0)$  (Eq. A.7 in Appendix A), once the latter has been re-projected by correcting for the temperature gradient along the line of sight as suggested in Mazzotta et al. (2004), provides the best estimate of the free parameters  $(\mathbf{q}, P_0)$  through a  $\chi^2$  minimization, and therefore of  $T(\mathbf{q}, P_0)$  (see an example in Figure 3.2.3).

In the right panel of Fig. 3.1 we present the density profiles (plotted versus  $r/R_{2500}$ ) as determined through the previous method. In general, we find there is no significant effect on the determination of the physical parameters when adopting the two different DM models. Hereafter we will use the physical parameters determined using the RTM model, reported with their corresponding errors in Table 3.2, where we also list the exposure time, the number and the instrument (ACIS-I or ACIS-S) used for each of the *Chandra* observations.

Finally we computed the total mass enclosed in a sphere of radius  $R_\Delta$  as  $M(\mathbf{q})(< R_\Delta) = \int_0^{R_\Delta} \rho(r, \mathbf{q}) dV$  where the radius  $R_\Delta$  corresponds to a given overdensity  $\Delta$ : we considered the cases where the overdensity is equal to 2500 and 500. The values for masses and radii, together with the parameters  $(\mathbf{q}, P_0)$  for the RTM model, are reported in Table 3.3. The errors on the different quantities represent the 68.3 per cent confidence level and are computed by looking to the regions in the parameter space where the reduction of  $\chi^2$  with

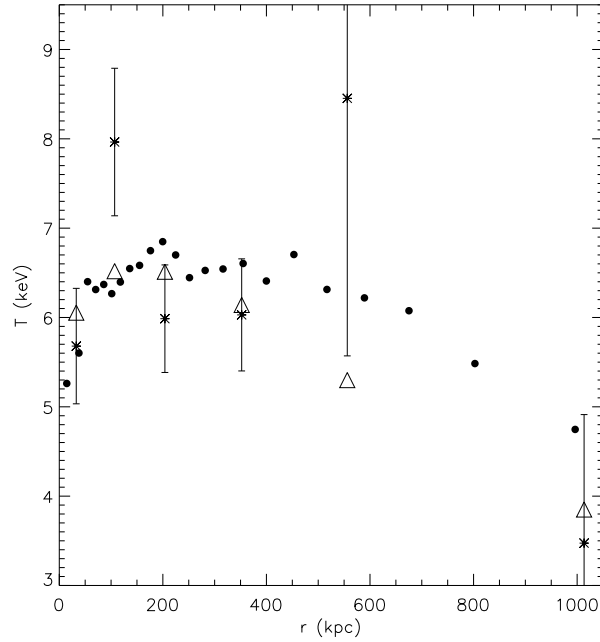


**Figure 3.2.** Example of temperature spectral deprojection for cluster A1413. We display the two quantities which enter in the Eq. (A.7) in the spectral deprojection analysis to retrieve the physical parameters: the observed spectral projected temperature  $T_{\text{proj},m}^*$  (stars with errorbars) and the theoretical projected temperature (triangles, indicated as  $T_{\text{proj},m}$  in Appendix A). We also show the theoretical deprojected temperature  $T(\mathbf{q}, P_0)$  (points), which generates  $T_{\text{proj},m}$  through convenient projection techniques.

respect to its minimum value  $\chi_{\text{min}}^2$  is smaller than a given threshold, fixed according to the number of degrees of freedom d.o.f. (see, e.g., Press et al., 1992). Notice that we included in the Eq. (3.1) the statistical errors related to measurement errors of  $n_{\text{gas}}(r)$ .

### 3.2.4 Determination of the X-ray properties

The bolometric X-ray luminosity  $L(< R_{\Delta})$  has been calculated by correcting the observed luminosity  $L(100 \text{ kpc} < r < R_{\text{spec}})$  determined from the spectral analysis performed by XSPEC excluding the central cooling region of 100 kpc (the results are reported in Table 3.2):

$$L(< R_{\Delta}) = L(100 \text{ kpc} < r < R_{\text{spec}}) \frac{\int_0^{x_{\Delta}} (1+x^2)^{-3\beta} x^2 dx}{K_{\text{corr}}}, \quad (3.6)$$

where  $x = r/r_c$ ,  $x_{\Delta} = R_{\Delta}/r_c$ ,  $r_c$  and  $\beta$  are the best-fit parameters of the  $\beta$ -model on the image brightness,  $K_{\text{corr}}$  is the normalization of the thermal spectrum drawn with XSPEC, and corrected for the emission from the spherical source up to 10 Mpc intercepted by the line of sight:  $K_{\text{corr}} = \int_{x_0}^{x_1} (1+x^2)^{-3\beta} x^2 dx + \int_{x_1}^{x_2} (1+x^2)^{-3\beta} x^2 (1 - \cos \theta) dx - \int_{x_0}^{x_2} (1+x^2)^{-3\beta} x^2 (1 - \cos \theta^*) dx$ , with  $\theta = \arcsin(x_1/x)$ ,  $\theta^* = \arcsin(x_0/x)$ ,  $x_0 = 100 \text{ kpc}/r_c$ ,  $x_1 = R_{\text{spec}}/r_c$  and  $x_2 = 10 \text{ Mpc}/r_c$ .

**Table 3.3.** Different physical properties for the clusters in our sample. For each object the different columns report the name, the minimum value for  $\chi^2$  (with the corresponding number of degrees of freedom d.o.f.), the virial radius  $r_{\text{vir}}$ , the reference scale  $x_s$ , the value of the pressure  $P_0$ , the mass and the radius corresponding to an overdensity of 2500 ( $M_{2500}$  and  $R_{2500}$ , respectively), the mass and the radius corresponding to an overdensity of 500 ( $M_{500}$  and  $R_{500}$ , respectively). All quantities are derived by assuming the RTM model.

name	$\chi^2_{\text{min}}$ (d.o.f.)	$r_{\text{vir}}$ (kpc)	$x_s$	$P_0$ ( $10^{-12}$ erg cm $^{-3}$ )	$M_{2500}$ ( $10^{14}M_{\odot}$ )	$R_{2500}$ (kpc)	$M_{500}$ ( $10^{14}M_{\odot}$ )	$R_{500}$ (kpc)
A1413	5.29(3)	1853 ± 255	0.11 ± 0.05	1.87 ± 0.48	2.30(±0.46)	520(±57)	5.58(±2.25)	1195(±232)
A2204	4.24(5)	2840 ± 357	0.16 ± 0.03	0.73 ± 0.71	6.74(±1.40)	742(±91)	19.12(±6.68)	1796(±320)
A1914	2.29(5)	1809 ± 202	0.03 ± 0.03	1.98 ± 0.64	3.39(±0.76)	586(±61)	5.99(±2.28)	1212(±202)
A2218	0.61(2)	1653 ± 180	0.06 ± 0.04	1.53 ± 0.33	2.14(±0.30)	502(±36)	4.36(±1.33)	1088(±152)
A665	1.23(5)	2177 ± 359	0.31 ± 0.16	1.72 ± 0.44	1.88(±0.16)	480(±30)	7.77(±2.71)	1317(±260)
A1689	0.68(4)	2159 ± 323	0.09 ± 0.04	1.24 ± 1.05	4.14(±0.95)	624(±76)	9.40(±3.65)	1402(±260)
A520	0.08(3)	2487 ± 1340	0.23 ± 0.74	1.58 ± 0.57	3.72(±0.93)	599(±102)	12.66(±8.50)	1540(±546)
A2163	3.00(5)	4884 ± 637	1.46 ± 0.46	1.44 ± 0.26	4.07(±0.69)	616(±102)	52.58(±10.72)	2472(±396)
A773	1.38(2)	1672 ± 486	0.09 ± 0.14	2.90 ± 0.51	2.01(±0.45)	485(±60)	4.54(±3.49)	1087(±388)
A2261	2.82(3)	1851 ± 191	0.10 ± 0.03	0.87 ± 0.46	2.68(±0.44)	532(±46)	6.17(±1.79)	1201(±168)
A2390	23.08(4)	3557 ± 497	0.41 ± 0.11	2.66 ± 0.81	6.59(±0.64)	716(±52)	33.22(±9.88)	2099(±373)
A1835	0.80(1)	2259 ± 413	0.14 ± 0.05	5.92 ± 1.70	4.09(±1.34)	606(±113)	10.95(±6.39)	1439(±414)
A697	1.17(4)	2251 ± 1491	0.21 ± 0.72	2.69 ± 2.77	3.23(±0.88)	554(±94)	10.46(±8.47)	1402(±588)
A611	0.81(3)	1719 ± 242	0.12 ± 0.05	2.14 ± 0.59	2.11(±0.45)	480(±56)	5.18(±2.15)	1107(±222)
Zw3146	4.36(3)	2984 ± 403	0.31 ± 0.07	1.26 ± 0.86	5.41(±0.81)	656(±68)	22.50(±7.58)	1804(±344)
A1995	3.05(2)	2585 ± 2042	0.32 ± 0.67	3.41 ± 2.84	3.51(±1.32)	562(±149)	14.96(±13.96)	1558(±804)
MS1358.4+6245	0.60(1)	2748 ± 2134	0.38 ± 0.66	3.67 ± 3.11	3.62(±1.64)	566(±184)	17.37(±16.70)	1633(±885)
A370	4.21(1)	2195 ± 822	0.23 ± 0.33	0.06 ± 1.44	3.10(±0.74)	528(±82)	10.58(±7.70)	1359(±518)
RXJ2228+2037	0.12(2)	1648 ± 1164	0.19 ± 0.73	3.11 ± 1.72	1.59(±0.46)	415(±90)	4.90(±4.35)	1033(±464)
RXJ1347.5-1145	3.58(5)	2703 ± 187	0.13 ± 0.02	0.01 ± 0.15	9.49(±1.26)	744(±56)	24.00(±4.75)	1734(±170)
MS0015.9+1609	0.96(4)	2129 ± 433	0.48 ± 0.39	0.24 ± 0.55	1.72(±0.25)	406(±50)	9.75(±2.82)	1237(±224)
MS0451.6-0305	0.14(5)	2118 ± 1915	0.21 ± 0.73	3.63 ± 3.24	3.68(±1.43)	522(±130)	11.89(±12.85)	1320(±725)
MS1137.5+6625	2.12(1)	1468 ± 284	0.17 ± 0.13	0.13 ± 0.47	1.91(±0.48)	382(±58)	5.47(±2.79)	928(±238)
EMSS1054.5-0321	0.03(1)	3060 ± 1666	1.39 ± 0.75	5.58 ± 7.61	2.17(±1.26)	393(±168)	27.21(±21.81)	1560(±930)

The gas mass  $M_{\text{gas}}$  enclosed in a circular region having overdensity  $\Delta$  has been computed from the total gas density  $n_{\text{gas},j}$ , that we directly obtained from the spectral deprojection, up to  $R_{\text{spec}}$ . We have checked that the exclusion of the central cooling region does not significantly affect the resulting values for  $M_{\text{gas}}$ .

Finally we have estimated the total mass-weighted temperature:

$$T_{\text{mw}} \equiv \left( \sum_{i=1}^p T_j(\mathbf{q}, P_0) m_i \right) / \sum_{i=1}^p m_i \quad (3.7)$$

which can be compared to the total emission-weighted temperature  $T_{\text{ew}}$ ;  $p$  represents the number of annuli inside  $R_{2500}$ . Notice that our average deprojected temperature profile implies the following relation between the maximum, the deprojected and the mass-weighted temperatures:  $T_{\text{max}} : T_{\text{ew}} : T_{\text{mw}} = 1 : 0.67 : 0.69$  ( $1 : 0.83 : 0.88$  for the CC-only subsample). The physical parameters obtained in this way are also listed in Table 3.2 for all clusters of our sample.

### 3.2.5 Determination of the Sunyaev-Zel'dovich properties

In Sect. 2.4 we have seen that the thermal SZ effect is a very small distortion of the spectra of the cosmic microwave background, due to the Inverse Compton scattering between the photons of the CMB and the hot ( $\sim 10^7 - 10^8$  K) electrons of the ICM trapped in the gravitational potential well of the dark matter halo (Sunyaev & Zeldovich, 1970; Birkinshaw, 1999). We can parameterize the magnitude of this effect by considering the Compton parameter  $y \propto \int P_e(r) dl$ , which is proportional to integral of the electronic pressure  $P_e$  of the ICM along the line of the sight  $l$  (see Sect. 2.4). We consider the Compton- $y$  parameter integrated over the entire solid angle (and given in flux units)  $y_\Delta$  defined as:

$$y_\Delta = I_0 \int_0^{\theta_\Delta} y(\theta) d\Omega ; \quad (3.8)$$

To remove the dependence of  $y_\Delta$  on the angular diameter distance  $d_a(z)$  we use the intrinsic integrated Compton parameter  $Y$ , defined as:

$$Y \equiv d_a^2(z) y_\Delta. \quad (3.9)$$

The same quantity, but integrated over a fixed solid angle  $\Omega$ , can be similarly written as:

$$y_\Omega = I_0 \int_0^\Omega y(\theta) d\Omega . \quad (3.10)$$

We fixed  $\Omega = 1$  arcmin, that is  $\lesssim$  than the field of view of OVRO, used in the observations of most of the sources in our sample (see, e.g., McCarthy et al., 2003a). Notice that in order to remove the frequency dependence we have normalized  $Y$ ,  $y_\Delta$  and  $y_\Omega$  to  $g_{(x, T_e)}$ .

To integrate Eq. (3.8) and (3.10) we have recovered  $y(\theta)$  from Eq. (2.20) by using the pressure profile  $P(\mathbf{q}, P_0)$  determined in the spectral analysis (Sect. 3.2.3), renormalized in such a way that  $y(0)$  equals the central Compton parameter  $y_0$  taken from the literature.

This method can lead to systematics on  $y_\Omega$  and  $Y$  due to the fact that, even if we are assuming the true pressure profiles  $P(r)$  in Eq. (2.20),  $y_0$  has been obtained by assuming an isothermal  $\beta$ -model inferred from the brightness profile. The value of  $y_0$  is thus potentially dependent on the underlying model of  $P(r)$ . As discussed in recent works (see, e.g., LaRoque et al., 2006; Bonamente et al., 2006), the relaxation of the isothermal assumption should apply to the analysis of both X-ray and SZ data, to obtain a robust and consistent description of the physics acting inside galaxy clusters. Unfortunately, we have only the central Compton parameter, and not the complete  $uv$ -data, which are not public available: so it is very difficult to quantify the amplitude of this systematics, being  $y_0$  determined through a best fit in the  $uv$ -plane.

Nevertheless, we can give an estimate in this way: we have computed the central Compton parameter  $y_{0,X}^I$  inferred from the X-ray data by parameterizing first  $P(r)$  in Eq. (2.20) with a  $\beta$ -model inferred on the brightness images:

$$y_0 = \frac{\sigma_T}{m_e c^2} n_0 k T_{\text{gas}} \int dx (1+x^2)^{(1-3\beta)/2} \quad (3.11)$$

with  $n_0 = n_{\text{gas}}(r=0)$  derived from the brightness profile  $B(r)$ :

$$B(r=0) = \frac{1}{4\pi(1+z)^4} r_c \Lambda 0.82 n_0^2 \int dx (1+x^2)^{1/2-3\beta} \quad (3.12)$$

where  $\Lambda$  is the X-ray cooling function of the ICM in the cluster rest frame in cgs units ( $\text{erg cm}^3 \text{s}^{-1}$ ) integrated over the energy range of the brightness images (0.5 – 5 keV). Then we have calculated  $y_{0,X}^H$  by accounting in Eq. (2.20) for the true pressure profile  $P(\mathbf{q}, P_0)$  recovered by the spectral deprojection analysis (Sect. 3.2.3), and therefore we determined the ratio  $\eta = y_{0,X}^H / y_{0,X}^I$ . We notice that the parameter  $\eta$  differs from the unity of  $\lesssim 25$  per cent, comparable to statistical errors.

The different quantities related to the SZ effect are listed in Table 3.1 for all clusters in our sample.

### 3.3 The X-ray and SZ scaling relations: theory and fitting procedure

#### 3.3.1 The scaling relations in the self-similar model

The self-similar model (see, e.g., Kaiser , 1986) gives a simple picture of the process of cluster formation in which the ICM physics is driven by the infall of cosmic baryons into the gravitational potential of the cluster DM halo. The collapse and subsequent shocks heat the ICM up to the virial temperature. Thanks to this model, which assumes that gravity is the only responsible for the observed values of the different physical properties of galaxy clusters, we have a simple way to establish theoretical analytic relations between them.

Numerical simulations confirm that the DM component in clusters of galaxies, which represents the dominant fraction of the mass, has a remarkably self-similar behaviour; however the baryonic component does not show the same level of self-similarity. This

picture is confirmed by X-ray observations, see for instance the deviation of the  $L - T$  relation in clusters, which is steeper than the theoretical value predicted by the previous scenario. These deviations from self-similarity have been interpreted as the effects of non-gravitational heating due to radiative cooling as well as the energy injection from supernovae, AGN, star formation or galactic winds (see, e.g., Tozzi & Norman, 2001; Bialek et al., 2001; Borgani et al., 2002; Babul et al., 2002; Borgani et al., 2004; Brighenti & Mathews, 2006) which make the gas less centrally concentrated and with a shallower profile in the external regions with respect the DM component. Consequently, the comparison of the self-similar scaling relations to observations allows us to evaluate the importance of the effects of the non-gravitational processes on the ICM physics.

For  $Y$  and  $y_\Omega$  we have the following dependences on the cosmology:

$$E_z \Delta_z^{1/2} Y \propto \left( E_z^{-1} \Delta_z^{-1/2} y_0 \right) \left( E_z \Delta_z^{1/2} R_{\Delta_z} \right)^2, \quad (3.13)$$

and

$$E_z^{-1} \Delta_z^{-1/2} y_\Omega \propto E_z^{-1} \Delta_z^{-1/2} y_0, \quad (3.14)$$

respectively,

where the factor  $\Delta_z = 200 \times \left[ 1 + 82 (\Omega_z - 1) / (18\pi^2) - 39 (\Omega_z - 1)^2 / (18\pi^2) \right]$ , with  $\Omega_z = \Omega_{0m} (1+z)^3 / E_z^2$ , accounts for evolution of clusters in an adiabatic scenario (Bryan & Norman, 1998).

Assuming the spherical collapse model for the DM halo and the equation of hydrostatic equilibrium to describe the distribution of baryons into the DM potential well, in the self-similar model the cluster mass and temperature are related by:

$$E_z \Delta_z^{1/2} M_{\text{tot}} \propto T^{3/2}; \quad (3.15)$$

so we have  $R_{\Delta_z} \propto (M / (\rho_{c,z} \Delta_z))^{1/3} \propto T^{1/2} E_z^{-1} \Delta_z^{-1/2}$ . By setting  $f_z \equiv E_z (\Delta_z / \Delta)^{1/2}$ , from the previous equations we can easily obtain the following relations (see, e.g., Markevitch, 1998; Allen & Fabian, 1998; Ettori et al., 2004; Arnaud et al., 2005; Diaferio et al., 2005; Vikhlinin et al., 2005; Kotov & Vikhlinin, 2005):

$$f_z(Y) \propto (f_z^{-1} y_0)^{5/3}, \quad (3.16)$$

$$y_\Omega \propto y_0, \quad (3.17)$$

$$f_z^{-1} y_0 \propto T^{3/2}, \quad (3.18)$$

$$f_z^{-1} y_0 \propto f_z M_{\text{tot}}, \quad (3.19)$$

$$f_z^{-1} y_0 \propto (f_z^{-1} L)^{3/4}, \quad (3.20)$$

$$f_z Y \propto T^{5/2} , \quad (3.21)$$

$$f_z Y \propto (f_z M_{\text{tot}})^{5/3} , \quad (3.22)$$

$$f_z Y \propto (f_z^{-1} L)^{5/4} . \quad (3.23)$$

We also remember here that for galaxy clusters similar scaling laws exist also in the X-ray band (see, e.g., Ettori et al., 2004a; Arnaud et al., 2005; Kotov & Vikhlinin, 2005; Vikhlinin et al., 2006):

$$f_z^{-1} L \propto T_{\text{gas}}^2 , \quad (3.24)$$

$$f_z M_{\text{tot}} \propto T_{\text{gas}}^{3/2} , \quad (3.25)$$

$$f_z^{-1} L \propto (f_z M_{\text{tot}})^{4/3} , \quad (3.26)$$

$$f_z M_{\text{gas}} \propto T_{\text{gas}}^{3/2} , \quad (3.27)$$

$$f_z^{-1} L \propto (f_z M_{\text{gas}})^{4/3} . \quad (3.28)$$

In our work we have considered all the physical quantities at fixed overdensity ( $\Delta_z = \Delta$ ), i.e.  $f_z = E_z$  in the above equations.

### 3.3.2 Fitting the scaling relations

We describe here the method adopted to obtain the best-fitting parameters in the scaling relations. Since they are power-law relations, we carry out a log-log fit:

$$\log(Y) = \alpha + A \log(X) , \quad (3.29)$$

where  $X$  and  $Y$  represent the independent and dependent variables, respectively (hereafter  $Y|X$ );  $\alpha$  and  $A$  are the two free parameters to be estimated. However, in the considered scaling relations it is unclear which variable should be considered as (in)dependent. Moreover both  $X$ - and  $Y$ -data have errors due to measurement uncertainties, plus an intrinsic scatter. For these reasons, the ordinary least squares (OLS) minimization approach is not appropriate: in fact it does not take into account intrinsic scatter in the data, and it is biased when errors affect the independent variable. So we decided to use the BCES (Bivariate Correlated Errors and intrinsic Scatter) ( $Y|X$ ) modification or the bisector modification BCES ( $Y, X$ ) proposed by Akritas & Bershady (1996), for which the best-fit results correspond to the bisection of those obtained from minimizations in the vertical and horizontal directions. Both these methods are robust estimators that take into account both any intrinsic scatter and the presence of errors on both variables.

The results for the best-fit normalization  $\alpha$  and slope  $A$  for the listed scaling relations are presented in Table 3.4, where we also report the values of the total scatter

$$S = \left[ \sum_j (\log Y_j - \alpha - A \log X_j)^2 / \nu \right]^{1/2} \quad (3.30)$$

and of the intrinsic scatter  $\hat{S}$  calculated as:

$$\hat{S} = \left[ \sum_j \left( (\log Y_j - \alpha - A \log X_j)^2 - \epsilon_{\log Y_j}^2 \right) / \nu \right]^{1/2}, \quad (3.31)$$

where  $\epsilon_{\log Y_j} = \epsilon_{Y_j} / (Y_j \ln 10)$ , with  $\epsilon_{Y_j}$  being the statistical error of the measurement  $Y_j$ , and  $\nu$  is the number of degrees of freedom ( $\nu = N - 2$ , with  $N$  equal to total number of data).

Notice that in these fits the physical quantities ( $L$ ,  $M_{\text{tot}}$ ,  $M_{\text{gas}}$ ,  $Y$ ) refer to  $R_{2500}$  estimated through the mass estimates based on the RTM model.

### 3.3.3 On the evolution of the scaling relations

We can extend the previous analysis by investigating the redshift evolution of the scaling relations at  $z > 0.1$ . Note that only two objects are available at  $z > 0.6$  and that all CC clusters are at redshift below 0.45. We parametrize the evolution using a  $(1+z)^B$  dependence and put constraints on the value of  $B$  by considering a least-square minimization of the relation

$$\log(Y) = \alpha + A \log(X) + B \log(1+z). \quad (3.32)$$

This is obtained by defining a grid of values of  $B$  and looking for the minimum of a  $\chi^2$ -like function, defined as:

$$\chi^2 = \sum_j \frac{[\log Y_j - \alpha - A \log X_j - B \log(1+z_j)]^2}{\epsilon_{\log Y_j}^2 + \epsilon_{\alpha}^2 + A^2 \epsilon_{\log X_j}^2 + \epsilon_A^2 \log^2 X_j}; \quad (3.33)$$

the sum is over all data, and  $\epsilon_{\log X} \equiv \epsilon_X / (X \ln 10)$  and  $\epsilon_{\log Y} \equiv \epsilon_Y / (Y \ln 10)$  are related to the uncertainties on  $X$  and  $Y$ , respectively. The best-fit parameters values calculated by using this method are reported in Table 3.5. Again in these fits, which refer to same scaling relations presented in Table 3.4, the physical quantities ( $L$ ,  $M_{\text{tot}}$ ,  $M_{\text{gas}}$ ,  $Y$ ) refer to  $R_{2500}$ , and masses are computed by assuming the RTM model.

## 3.4 Discussion of the results

We present here a general discussion of our results concerning the scaling relations. In particular we have chosen to consider both the whole sample (CC plus NCC objects) and

**Table 3.4.** Best-fit parameters for the scaling relations computed by using the cluster quantities evaluated at  $R_{2500}$ ; masses are estimated using the RTM profile. For each relation we give the logarithmic slope  $A$  (compared to the theoretically expected value  $A^*$ ), the normalization  $\alpha$ , the intrinsic scatter  $\hat{S}$  and the logarithmic scatter of the data  $S$ . The results are given both for a subsample including the CC clusters (11 objects), and for the whole sample (24 objects). In the column “method”, symbols (1) and (2) indicate if the fit has been performed by adopting the BCES ( $Y|X$ ) or BCES ( $Y,X$ ) methods, respectively. With the notation ( $y_{0,-4}, y_{\Omega}, Y_8$ ),  $L_{44}$ ,  $T_7$ ,  $M_{14}$ , we indicate the Compton parameter, the X-ray luminosity, the temperature and the mass, in units of ( $10^{-4}$ , mJy,  $10^8$  mJy Mpc $^2$ ),  $10^{44}$  erg s $^{-1}$ , 7 keV,  $10^{14}M_{\odot}$ , respectively.

relation ( $Y - X$ )	Cooling core clusters 11 objects				All clusters 24 objects				
	$A/A^*$	$\alpha$	$\hat{S}$	$S$	$A/A^*$	$\alpha$	$\hat{S}$	$S$	method
$f_z Y_8 - f_z^{-1} y_{0,-4}$	1.22( $\pm 0.15$ )/1.67	-1.07( $\pm 0.06$ )	0.090	0.113	1.19( $\pm 0.20$ )/1.67	-0.91( $\pm 0.06$ )	0.116	0.137	(1)
$y_{\Omega} - y_{0,-4}$	0.93( $\pm 0.14$ )/1.00	0.61( $\pm 0.04$ )	0.033	0.076	0.92( $\pm 0.26$ )/1.00	0.66( $\pm 0.08$ )	0.120	0.140	(1)
$f_z^{-1} y_{0,-4} - T_{\text{ew},7}$	2.21( $\pm 0.32$ )/1.50	0.19( $\pm 0.05$ )	0.138	0.154	2.06( $\pm 0.23$ )/1.50	0.15( $\pm 0.03$ )	0.123	0.141	(2)
$f_z^{-1} y_{0,-4} - f_z M_{\text{tot},14}$	1.25( $\pm 0.30$ )/1.00	-0.50( $\pm 0.22$ )	0.248	0.257	1.22( $\pm 0.29$ )/1.00	-0.41( $\pm 0.17$ )	0.211	0.222	(2)
$f_z^{-1} y_{0,-4} - f_z^{-1} L_{44}$	0.75( $\pm 0.07$ )/0.75	-0.69( $\pm 0.11$ )	0.156	0.170	0.61( $\pm 0.05$ )/0.75	-0.48( $\pm 0.07$ )	0.124	0.142	(2)
$f_z Y_8 - T_{\text{ew},7}$	2.74( $\pm 0.23$ )/2.50	-0.83( $\pm 0.03$ )	0.103	0.124	2.64( $\pm 0.28$ )/2.50	-0.74( $\pm 0.03$ )	0.139	0.157	(2)
$f_z Y_8 - f_z M_{\text{tot},14}$	1.56( $\pm 0.29$ )/1.67	-1.70( $\pm 0.21$ )	0.235	0.245	1.48( $\pm 0.39$ )/1.67	-1.42( $\pm 0.21$ )	0.288	0.297	(2)
$f_z Y_8 - f_z^{-1} L_{44}$	0.92( $\pm 0.11$ )/1.25	-1.92( $\pm 0.16$ )	0.183	0.196	0.81( $\pm 0.07$ )/0.75	-1.58( $\pm 0.10$ )	0.237	0.248	(2)
$f_z^{-1} y_{\Omega} - T_{\text{ew},7}$	1.98( $\pm 0.46$ )/1.50	0.80( $\pm 0.05$ )	0.143	0.158	2.15( $\pm 0.45$ )/1.50	0.79( $\pm 0.05$ )	0.167	0.182	(2)
$f_z^{-1} y_{\Omega} - f_z M_{\text{tot},14}$	1.12( $\pm 0.31$ )/1.00	0.17( $\pm 0.22$ )	0.239	0.249	1.07( $\pm 0.17$ )/1.00	0.31( $\pm 0.10$ )	0.278	0.288	(2)
$f_z^{-1} y_{\Omega} - f_z^{-1} L_{44}$	0.68( $\pm 0.09$ )/0.75	-0.02( $\pm 0.14$ )	0.160	0.174	0.74( $\pm 0.10$ )/0.75	0.00( $\pm 0.15$ )	0.233	0.244	(2)
$f_z^{-1} L_{44} - T_{\text{ew},7}$	2.98( $\pm 0.53$ )/2.00	1.18( $\pm 0.05$ )	0.182	0.183	3.37( $\pm 0.39$ )/2.00	1.03( $\pm 0.05$ )	0.220	0.221	(2)
$f_z^{-1} L_{44} - f_z M_{\text{tot},14}$	1.71( $\pm 0.46$ )/1.33	0.24( $\pm 0.32$ )	0.205	0.206	2.03( $\pm 0.54$ )/1.33	0.08( $\pm 0.32$ )	0.269	0.270	(2)
$f_z M_{\text{tot},14} - T_{\text{ew},7}$	1.74( $\pm 0.25$ )/1.50	0.56( $\pm 0.03$ )	0.000	0.098	1.69( $\pm 0.40$ )/1.50	0.47( $\pm 0.04$ )	0.044	0.142	(2)
$f_z M_{\text{tot},14} - T_{\text{mw},7}$	1.63( $\pm 0.25$ )/1.50	0.54( $\pm 0.04$ )	0.000	0.087	1.69( $\pm 0.34$ )/1.50	0.45( $\pm 0.03$ )	0.000	0.125	(2)
$f_z M_{\text{gas},13} - T_{\text{ew},7}$	1.94( $\pm 0.21$ )/1.50	0.57( $\pm 0.02$ )	0.083	0.086	2.09( $\pm 0.23$ )/1.50	0.51( $\pm 0.02$ )	0.107	0.110	(2)
$f_z^{-1} L_{44} - f_z M_{\text{gas},13}$	1.55( $\pm 0.13$ )/1.33	0.30( $\pm 0.09$ )	0.083	0.085	1.64( $\pm 0.13$ )/1.33	0.19( $\pm 0.09$ )	0.131	0.132	(2)

**Table 3.5.** Best-fit parameters for the redshift evolution of the scaling relations. Again, the quantities are evaluated at  $R_{2500}$  and masses are estimated by using the RTM profile. For each relation we list the redshift evolution parameter  $B$ , the logarithmic slope  $A$  (compared to the theoretically expected value  $A^*$ ), the normalization  $\alpha$ , the minimum value of the function  $\chi^2$  and the number of degrees of freedom (d.o.f.). The results are given both for a subsample including the CC-only clusters (11 objects), and for the whole sample (24 objects). With the notation ( $y_{0,-4}$ ,  $y_\Omega$ ,  $Y_8$ ),  $L_{44}$ ,  $T_7$ ,  $M_{14}$ , we indicate the Compton parameter, the X-ray luminosity, the temperature and the mass, in units of ( $10^{-4}$ , mJy,  $10^8$  mJy Mpc $^2$ ),  $10^{44}$  erg s $^{-1}$ , 7 keV,  $10^{14}M_\odot$ , respectively.

relation ( $Y - X$ )	Cooling core clusters 11 objects				All clusters 24 objects			
	B	$A/A^*$	$\alpha$	$\chi^2_{\min}$ (d.o.f.)	B	$A/A^*$	$\alpha$	$\chi^2_{\min}$ (d.o.f.)
$f_z Y_8 - f_z^{-1} y_{0,-4}$	$2.36^{+0.64}_{-0.68}$	$1.02(\pm 0.09)/1.67$	$-1.24(\pm 0.04)$	15.9(8)	$0.76^{+0.28}_{-0.28}$	$1.15(\pm 0.08)/1.67$	$-1.00(\pm 0.03)$	87.8(21)
$y_\Omega - y_{0,-4}$	$-1.56^{+0.56}_{-0.60}$	$0.85(\pm 0.08)/1.00$	$0.80(\pm 0.04)$	5.1(8)	$-1.24^{+0.24}_{-0.24}$	$0.82(\pm 0.07)/1.00$	$0.83(\pm 0.03)$	88.6(21)
$f_z^{-1} y_{0,-4} - T_{\text{ew},7}$	$-2.12^{+0.96}_{-0.96}$	$2.41(\pm 0.25)/1.50$	$0.40(\pm 0.03)$	23.4(8)	$0.08^{+0.36}_{-0.32}$	$2.08(\pm 0.17)/1.50$	$0.12(\pm 0.02)$	82.4(21)
$f_z^{-1} y_{0,-4} - f_z M_{\text{tot},14}$	$-2.44^{+1.68}_{-2.52}$	$1.35(\pm 0.23)/1.00$	$-0.33(\pm 0.19)$	29.6(8)	$0.08^{+0.48}_{-0.48}$	$0.98(\pm 0.10)/1.00$	$-0.27(\pm 0.07)$	55.6(21)
$f_z^{-1} y_{0,-4} - f_z^{-1} L_{44}$	$0.04^{+0.48}_{-0.48}$	$0.69(\pm 0.05)/0.75$	$-0.57(\pm 0.07)$	48.0(8)	$-0.32^{+0.16}_{-0.16}$	$0.62(\pm 0.03)/0.75$	$-0.44(\pm 0.05)$	99.7(21)
$f_z Y_8 - T_{\text{ew},7}$	$-1.08^{+1.12}_{-1.16}$	$2.98(\pm 0.31)/2.50$	$-0.71(\pm 0.04)$	10.6(8)	$0.28^{+0.40}_{-0.40}$	$2.66(\pm 0.20)/2.50$	$-0.78(\pm 0.03)$	37.9(21)
$f_z Y_8 - f_z M_{\text{tot},14}$	$-2.32^{+1.96}_{-2.60}$	$1.68(\pm 0.25)/1.67$	$-1.55(\pm 0.20)$	20.5(8)	$0.28^{+0.52}_{-0.52}$	$1.14(\pm 0.13)/1.67$	$-1.26(\pm 0.08)$	78.9(21)
$f_z Y_8 - f_z^{-1} L_{44}$	$2.40^{+0.44}_{-0.48}$	$0.70(\pm 0.05)/1.25$	$-1.81(\pm 0.07)$	58.9(8)	$0.12^{+0.20}_{-0.16}$	$0.62(\pm 0.04)/0.75$	$-1.35(\pm 0.05)$	206.0(21)
$f_z^{-1} y_\Omega - T_{\text{ew},7}$	$-4.00^{+0.96}_{-0.96}$	$2.31(\pm 0.26)/1.50$	$1.20(\pm 0.03)$	16.6(8)	$-1.44^{+0.36}_{-0.32}$	$1.95(\pm 0.18)/1.50$	$0.97(\pm 0.02)$	71.2(21)
$f_z^{-1} y_\Omega - f_z M_{\text{tot},14}$	$-4.88^{+1.68}_{-2.44}$	$1.33(\pm 0.22)/1.00$	$0.52(\pm 0.18)$	26.9(8)	$-1.52^{+0.44}_{-0.40}$	$0.82(\pm 0.12)/1.00$	$0.64(\pm 0.08)$	120.0(21)
$f_z^{-1} y_\Omega - f_z^{-1} L_{44}$	$-1.52^{+0.48}_{-0.44}$	$0.58(\pm 0.05)/0.75$	$0.34(\pm 0.07)$	47.5(8)	$-1.72^{+0.16}_{-0.16}$	$0.40(\pm 0.03)/0.75$	$0.65(\pm 0.05)$	178.0(21)
$f_z^{-1} L_{44} - T_{\text{ew},7}$	$-0.72^{+0.96}_{-1.00}$	$3.27(\pm 0.29)/2.00$	$1.25(\pm 0.03)$	69.40(8)	$0.92^{+0.52}_{-0.52}$	$4.05(\pm 0.24)/2.00$	$0.85(\pm 0.03)$	190.0(21)
$f_z^{-1} L_{44} - f_z M_{\text{tot},14}$	$-1.32^{+1.24}_{-1.56}$	$1.29(\pm 0.16)/1.33$	$0.66(\pm 0.13)$	5.4(8)	$-0.24^{+0.56}_{-0.56}$	$1.36(\pm 0.11)/1.33$	$0.53(\pm 0.07)$	40.5(21)
$f_z M_{\text{tot},14} - T_{\text{ew},7}$	$0.56^{+1.12}_{-1.20}$	$1.79(\pm 0.30)/1.50$	$-1.00(\pm 0.28)$	11.1(8)	$-0.08^{+0.52}_{-0.52}$	$2.30(\pm 0.24)/1.50$	$-1.51(\pm 0.22)$	48.4(21)
$f_z M_{\text{tot},14} - T_{\text{mw},7}$	$-0.88^{+1.24}_{-1.32}$	$2.00(\pm 0.28)/1.50$	$-1.09(\pm 0.27)$	7.1(8)	$-0.32^{+0.48}_{-0.48}$	$2.32(\pm 0.22)/1.50$	$-1.54(\pm 0.21)$	33.0(21)
$f_z M_{\text{gas},13} - T_{\text{ew},7}$	$0.16^{+0.56}_{-0.60}$	$2.00(\pm 0.16)/1.50$	$0.57(\pm 0.02)$	39.2(8)	$0.84^{+0.28}_{-0.28}$	$2.17(\pm 0.12)/1.50$	$0.41(\pm 0.02)$	127.0(21)
$f_z^{-1} L_{44} - f_z M_{\text{gas},13}$	$-0.92^{+0.24}_{-0.24}$	$1.43(\pm 0.03)/1.33$	$0.45(\pm 0.03)$	73.7(8)	$-0.60^{+0.12}_{-0.12}$	$1.63(\pm 0.02)/1.33$	$0.26(\pm 0.02)$	358.0(21)

the CC-only subsample: this is done to allow a more direct comparison of our results with most of the works present in the literature, which are based on CC-sources only. Moreover this allows also to obtain at the same time more general relations which can be useful for future much extended (X-ray and SZ) cluster surveys, in which the distinction between relaxed and unrelaxed systems will be not easy.

### 3.4.1 The X-ray scaling relations

In this section we consider the scaling relations involving quantities extracted from the X-ray data only. We start by examining the relation between  $M_{\text{tot}}$  and  $T$ , and finding in general a good agreement between our best-fitting slopes and the values expected in the self-similar model. Then we will consider the other X-ray relations, finding slopes which are steeper than expected from the self-similar model. In particular the  $L - T$ ,  $L - M_{\text{gas}}$  and  $M_{\text{gas}} - T$  relations display deviations larger than  $2\sigma$ , while for the  $L - M_{\text{tot}}$  relation we found agreement between the observed slope and the expected one.

#### The $M_{\text{tot}} - T$ relation

Without any assumption for models on the gas density and (deprojected) temperature profile, we have supposed that the DM density profile is well described by an analytical model (RTM or NFW). Thanks to the results of numerical simulations, we know, indeed, sufficiently well the DM physics which is in fact very simple, only depending on the gravity, unlike the physics of the baryons, which is also affected by further sources of non-gravitational energy. Moreover we have removed the observational biases in the determination of the deprojected temperature (and consequently of the mass) by adopting the spectral-like temperature estimator (see Sect. 3.2.3). In this way we have a bias-free estimate of the deprojected temperature and, therefore, of the cluster mass. Below we focus our attention on  $T_{\text{mw}}$ , because it is directly related to the total energy of the particles and so comparable to the results of hydrodynamical simulations, unlike  $T_{\text{ew}}$ , which is affected by observational biases (see, e.g., Gardini et al., 2004; Mazzotta et al., 2004; Mathiesen & Evrard, 2001).

First, we notice that the two different models for the DM profile give slightly different results. Nevertheless, at an overdensity of  $\Delta = 2500$  the masses determined by using RTM are in perfect agreement with the ones determined by using NFW ( $\alpha_{\text{RTM}}^{\text{CC}} = 0.540 \pm 0.037$  and  $A_{\text{RTM}}^{\text{CC}} = 1.630 \pm 0.253$ ,  $\alpha_{\text{NFW}}^{\text{CC}} = 0.546 \pm 0.035$  and  $A_{\text{NFW}}^{\text{CC}} = 1.590 \pm 0.250$ ). At  $\Delta = 500$  the situation becomes less clear, because for most of the clusters we needed to extrapolate from  $R_{\text{spec}}$  (corresponding to  $\Delta \sim 1000$ ) up to  $\Delta = 500$ , being  $R_{\text{spec}}$  of order of  $(1/3)$ - $(1/2)$  of the virial radius (roughly corresponding to  $R_{2500} - R_{1000}$ ). Hereafter we consider only the RTM model, even if most of the results present in the literature are usually based on the NFW one.

Considering the whole sample, we find a normalization ( $\alpha = 0.45 \pm 0.03$ ), which is  $\sim 10$  ( $\sim 5$ ) per cent smaller than the value found by Allen et al. (2001) (Arnaud et al. (2005)), who only consider relaxed clusters. Our normalization ( $\alpha = 0.54 \pm 0.04$ ) is instead  $\sim 10$  ( $\sim 15$ ) per cent larger than the value of Allen et al. (Arnaud et al.) if

we only consider the CC-only subsample. This suggests a different behaviour depending on the presence or not of a cooling core (see also the left panel Fig. 3.3): in fact we find that at  $\Delta = 2500$  the normalization of the NCC subsample at  $M_{2500} = 5 \times 10^{14} M_{\odot}$  (corresponding to our median value for the mass) is  $\approx 10$  per cent smaller than for the CC-only subsample; conversely at  $\Delta = 500$  the two subsamples give consistent normalizations, but the robustness of this result is affected by the fact that in this case we have to extrapolate the mass profile out of the region covered by observational data.

Some other authors (e.g., Arnaud et al., 2005) prefer to mask out the central region (up to  $0.1 \times R_{200}$ ) in the determination of the mass profile. We have decided to check the effects of the inclusion of the cooling region in our analysis by comparing the values of the mass obtained by excluding or not the central 100 kpc in the determination of the best fit parameters of the RTM profile: we pointed out that accounting for the cooling region does not involve any systematic error on the determination of the mass, indeed we obtain more statistically robust results.

Consequently the disagreement between CC and NCC clusters is probably due to a different state of relaxation, namely that the former are more regular and with more uniform physical properties than the latter (De Grandi & Molendi, 2002); this is true even if we have masked out the most evident substructures. Notice that the observed mismatch is only marginally statistically significant ( $\sim 1 - 1.5\sigma$ ). For a couple of clusters, namely A520 and A2163, we find that the exclusion of the unrelaxed central regions avoids observational biases due to the presence of local substructures: in particular the mass of the first (second) object increases by a factor of  $\sim 2$  ( $\sim 1.5$ ) when excluding the central 300 (360) kpc. For other clusters which are evidently unrelaxed, we did not find any convenient way to avoid possible biases: even after masking out the most visible substructures, the analysis of the density and deprojected temperature profiles still reveals the possible presence of local irregularities (a sort of local ‘jumps’ in the profiles), which are difficult to individuate in the brightness image.

At  $\Delta = 2500$ , the best fitting normalization obtained considering the whole sample is  $\sim 30$  per cent below the value found in the non-radiative hydrodynamic simulations by Mathiesen & Evrard (2001)<sup>1</sup>; for the CC-only subsample, the normalization is  $\sim 20$  per cent below the theoretical value. The discrepancy is slightly reduced ( $\sim 15 - 20$  per cent) with respect to the adiabatic hydrodynamic simulations by Evrard et al. (1996).

The picture emerging from numerical simulations with a more sophisticated ICM modeling is different. The simulation by Borgani et al. (2004), which includes radiative processes, supernova feedback, galactic winds and star formation, suggests a normalization which is in rough agreement with our whole sample, and 15 per cent lower with respect to the CC-only subsample. Notice, however, that the re-analysis of the same simulation data made by Rasia et al. (2005), who adopted a different definition of temperature, the spectroscopic-like one (which is not consistent with our definition of mass-weighted temperature; see above for a more detailed discussion), gives a higher ( $\sim 40 - 50$  per cent) normalization.

Finally we notice that the slope of the  $M - T$  relation is, indeed, in agreement with the

---

<sup>1</sup>We have rescaled their results from  $\Delta = 500$  to  $\Delta = 2500$ .

theoretical expectations ( $A^* = 1.5$ ).

Considering the results at an overdensity of 500, we found a good agreement (at  $1\sigma$  level) between observed and theoretical slopes.

Our analysis suggests no evolution ( $B^{\text{CC}} = -0.88^{+1.24}_{-1.32}$ ,  $B^{\text{all}} = -0.32 \pm 0.48$ ), in agreement with the literature (see, e.g., Finoguenov et al., 2001; Ettori et al., 2004; Allen et al., 2001).

We compare also our intrinsic scatter, which is consistent with zero, with the one estimated by Rasia et al. (2005): they find a scatter of  $\approx 30(16)$  per cent by considering the emission-weighted (spectroscopic-like) temperature. We reach similar conclusions comparing our intrinsic scatter with the value retrieved by Motl et al. (2005).

### The $L - T$ relation

We find (see the upper-right panel of Fig. 3.3) a marginal agreement of our results on the slope of this relation ( $A^{\text{all}} = 3.37 \pm 0.39$ ), with those obtained by Ettori et al. (2002), who found  $A = 2.64 \pm 0.64$  at  $\Delta = 2500$ : however, their sample contains colder objects, for which a flatter relation would be expected. Our results also agree with the analysis made by Markevitch (1998):  $A = 2.64 \pm 0.27$ . Notice that his cluster sample is not directly comparable with ours, since it covers different ranges in redshift and temperature.

We compare our results about the scatter ( $\hat{S} = 0.220$  and  $S = 0.221$ ) with those obtained by Markevitch (1998), who found a smaller value:  $S = 0.103$  (see, however, the previous comments on the different characteristics of the two samples).

Moreover, we find (at  $\sim 1\sigma$ ) a positive (negative) redshift evolution for all clusters (CC-only subsample), i.e. we notice a mildly different behaviour on the evolution CC and NCC clusters. For comparison Ettori et al. (2002) found  $B = -1.04 \pm 0.32$  for their sample of clusters at higher redshift.

Regarding the normalization we observe a slightly different behaviour when the CC-only subsample and whole sample are considered:  $\alpha^{\text{CC}} = 1.18 \pm 0.05$  and  $\alpha^{\text{all}} = 1.03 \pm 0.05$ , respectively. We notice that the luminosity of the CC clusters is systematically larger than that of the NCC clusters, even if we have corrected it for the cooling flow (see Sect. 3.2.4), as already observed by Fabian (1994). On the contrary numerical simulations predict that the removal of the gas from the X-ray emitting phase reduces the luminosity (Muanwong et al., 2002). This confirms that cooling (Bryan, 2000; Voit & Bryan, 2001) is not effective in removing baryons from the X-ray phase, because of the presence of an extra-source of feedback or pre-heating (Balogh et al., 1999; Cavaliere et al., 1998; Tozzi & Norman, 2001; Babul et al., 2002), which maintains the ICM at warm temperature (Borgani et al., 2002). Alternatively, the more evident negative evolution of the CC clusters compared to the NCC ones (especially in the  $y_{\Omega}$ -X-ray(SZ) relations) could indicate different states of relaxation, being the former more regular, relaxed and virialized than the latter (De Grandi & Molendi, 2002).

### Other X-ray scaling relations

Here we discuss our results for the relations not shown in the figures. For the  $M_{\text{gas}} - T$  relation we find a  $\sim 1\sigma$  discrepancy between the slope of this relation in the CC-only subsample ( $A^{\text{CC}} = 1.94 \pm 0.21$  and  $A^{\text{all}} = 2.09 \pm 0.23$ ) and the theoretical expectation for the self-similar model ( $A = 1.5$ ). Nevertheless, our estimate is consistent with the results already present in the literature. By applying a  $\beta$ -model to recover the gas mass, Vikhlinin et al. (1998) measured  $A = 1.71 \pm 0.23$  at the baryon overdensity 1000 (approximately corresponding to the virial DM overdensity). Our slope is also in good agreement with the value ( $A = 1.98 \pm 0.18$ ) found by Mohr et al. (1999), always by applying the  $\beta$ -model. We have also a marginal agreement (at  $1\sigma$  level) with the value found by Ettori et al. (2004) ( $A = 2.37 \pm 0.24$ ), who make use of the  $\beta$ -model and apply the correction for  $E_z$ . Finally Ettori et al. (2002), combining a spectral analysis and the application of a  $\beta$ -model to the brightness distribution and without correcting for  $E_z$ , found  $A = 1.91 \pm 0.29$  for  $\Delta = 2500$  and  $A = 1.74 \pm 0.22$  at  $\Delta = 500$ . The results of this last paper also suggest a low intrinsic scatter, in good agreement with our analysis ( $\hat{S} = 0.079$ ). We point out here that we find some differences between CC and NCC clusters at  $\Delta = 2500$ , because of the contribution of the cooling core region ( $\lesssim 100$  kpc); at  $\Delta = 500$  this effect becomes negligible because the behaviour of the gas mass is dominated by the contribution from the external regions ( $M_{\text{gas}} \propto r$ ). Finally no significant evolution is observed ( $B = 0.16^{+0.56}_{-0.60}$ ) for the CC clusters; when we consider the whole sample, we notice a more significant positive evolution ( $B = 0.84 \pm 0.28$ ).

Regarding the  $L - M_{\text{tot}}$  the best-fit slope for the CC-only subsample ( $A^{\text{CC}} = 1.71 \pm 0.46$ ) is in good agreement with the results obtained by Reiprich & Böhringer (2002) ( $A = 1.80 \pm 0.08$ ), Ettori et al. (2002) ( $A = 1.84 \pm 0.23$ ) and Ettori et al. (2004) ( $A = 1.88 \pm 0.42$ ). The observed scatter we measure ( $S^{\text{CC}} = 0.206$ ,  $S^{\text{all}} = 0.270$ ) is slightly smaller than in previous analysis by Reiprich & Böhringer (2002) ( $S = 0.32$ ), and in agreement with Ettori et al. (2002) ( $S = 0.26$ ). This seems to suggest that the methods we applied to correct the observed luminosity (see Sect. 3.2.4) and to determine the total mass are quite robust. Hints of negative evolution are observed ( $B^{\text{CC}} = -1.32^{+1.24}_{-1.56}$ ,  $B^{\text{all}} = -0.24 \pm 0.56$ ).

For the  $L - M_{\text{gas}}$  law we measure a slope which is discrepant with respect to the theoretical value expected in the self-similar model. This relation, together with the one between  $M_{\text{gas}} - T$  and  $M_{\text{tot}} - T$ , has the lowest intrinsic scatter between the X-ray only scaling laws. Moreover we have a significant evidence of a negative redshift evolution.

### 3.4.2 The scaling relations involving the SZ effect

In this section, we discuss first the  $Y - y_0$  and  $y_\Omega - y_0$  relations, which are linking the SZ properties only (see Fig. 3.4), and then the relations between SZ and X-ray quantities (see Fig. 3.5). The importance of these relations relies on the possibility of providing new insights into the general physical properties of the ICM, in a way complementary to the X-ray view. In particular, the different dependence on the gas density and temperature of the SZ flux ( $\sim n_e T$ ) with respect to the X-ray brightness ( $\sim n_e^2 T^{1/2}$ ) can allow to reduce some of the biases present in the X-ray analysis. The presence of substructures

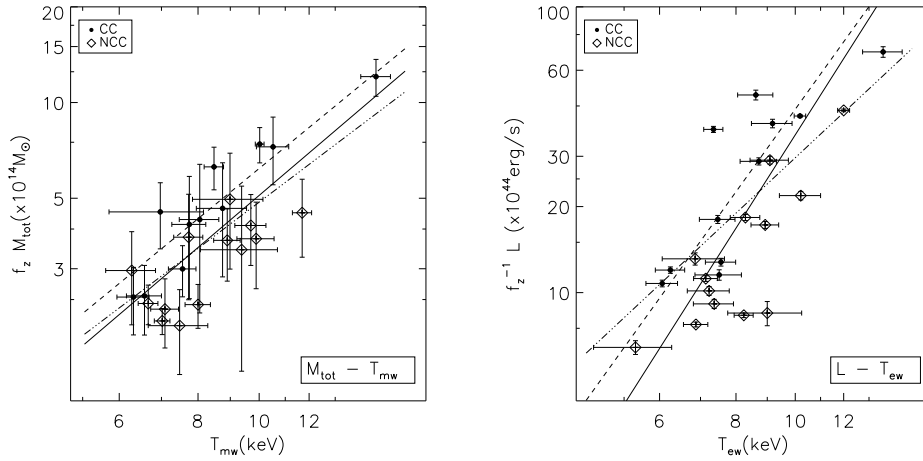


**Figure 3.3.** The relations between  $M_{\text{tot}}-T_{\text{mw}}$  (left panel) and  $L-T_{\text{ew}}$  (right panel). In each panel the filled circles represent cooling core (CC) sources, while the diamonds are the no-cooling core (NCC) ones. The solid line refers to the best-fit relation obtained when considering all clusters of our sample, the dashed one represents the best-fit when the CC sources only have been considered and the dot-dashed is the best-fit obtained by fixing the slope to the self-similar value.

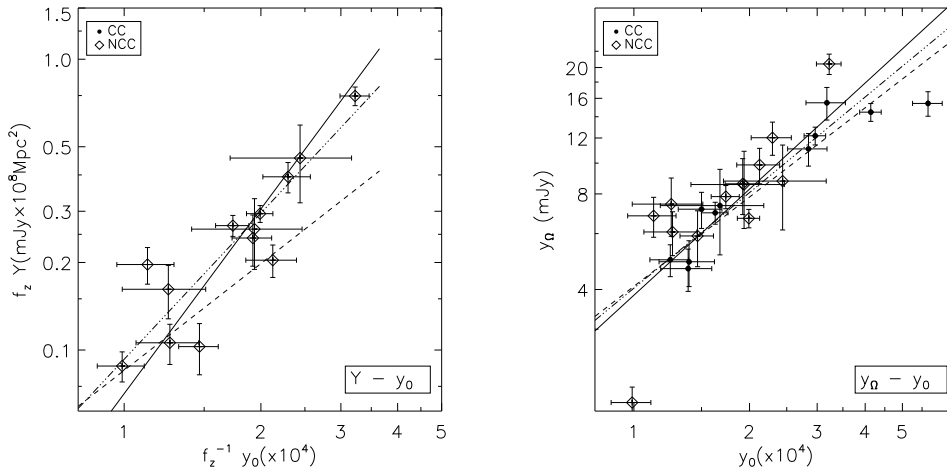


**Figure 3.4.** As in Fig. 3.3 but for the relations between  $Y-y_0$  (left panel) and  $y_{\Omega}-y_0$  (right panel).

and inhomogeneities in the ICM can indeed strongly affect some of the X-ray determined physical parameters, like temperature and luminosity. An independent approach through the SZ analysis of some physical quantities can shed more light on the limits of validity of the ICM self-similar scenario.

#### The $Y-y_0, y_{\Omega}-y_0$ relations

For both relations, we find slopes which are smaller than the expected ones. The discrepancy we measure is larger than the one found by McCarthy et al. (2003b). This

is likely due to the fact that the self-similar model predicts a pressure profile which is steeper than the observed one: including extra-gravitational energy draws a picture in which the gas density (and consequently the pressure) has a profile shallower than the DM density. This is also confirmed by the observation that there are differences between CC (which are obviously more subject to non-gravitational processes) and NCC clusters, having the former a slightly ( $\sim 1\sigma$ ) smaller integrated Compton parameter. We point out that the dispersion in these relations is very high, probably because of the systematics on the reconstruction of the integrated Compton parameter (see Sect. 3.2.5).

We measure a strong negative evolution in the  $y_\Omega - y_0$  relation. As pointed out by McCarthy et al. (2003b), this different behaviour of the  $y_\Omega - y_0$  relation (more in general of the  $y_\Omega$ -X-ray and  $y_\Omega$ -SZ relations) concerning the evolution is likely due to the fact the SZ effect within a fixed angular size samples larger physical region at higher redshifts. This means that the effect of non-gravitational processes are relatively more pronounced if the SZ flux is measured within smaller physical radii, where the density of the ICM is higher: this is expected in a scenario of either preheating, where we can assign a fixed extra-energy per particle, or cooling, where the radiative cooling is more prominent in the denser central regions. This is also in agreement with the general picture emerging by studying entropy profiles (see Ponman et al., 2003; Pratt et al., 2006; Voit & Ponman, 2003; Tozzi & Norman, 2001, and Chapter 4), which are affected just in the central regions by non-gravitational processes, while the self-similarity is roughly preserved in the halo outskirts, where the dynamics is still dominated by the gravity.

#### The $y_0 - T$ , $Y - T$ , $y_\Omega - T$ relations

We note that  $y_0 - T$  is the only scaling relation that deviates by  $\gtrsim 3\sigma$  from the self-similar slope (see Table 4 and 5) both when only CC clusters and CC+NCC objects are considered. Moreover, we measure an higher normalization in the CC-only subsample, probably due to the inclusion of the cooling regions during the SZ data reduction and the subsequent fit in the visibility plane. These results, in good agreement with the ones presented in Benson et al. (2004), are consistently obtained with both a robust BCES fit and a  $\chi^2$ -minimization. By applying the former technique, this relation is also the one that shows the smaller scatter (both total and intrinsic) around the best-fit. Furthermore, the  $\chi^2$ -approach indicates a significant negative evolution among the 11 CC clusters ( $B^{\text{CC}} = -2.12^{+0.96}_{-0.96}$  at  $2.5\sigma$ ;  $\chi^2_{\text{min}} = 23.4$  with 8 d.o.f.) that disappears when the whole sample of 24 objects is considered. For the NCC sources we do observe hints of positive evolution ( $B^{\text{NCC}} = 0.64^{+0.40}_{-0.40}$ ): this points to a different behaviour of the cool core and non-cool clusters in the central regions, and different state of relaxation of the gas as suggested by the comparison of the normalization of the fit ( $\alpha^{\text{CC}} = 0.19 \pm 0.15$  and  $\alpha^{\text{NCC}} = 0.14 \pm 0.35$ ).

The best-fitting parameters for the  $Y - T$  relation show a value for the slope in agreement with the value predicted by the self-similar model either when we consider the CC-only clusters or the whole sample, unlike for the  $y_0 - T$  relation: this is probably due to the sensitivity of  $y_0$  to the cooling region. On the contrary for the  $y_\Omega - T$  relation, when we consider the CC clusters, we observe a good agreement with the self-similar predictions

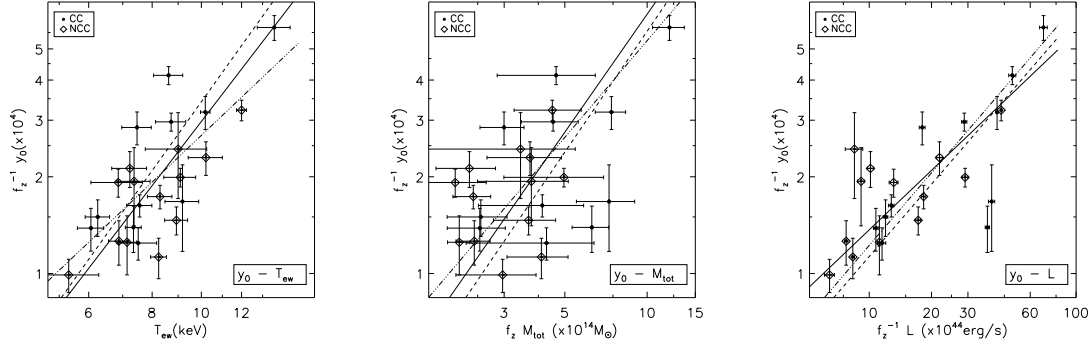


**Figure 3.5.** As in Fig. 3.3 but for the relations between  $y_0 - T_{\text{ew}}$  (left panel),  $y_0 - M_{\text{tot}}$  (central panel),  $y_0 - L$  (right panel).

( $A^{\text{CC}} = 1.98 \pm 0.46$   $A^* = 1.50$ ).

Our results confirm that the  $Y - T$  relation exhibits a smaller scatter than the  $y_0 - T$  one, as naively expected. Finally we find that the  $y_\Omega - T$  relation has a larger scatter than the  $Y - T$  one, in contrast with what obtained by McCarthy et al. (2003a). Moreover we notice in the CC-only subsample a mildly larger scatter compared to the whole cluster sample.

#### The $y_0 - M$ , $Y - M$ , $y_\Omega - M$ relations

These relations show a very good agreement between observed and self-similar slopes, with a scatter a factor of 2 larger than the correlation with  $T$  (see the previous subsection). We do not confirm the low scatter,  $S \approx 10 - 15$  per cent, for the  $Y - M$  relation suggested from the numerical simulations by Nagai (2006) and Motl et al. (2005): this indicate possible bias in the determination of  $Y$ . But it is possible that the present simulations are not completely adequate to reproduce the observed quantities, being the ICM modeling in hydrodynamical codes quite complex.

The normalization of the  $Y - M_{\text{tot}}$  relation has been investigated in dedicated hydrodynamical simulations to discriminate between different ICM physics. For example, Nagai (2006) uses non-radiative (NR) and with gas cooling and star formation (CSF) simulated clusters to find a normalization that varies by about 70 per cent: for a typical cluster with  $M_{2500} = 5 \times 10^{14} M_\odot$ ,  $Y^{\text{NR}} = (1.32^{+0.10}_{-0.09}) \times 10^{-4}$  and  $Y^{\text{CSF}} = (9.01^{+0.78}_{-0.59}) \times 10^{-5}$  at  $z = 0^2$ . At the same mass and overdensity, and fixing the slope to the self-similar model, our observed normalization is:  $Y^{\text{CC}} = (5.32 \pm 1.06) \times 10^{-5}$  and  $Y^{\text{all}} = (8.06 \pm 1.35) \times 10^{-5}$  for CC-only and all clusters, respectively. At  $\Delta = 200$ , the observed normalizations are  $Y^{\text{CC}} = (1.30 \pm 0.74) \times 10^{-5}$  and  $Y^{\text{all}} = (1.22 \pm 0.53) \times 10^{-5}$ , systematically lower than the results in Nagai (2006) ( $Y^{\text{NR}} = 5.13^{+0.57}_{-0.52} \times 10^{-5}$  and  $Y^{\text{CSF}} = 3.95^{+0.37}_{-0.34} \times 10^{-5}$ ) and more in agreement with the results by da Silva et al. (2004), that measure  $Y^{\text{NR}} = 1.85 \times 10^{-5}$ ,  $Y^{\text{cool}} = 1.73 \times 10^{-5}$  and  $Y^{\text{pre-heat}} = 2.50 \times 10^{-6}$  for non-radiative, cooling (cool) and pre-heating (pre-heat) simulations, respectively.

<sup>2</sup>Here we are following his definition of  $Y$ , corresponding to  $I_0 = 1$  in Eq. (3.8), and we adopt his cosmological parameters.

We obtain, therefore, that our CC clusters, for which we obtain the most robust estimates of the total mass at the overdensity of 2500 (see Subsect. 3.4.1), well reproduce the distribution measured in the  $Y - M_{\text{tot}}$  plane of the objects simulated including extra physical processes. Similar conclusions can be drawn for  $Y - T_{\text{mw}}$  and  $Y - L$  relations.

Finally, we find a negative evolution for the relations under examinations at  $\gtrsim 1\sigma$  confidence level for the CC-only clusters (see Table 5). The slopes of the correlations tend, however, to deviate from the self-similar predictions more significantly than the measurements obtained with the robust fitting technique. If we fix the slope to the self-similar value  $\mathcal{A}^*$  in these relations between SZ and X-ray quantities, we still obtain a negative evolution at  $\approx 1 - 2\sigma$  confidence level. We note here that Nagai (2006), on the contrary, does not find any hint of evolution in the  $Y - M$  relation.

#### The $y_0 - L$ , $Y - L$ , $y_\Omega - L$ relations

In general we find a good agreement between the best-fitted slope and the self-similar prediction. Compared to other scaling relations, in these cases the intrinsic scatter is very small ( $\sim 0.15$  for the  $y_0 - L$  relation estimated in the CC-only subsample). We do not observe significant differences between CC and NCC clusters, being the estimates of luminosity corrected for the cooling core.

Regarding the evolution, we find suggestions (at  $3\sigma$  level) for a negative evolution in the  $y_\Omega - L$  relation ( $B^{\text{CC}} = -1.52^{+0.48}_{-0.44}$ ). We observe instead positive evolution in the  $Y - L$  relation,  $B^{\text{CC}} = 2.40^{+0.44}_{-0.48}$ , but negative evolution when we consider the NCC clusters ( $B^{\text{NCC}} = -0.80^{+0.24}_{-0.20}$ ).

## 3.5 Conclusions

We have presented an analysis of X-ray and SZ scaling relations of a sample of 24 galaxy clusters in the redshift range 0.14-0.82, selected by having their SZ measurements available in literature. We have analyzed the Chandra exposures for these X-ray luminous objects. We have reconstructed their gas density, temperature and pressure profiles in a robust way. Then, we have investigated the scaling relations holding between X-ray and SZ quantities. By assuming an adiabatic self-similar model, we have corrected the observed quantities by the factor  $f_z \equiv E_z$ , neglecting the factor  $\Delta_z$ , checking that the final results do not change significantly in this way: so we can compare our results with the work in the literature. We have estimated the values of normalization, slope, observed and intrinsic scatters, and evolution to quantify the amplitude of the effects of the non-gravitational processes in the ICM physics. In this sense, the combined study of the SZ and X-ray scaling relations and their evolution in redshift is a powerful tool to investigate the thermodynamical history in galaxy clusters. Indeed, the departures from the self-similar predictions observed in some of the scaling laws studied in our work confirm that the simple adiabatic scenario is not wholly adequate to describe the physics of the X-ray luminous clusters, because it does not account for a further non-gravitational energy besides the potential one. We remind that our results are, by construction, more robust

at  $R_{2500}$ , where no extrapolation is required and the determinations of the mass (at least for CC clusters) and the reconstruction of the integrated Compton parameter are reliable. These results can be here summarized as follows.

- We observe a good agreement of the normalization of the  $M_{\text{tot}} - T$  relation between our results and the ones obtained in hydrodynamical numerical simulations. The other X-ray scaling relations involving a direct propagation of the absolute value of the measured gas density show a steeper slope than expected from self-similar predictions. Departures larger than  $2\sigma$  are observed in the  $L - T$  ( $A^{\text{all}} = 3.37 \pm 0.39$  vs.  $A^* = 2$ ),  $L - M_{\text{gas}}$  ( $A^{\text{all}} = 1.64 \pm 0.13$  vs.  $A^* = 1.33$ ) and  $M_{\text{gas}} - T$  ( $A^{\text{all}} = 2.09 \pm 0.23$  vs.  $A^* = 1.5$ ) relations. These results are consistent with previous analysis on high- $z$  X-ray luminous galaxy clusters (see, e.g., Ettori et al., 2002; Kotov & Vikhlinin, 2005; Maughan et al., 2006).
- Correlations between the investigated SZ quantities and the gas temperature have the largest deviations from the slope predicted from the self-similar model and the lowest scatter among similar relations with different X-ray quantities. The measured scatter is comparable to what is observed in the relations between X-ray parameters. The  $Y - T$  relation shows the lowest total and intrinsic scatter both when CC clusters only and the whole sample are considered.
- We observe a strong negative evolution in the  $y_{\Omega} - \text{X-ray}$  and  $y_{\Omega} - \text{SZ}$  relations. A plausible explanation is that the SZ effect within a fixed angular size samples larger physical region at higher redshifts. That means the effect of non-gravitational processes are relatively more pronounced within smaller physical radii.
- The observed normalization of the  $Y - M_{\text{tot}}$  relation in cooling-core clusters at  $\Delta = 2500$ , that provide the most robust estimates of the total masses in our cluster sample, agrees well with the predicted value from numerical simulations (see, e.g., da Silva et al., 2004; Nagai, 2006). In particular, we confirm the trend that lower normalization are expected when some feedback processes take place in the cluster cores: for a cluster with typical  $M_{2500} \approx 5 \times 10^{14} M_{\odot}$ , we measure  $Y^{\text{CC}} = (5.32 \pm 1.06) \times 10^{-5}$  in the sample of CC objects where the cooling activity is expected to be very effective, and  $Y^{\text{all}} = (8.06 \pm 1.35) \times 10^{-5}$  in the whole sample. However, we have to note that the normalization in hydrodynamical simulations is strictly related to the adopted recipes to describe physical processes, like gas cooling and star formation. These processes are also responsible for the production of the cold baryon fraction, the amount of which is still under debate when compared to the observational constraints (see, e.g., Borgani et al., 2006).
- The SZ - X-ray relations are, in general, well described by a self-similar model parametrized through the dependence upon  $f_z$ , when a robust fitting technique, that considers both the intrinsic scatter and the errors on the two variables, is adopted. On the contrary, when an evolution in the form  $(1+z)^B$  is investigated by a  $\chi^2$ -minimization with error propagations on both  $X$  and  $Y$  variables, we measure a strong negative evolution at  $\gtrsim 1\sigma$  level of confidence for all relations that involve SZ

quantities ( $y_0, Y, y_\Omega$ ) and the X-ray measured gas temperature and total mass. The slopes of the correlation tend, however, to deviate from the self-similar predictions more significantly than the measurements obtained with the robust fitting technique. If we fix the slope to the self-similar value  $\mathcal{A}^*$  in these relations between SZ and X-ray quantities, we obtain stronger hints of negative evolution for the  $y_0 - M_{\text{tot}}$  relation ( $B^{\text{CC}} = -0.88 \pm 0.94$ ) and for the  $Y - M_{\text{tot}}$  relation ( $B^{\text{CC}} = -2.30 \pm 1.13$ ).

Our results on the X-ray and SZ scaling relations show a tension between the quantities more related to the global energy of the system (e.g. gas temperature, gravitating mass) and the indicators of the ICM structure (e.g. gas density profile, central Compton parameter  $y_0$ ). Indeed, by using a robust fitting technique, the most significant deviations from the values of the slope predicted from the self-similar model are measured in the  $L - T$ ,  $L - M_{\text{tot}}$ ,  $M_{\text{gas}} - T$ ,  $y_0 - T$  relations. When the slope is fixed to the self-similar value, these relations show consistently a negative evolution suggesting a scenario in which the ICM at higher redshift has lower both X-ray luminosity and pressure in the central regions than the self-similar expectations. These effects are more evident in relaxed CC clusters in the redshift range 0.14-0.45, where a more defined core is present and the assumed hypotheses on the state of the ICM are more reliable.

A likely explanation is that we need an increase in the central entropy to spread the distribution of the gas on larger scales: this could be achieved either by episodes of non-gravitational heating due to supernovae and AGN (see, e.g., Evrard & Henry, 1991; Cavaliere et al., 1999; Tozzi & Norman, 2001; Bialek et al., 2001; Brighenti & Mathews, 2001; Babul et al., 2002; Borgani et al., 2002), or by selective removal of low-entropy gas through cooling (see, e.g., Pearce et al., 2001; Voit & Bryan, 2001; Wu & Xue, 2002), possibly regulated by some mechanism supplying energy feedback [e.g. the semi-analytical approach proposed by Voit et al. (2002) and the numerical simulations discussed by Muanwong et al. (2002); Tornatore et al. (2003); Kay et al. (2003)].



## Chapter 4

# Entropy profiles in X-ray luminous galaxy clusters at $z > 0.1$

The entropy distribution of the intracluster gas reflects both the accretion history of the gas and the processes of feedback which provide a further non-gravitational energy besides the potential one. In this Chapter, we study the profiles and the scaling properties of the gas entropy in 24 hot ( $kT_{\text{gas}} > 6$  keV) galaxy clusters observed with *Chandra* in the redshift range 0.14–0.82 and showing different states of relaxation. We show that the entropy profiles are remarkably similar outside the core and can be described by simple power laws with slope of 1.0 – 1.2. We measure an entropy level at  $0.1 R_{200}$  of  $100 - 500 \text{ keV cm}^2$  and a central plateau which spans a wide range of value ( $\sim$  a few  $-200 \text{ keV cm}^2$ ) depending on the state of relaxation of the source. To characterize the energetic of the central regions, we compare the radial behaviour of the temperature of the gas with the temperature of the dark matter  $T_{\text{DM}}$  by estimating the excess of energy  $\Delta E = 3/2k(T_{\text{gas}} - T_{\text{DM}})$ . We point out that  $\Delta E$  ranges from  $\approx 0$  in typical cooling-core clusters to few keV within 100 kpc in non-cooling core systems. We also measure a significant correlation between the total iron mass and the entropy outside the cooling region, whereas in the inner regions they anticorrelate strongly. We find that none of the current models in literature on the extra-gravitational energy is able to justify alone the evidences we obtained on the entropy, metallicity and gas+dark matter temperature profiles. This Chapter is mainly based on the refereed paper "*Entropy profiles in X-ray luminous galaxy clusters at  $z > 0.1$* ", Morandi A., Ettori S. 2007, MNRAS, 380, 1521-1532.

### 4.1 INTRODUCTION

The self-similar model (see, e.g., Kaiser , 1986, and Chapter 2) gives a simple picture of the process of cluster formation in which the ICM physics is driven by the infall of cosmic baryons into the gravitational potential of the cluster DM halo. The collapse and subsequent shocks heat the ICM up to the virial temperature. In this scenario all the non-radiative processes are neglected and the gravity, which has not preferred scales, is the only responsible for the physical properties of galaxy clusters: for this reason they are expected to maintain similar properties when rescaled with respect to their mass and formation epoch. X-ray properties of galaxy clusters show, however, some deviations from this scenario, breaking up the self-similarity predicted by the adiabatic model (see

recent work in Arnaud et al. (2005); Donahue et al. (2006); Ponman et al. (2003) and reference therein). In particular, in the last years, the studies about X-ray scaling relations (Ettori et al., 2004; Vikhlinin et al., 2005; Kotov & Vikhlinin, 2005; Maughan et al., 2006) and observations of the entropy profiles (Ponman et al., 1999, 2003) in groups and clusters of galaxies, and the analysis of simulated sources with an extra non-gravitational energy injection (Borgani, 2004) have suggested that we have to account for further non-gravitational feedback beyond the gravitational energy.

The gas entropy records the thermodynamic history of the ICM as the product of both gravitational and non-gravitational processes, shaping its observed structure accordingly (Voit, 2005a). The measurements of the gas entropy at  $0.1 R_{200}$  (hereafter  $S_{0.1}$ ) showed that the observed value of  $S$  is higher than the expected one from the adiabatic scenario (Ponman et al., 1999; Lloyd-Davies et al., 2000), where  $S$  should scale simply with the mean temperature of the virialized systems. Instead, an excess in the entropy, with respect to the prediction of the adiabatic model, is observed in the inner regions of groups and poor clusters at some fraction of  $R_{200}$ . This excess sets a minimum value of the entropy, labeled as entropy “floor” or “ramp”, associated to the ambient gas. The presence of this minimum level of entropy calls for some energetic mechanism, not referable to the gravity only, that falls into three main classes: preheating, where the gas collapsing into the dark matter potential well is preheated by some sources, before clusters were assembled at an early epoch (Kaiser, 1991; Balogh et al., 1999; Tozzi & Norman, 2001; Borgani et al., 2005); local heating by, e.g., AGN activity, star formation or supernovae (Bialek et al., 2001; Brighenti & Mathews, 2006; Babul et al., 2002; Borgani et al., 2002); cooling, which seems to be able to remove low-entropy gas in the centre of the clusters, producing a similar effect to non-gravitational heating (Bryan, 2000; Muanwong et al., 2002; Borgani, 2004).

In this Chapter we aim at comparing the models of preheating, feedback and cooling with the observed properties of the gas and of the dark matter in X-ray luminous galaxy clusters, by putting constraints on the sources of non-gravitational heating. To do that, we have considered the sample of 24 clusters presented in Chapter 3. To quantify the excess of energy stored in the ICM with respect to the amount available from the gravitational potential, we compare the gas and dark matter temperature profiles and measure the energy feedback as a function of the radial distance. Moreover, the clusters in our sample span a wide range of redshift ( $0.14 \leq z \leq 0.82$ ) and have different state of relaxation. We can thus investigate the dependence of the extra-gravitational energy feedback on the cosmic time of differently evolved structures.

This Chapter is constructed in this way: in Sect. 4.2 we describe the X-ray data reduction and analysis; in Sect. 4.3 we present our results about the entropy distribution in our hot ( $kT_{\text{gas}} > 6$  keV) clusters, studying its relation with the gas temperature and metallicity, its radial profile and how it relates to excess of energy measured by comparing gas and dark matter temperatures. We discuss our results in Sect. 4.4 and summarize our findings in Sect. 4.5.

**Table 4.1.** Properties of the sample analyzed. For each object, the name, the redshift  $z$ , the emission-weighted temperature  $T_{\text{ew}}$ , the ratio  $t_{\text{cool}}/t_{\text{age}}$ , a flag for the presence of a strong cooling core, an intermediate one or absence of a cooling core (labeled SCC, ICC and NCC, respectively) are indicated. The columns 6 and 7 refer to the best fit parameters  $S_{0.1}$  and  $\alpha$  for the Eq. (4.3) by setting  $S_0 = 0$ . The last four columns refer to the best fit parameters  $S_0$ ,  $S_{0.1}$ ,  $\alpha$  and the total  $\chi^2$  with the number of degree of freedom (d.o.f.) for the Eq. (4.3). For  $z$  and for each of the best fit parameters we report the average values and their dispersion at the bottom.

source	$z$	$T_{\text{ew}}$	$t_{\text{cool}}/t_{\text{age}}$	CC /NCC	power law		power law + $S_0$			$\chi^2$ d.o.f.
					$S_{0.1}$ keV cm <sup>2</sup>	$\alpha$	$S_0$ keV cm <sup>2</sup>	$S_{0.1}$ keV cm <sup>2</sup>	$\alpha$	
A2204	0.152	9.18 <sup>+0.75</sup> <sub>-0.65</sub>	0.03	SCC	602.6±10.0	1.05±0.04	5.8±0.8	602.4±20.7	1.44±0.03	35.9(31)
A2390	0.232	10.18 <sup>+0.23</sup> <sub>-0.21</sub>	0.06	SCC	524.8±4.7	1.30±0.02	3.8±1.3	597.6±5.0	1.15±0.01	377.6(55)
A1835	0.253	8.62 <sup>+0.60</sup> <sub>-0.54</sub>	0.09	SCC	288.4±2.7	1.16±0.02	11.9±2.5	273.0±10.9	1.35±0.06	10.2(30)
Zw3146	0.291	7.35 <sup>+0.27</sup> <sub>-0.26</sub>	0.02	SCC	457.1±9.2	1.20±0.06	4.8±0.4	401.1±7.5	1.39±0.02	55.3(57)
MS1358.4+6245	0.327	7.51 <sup>+0.70</sup> <sub>-0.61</sub>	0.05	SCC	489.8±3.1	1.05±0.02	0.0±0.0	511.8±24.2	1.19±0.04	9.9(31)
RXJ1347.5-1145	0.451	13.92 <sup>+1.14</sup> <sub>-0.93</sub>	0.08	SCC	616.6±13.2	1.07±0.04	15.7±1.2	548.3±14.8	1.44±0.03	22.3(44)
	0.284				409.9±152.6	1.18±0.11	6.0±5.9	509.0±130.7	1.23±0.16	
A1413	0.143	6.25 <sup>+0.36</sup> <sub>-0.33</sub>	0.22	ICC	263.0±2.3	0.95±0.01	34.8±21.2	230.9±27.8	1.06±0.15	0.8(16)
A1689	0.183	8.72 <sup>+0.63</sup> <sub>-0.56</sub>	0.18	ICC	316.2±3.7	1.02±0.02	36.4±20.4	286.9±27.1	1.09±0.13	1.8(23)
A2261	0.224	7.47 <sup>+0.53</sup> <sub>-0.47</sub>	0.27	ICC	263.0±1.5	1.09±0.01	55.1±13.1	205.3±18.4	1.29±0.13	0.8(22)
A611	0.288	6.06 <sup>+0.38</sup> <sub>-0.34</sub>	0.13	ICC	229.1±0.7	1.08±0.01	36.8±14.4	196.5±19.5	1.16±0.14	0.7(18)
A1995	0.319	7.56 <sup>+0.45</sup> <sub>-0.41</sub>	0.92	ICC	331.1±3.8	1.36±0.02	146.8±22.5	205.6±34.6	1.78±0.27	0.4(27)
MS1137.5+6625	0.784	5.48 <sup>+0.89</sup> <sub>-0.71</sub>	0.66	ICC	173.8±5.1	1.22±0.04	116.9±36.6	74.4±42.4	1.91±0.67	0.1(22)
	0.324				241.3±62.2	1.07±0.16	57.8±50.7	210.3±70.7	1.20±0.42	
A1914	0.171	8.93 <sup>+0.48</sup> <sub>-0.45</sub>	2.29	NCC	302.0±5.5	0.96±0.03	230.1±41.6	82.2±44.4	1.99±0.55	6.7(23)
A2218	0.176	6.88 <sup>+0.33</sup> <sub>-0.30</sub>	2.01	NCC	288.4±5.6	0.71±0.03	269.7±33.4	43.2±28.4	2.08±0.65	0.3(27)
A665	0.182	7.14 <sup>+0.33</sup> <sub>-0.31</sub>	1.47	NCC	275.4±1.3	1.16±0.01	184.1±19.8	108.0±20.9	1.94±0.21	9.0(30)
A520	0.199	8.24 <sup>+0.31</sup> <sub>-0.28</sub>	5.35	NCC	363.1±14.0	1.10±0.06	440.7±12.1	23.9±6.5	3.47±0.28	10.2(44)
A2163	0.203	12.00 <sup>+0.28</sup> <sub>-0.26</sub>	5.37	NCC	831.8±9.4	1.00±0.02	244.2±11.6	498.3±16.5	1.62±0.05	94.6(52)
A773	0.217	7.23 <sup>+0.62</sup> <sub>-0.52</sub>	1.19	NCC	281.8±0.8	0.85±0.01	176.7±56.1	114.4±57.6	1.48±0.48	0.7(41)
A697	0.282	10.21 <sup>+0.83</sup> <sub>-0.75</sub>	1.01	NCC	371.5±3.4	0.99±0.02	184.4±99.2	198.4±107.8	1.45±0.54	0.1(28)
A370	0.375	7.37 <sup>+0.58</sup> <sub>-0.53</sub>	6.63	NCC	398.1±3.4	0.38±0.01	396.4±76.5	25.4±65.4	2.06±2.54	0.7(20)
RXJ2228+2037	0.421	6.86 <sup>+0.89</sup> <sub>-0.71</sub>	2.05	NCC	234.4±2.0	0.89±0.01	158.9±111.4	91.2±110.0	1.56±1.10	0.5(23)
MS0015.9+1609	0.546	8.29 <sup>+0.49</sup> <sub>-0.43</sub>	1.13	NCC	245.5±8.3	1.02±0.05	173.7±37.5	91.2±39.2	1.76±0.47	0.3(14)
MS0451.6-0305	0.550	9.09 <sup>+0.70</sup> <sub>-0.61</sub>	0.97	NCC	229.1±4.8	1.01±0.04	177.5±56.2	70.7±65.2	1.95±1.01	0.1(14)
EMSS1054.5-0321	0.823	9.00 <sup>+1.39</sup> <sub>-1.10</sub>	2.82	NCC	398.1±2.1	1.00±0.02	347.2±107.5	69.2±133.2	3.01±3.54	0.1(19)
	0.345				292.6±174.3	0.95±0.21	300.7±110.3	86.8±132.5	1.69±0.71	

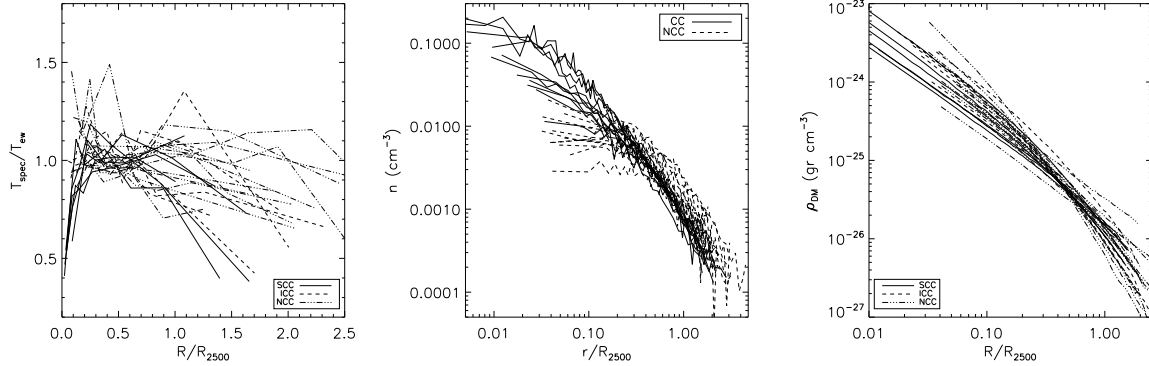


**Figure 4.1.** The radial profiles for the projected temperature  $T_{\text{spec}}(r)$ , normalized using the cooling-core corrected temperature  $T_{\text{ew}}$ , for the gas and dark matter density are shown for all objects of our sample in the left, central and right panels, respectively. The dashed lines refer to the intermediate cooling core clusters (ICC), the solid to the strong cooling clusters (SCC), and the dot-dashed to the non-cooling core clusters (NCC).

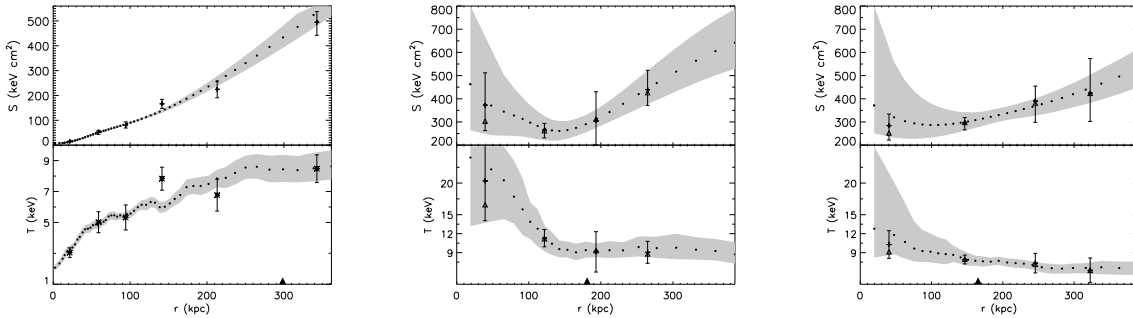


**Figure 4.2.** Comparison of the entropy and temperature profiles in the internal regions for, from the left to the right, ZW3146 (SCC), A1914 (NCC) and A2218 (NCC). The points represent each of the measure of  $S_j$  in the  $j$ -th spherical shell by applying the analysis described in Sect. 4.2, while the gray region refers to the  $1 - \sigma$  error band. The points with errorbars (triangles) are the measure of  $S$  by applying the spectral analysis (see Sect. 4.2.2) with (without) applying the spectroscopic-like temperature definition of (Mazzotta et al., 2004). The two triangles on the  $x$ -axis refer to the  $\delta = 0.1$  and  $\delta = 0.3$  (see Sect. 4.3).

## 4.2 The dataset and the analysis

In Chapter 3 we described our dataset and the analysis applied to study their  $X$ -ray and Sunyaev-Zel'dovich properties. Here we remind the main characteristics of the sample and of the  $X$ -ray analysis adopted to recover the radial distribution of the ICM entropy investigated in this Chapter.

We consider 24 galaxy clusters in the redshift range 0.14–0.82, emission-weighted temperature between 6 and 12 keV and  $X$ -ray bolometric luminosity  $L \gtrsim 10^{45}$  erg/s, with exposures available in Chandra archive. Assuming a spherically symmetric emission, the electron density and temperature profiles are obtained by deprojecting both the surface brightness profile put in hydrostatic equilibrium with a functional form of the

dark matter (DM) profile and the best-fit results obtained in the spatially-resolved X-ray spectral analysis by fitting a single thermal component. In particular, from the surface brightness profile resolved in a number of radial bins between 24 and 239, we obtain directly from the geometrical deprojection the electron density  $n_j$  in each  $j$ -th spherical shell. The deprojected gas temperature,  $T_j(\mathbf{q}, P_0)$ , is obtained by integration of the hydrostatic equilibrium equation once a functional form of the dark matter density profile,  $\rho = \rho(\mathbf{r}, \mathbf{q})$ , is assumed, where  $\mathbf{q} = (\text{scale radius, concentration parameter})$  and the gas pressure  $P_0$  at the X-ray boundary  $R_{\text{spec}}$  are free parameters. To parameterize the cluster mass distribution, we have considered two DM models: the universal density profile proposed by Navarro et al. (1997) (hereafter NFW) and the one suggested by Rasia et al. (2004) (hereafter RTM). In this study, we adopt the RTM model. Our results are not affected if a NFW functional form is used. To constrain the 3 free parameters  $(\mathbf{q}, P_0)$ , we define a grid of values and proceed with a  $\chi^2$  minimization of the merit function that compares the observed temperature profile with the projection of  $T_j(\mathbf{q}, P_0)$  by applying the spectroscopic-like temperature definition (Mazzotta et al., 2004). The best-fit values of  $(\mathbf{q}, P_0)$  are the ones corresponding to the minimum  $\chi^2$ ,  $\chi_{\text{min}}^2$ . The associated errors are estimated at the 68.3 per cent confidence level and are computed by looking to the regions in the parameter space where  $\Delta\chi^2 = \chi^2 - \chi_{\text{min}}^2$  is smaller than a given threshold, fixed according to the number of degrees of freedom (e.g.,  $\Delta\chi^2 = 1, 2.3, 3.53$  for 1, 2 and 3 d.o.f., respectively; see Chapter 3 and Press et al., 1992). The value of  $(\mathbf{q}, P_0)$  and the related errors are quoted in Chapter 3.

Furthermore, we deproject the best-fit results of the X-ray spectral analysis, spatially resolved in a lower number of bins (between 4 and 10) than the surface brightness profile as requested from the higher counts statistic needed to constrain adequately the measurements of the temperature. However, in each  $k$ -th shell, the electron density  $n_k$  and temperature  $T_k$  are then recovered without any assumption of the hydrostatic equilibrium and provide a direct verification of the validity of this assumption once they are compared to the measures of  $n_j$  and  $T_j$  described above. The spectral deprojection of the observed projected temperature  $T_{\text{proj}}$  has been performed in a set of  $n$  annuli selected to collect at least 2000 net counts by inverting the following equation:

$$T_{\text{proj}} = (\mathcal{V} \# (T_k n_k^2 T_k^{-\alpha})) / (\mathcal{V} \# (n_k^2 T_k^{-\alpha})), \quad (4.1)$$

where the operator  $\#$  indicates the matrix product (rows by columns),  $\mathcal{V}$  is the effective volume described in Appendix, and  $\alpha = 0.75$  using the spectroscopic-like temperature definition (Mazzotta et al., 2004).

### 4.2.1 Cooling core and Non-cooling core clusters

In the following analysis, we divide our sample in three categories, depending on the strength of the central cooling-core (see Table 4.1):

- **Strong cooling core (SCC)** clusters are the 6 objects in which the central cooling time is significantly less than the age of the universe at the cluster redshift ( $t_{\text{cool}}/t_{\text{age},z} < 0.1$ ). They show very low central temperature ( $\sim 2$  keV) and strong

spike of luminosity in the brightness profile, and a very pronounced drop of the temperature near the boundary of the observation, about a factor two compared with the peak of the temperature. The temperature profile is very regular, suggesting a relaxed dynamical state.

- **Intermediate cooling core (ICC)** clusters have a central cooling time with values  $0.1 \lesssim t_{\text{cool}}/t_{\text{age,z}} \lesssim 1$ . The six objects in our sample show a less prominent spike of brightness than SCC clusters and a mild drop of the temperature in the cooling region ( $\gtrsim 1/2 T_{\text{ew}}$ ).
- The **Non-cooling core (NCC)** sources (12 objects in our sample) have central cooling time higher than  $t_{\text{age,z}}$  and do not present any evidence of the central drop in the temperature profile. Both the temperature profile and surface brightness map are less regular than the ones observed in CC systems, showing hints of substructures and merging activity.

The gas and DM density profiles (right panel of Figure 4.1) have similar slopes over the entire radial range in the SCC clusters, whereas less self-similarity is present in the ICC and especially in the NCC clusters: the gas density profile is here flatter than the  $\rho_{\text{DM}}$  one, supporting the scenario in which the ICM has been affected by some form of non-gravitational energy. We discuss the physical interpretation of these observational results in Section 4.3.3.

The high level of relaxation of the SCC sources is also confirmed by the study of the polytropic index  $\gamma$ <sup>1</sup>, that has values near 1 with a very low scatter for the SCC sources, whereas is more scattered in NCC sources at  $r \gtrsim 0.5 R_{2500}$ :  $\gamma_{\text{SCC}} = 1.01 \pm 0.09$ ,  $\gamma_{\text{ICC}} = 1.06 \pm 0.12$ ,  $\gamma_{\text{NCC}} = 1.08 \pm 0.32$ . Within  $0.3 R_{200}$ , we measure  $\gamma_{\text{SCC}} = 0.66 \pm 0.07$ ,  $\gamma_{\text{ICC}} = 0.97 \pm 0.05$  and  $\gamma_{\text{NCC}} = 1.29 \pm 0.50$ , with a clear increase as a function of the morphological type and a very high scatter for the NCC sources.

## 4.2.2 On the gas entropy profile

Here we have extended the above analysis by estimating the entropy profile in each cluster by using (i) the gas pressure  $P_j$  and density  $n_j$  profile in the equation  $S_j = P_j/n_j^{5/3}$  and (ii) the deprojected spectral results  $S_k = T_k/n_k^{2/3}$ . The errors on the entropy profiles are obtained by error propagation of the uncertainties on the single quantity and/or best-fit parameters. We note that the dependence of  $S_j$  over  $P_0$ , the gas pressure value at the X-ray spectral boundary, can be checked by comparing it with the entropy measured once  $P_0$  is fixed to the value measured in the spectral analysis: we find a totally negligible variation at  $0.1 R_{200}$  and a change  $\lesssim 5$  per cent at  $0.3 R_{200}$ .

In Figure 4.2 we present a comparison of the entropy and temperature profiles recovered with the two methods in the inner regions of three representative cases, ZW3146 (SCC), A1914 (NCC) and A2218 (NCC). We obtain good agreement between the entropy

<sup>1</sup> $\gamma$  is calculated as  $\equiv d \log(T_k)/d \log(n_k) + 1$  by linear fit in the  $\log(n_k) - \log(T_k)$  plane by considering the spectral deprojected density  $n_k$  and temperature  $T_k$  described in Sect. 4.2.

measurements in ZW3146 and A1914, the former being an example of a typical CC source where the profile decreases moving inward, whereas the latter shows the most evident case of flattening, with hints of inversion, in the central entropy values. Given the good agreement between  $S_k$  and  $S_j$  even in the internal regions, we believe that this inversion is not due to our approach, but it is real in A1914 (similar behaviour is found in A773). We note that, if we use the entropy recovered by using the proper cooling function in Eq. (4.1) instead of the functional  $T^{-\alpha}$ , this inversion is less pronounced (see Fig. 4.2) for  $S_k$ .

In A2218 (NCC), we observe a marginal disagreement between  $S_j$  and  $S_k$ :  $S_j$  shows an inversion in the core, whereas  $S_k$  appears flatter. We draw similar conclusions for A370, A520, A2163, and RXJ2228+2037. Nevertheless we observe that for the latter sources the low spatial resolution of  $S_k$  in the central regions ( $\gtrsim 150 - 200$  kpc) does not allow to sample properly  $S_j$  on scales of  $\lesssim 50 - 150$  kpc, where the inversion occurs.

We note that the larger deviations between  $T_j$  and  $T_k$  are observed in NCC clusters within 100 kpc, where we expect higher relative contribution from non-thermal effects due to, e.g., merging activity. Therefore, even though the most prominent substructures identified in the cluster images were masked, implying that we have reduced their effects in the temperature reconstruction under the hydrostatic equilibrium equation, the sampled gas might be still subjected to ongoing merging processes. The higher value of  $S_j$  compared to  $S_k$  in the cluster centre is likely due to a very flat density profile that induces a higher temperature value (once the hydrostatic equilibrium equation is applied) than the spectral deprojected temperature. Indeed, unresolved mergers could lead to this very flat density profile (they are clearly visible in A520 and A2163), if the gas at  $R \lesssim 50 - 100$  kpc is not wholly relaxed and in hydrostatic equilibrium. For the other NCC sources, that do not show clearly ongoing merging processes, nevertheless we noted a disturbed morphology, as indicated, for example, from the fact that the centroid of symmetry does not coincide with the peak of brightness.

On larger scales, that involve larger cluster volumes, local deviations from the hydrostatic equilibrium are washed out even in the most unrelaxed objects, making tenable the hypothesis upon which  $S_j$  is obtained. This is also confirmed from (i) the agreement between  $S_j$  and  $S_k$  ( $T_j$  and  $T_k$ ) measured in these sources, (ii) the results of hydrodynamical numerical simulations (Rasia et al., 2006), and (iii) the analysis presented in Chapter 3 (Sect. 4.1.1), where we show how the relation between  $M_{\text{tot}}$  and the mass-weighted temperature for our sample is in agreement with the results coming from simulations including feedback and radiative processes, supporting our overall mass and temperature  $T_j$  reconstruction.

In the following analysis, we evaluate the entropy at  $0.1$  and  $0.3 R_{200}$ , i.e. at radii well beyond the region where the central inversion of  $S(r)$  is observed in few NCC objects. Given that, and the good agreement on larger scales between the reconstructed profiles, we define  $S(r) = S_j$  hereafter to fully exploit the spatial resolution available in estimating the entropy radial profile.

### 4.3 Entropy and temperature distribution

We examine the  $S - T$  relation at fixed overdensities, comparing our results with the ones available in literature for nearby systems. We investigate, then, the radial entropy profile, studying the behaviour of its gradient and its dependence upon the state of relaxation of the system. Finally, we implement an analysis of the temperature of the ICM and of the DM to quantify the excess of energy associated to the gas and its radial distribution.

#### 4.3.1 The entropy-temperature relation

We have determined the entropy-temperature relation at different fraction  $\delta$  of the virial radius  $R_{200}$  ( $\delta = 0.1$  and  $\delta = 0.3$ ). We have fitted a power-law model of the form:

$$E_z^{4/3} S_\delta = \alpha T_{\text{ew},7}^A, \quad (4.2)$$

where  $E_z = [\Omega_M(1+z)^3 + (1 - \Omega_M - \Omega_\Lambda)(1+z)^2 + \Omega_\Lambda]^{1/2}$  and  $T_{\text{ew},7}$  is the total cool-core corrected (by masking the central  $r = 100$  kpc region) emission-weighted temperature in units of 7 keV (see Chapter 3). The fit has been performed by adopting the BCES (Bivariate Correlated Errors and intrinsic Scatter)  $Y|X$  method (Akritas & Bershady, 1996) (see Chapter 3 for further details on this approach). We quote our best-fit results in Table 4.2 and show the distribution of the entropy values at different fractions of  $R_{200}$  in Figure 4.3. We note that SCC clusters show higher normalization ( $\sim 440$  and  $1400$  keV cm<sup>2</sup> at  $\delta = 0.1$  and  $0.3R_{200}$ , respectively) than ICC and NCC objects, with a larger deviation in the inner regions ( $\delta = 0.1$ ) which can be explained invoking different relaxation states of the clusters as discussed in Sect. 4.3.4. The best-fit slopes, within the error-bar at  $1\sigma$ , are in agreement with the self-similar prediction ( $A = 1$ ) and steeper than the slopes of  $A \sim 0.5 - 0.6$  observed in local samples of galaxy groups and clusters (Piffaretti et al., 2005; Pratt et al., 2006; Ponman et al., 1999, 2003). For comparison, we present in Table 4.2 also the normalizations measured by fixing  $A = 1$  (self-similar expectation) and  $A \sim 0.65$  (Ponman et al., 2003) and plot in Figure 4.3 the best-fit results obtained by Pratt et al. (2006) and Piffaretti et al. (2005) from their analysis of relaxed groups and clusters at low redshift. Pratt et al. (2006) measure  $A = 0.49 \pm 0.15$  ( $\alpha = 271 \pm 20$ ) and  $A = 0.64 \pm 0.11$  ( $\alpha = 990 \pm 55$ ) for  $\delta = 0.1$  and  $\delta = 0.3$ , respectively, with a clear departure from the self-similar expectation ( $A = 1$ ). Piffaretti et al. (2005) at  $\delta = 0.1$  measure  $\alpha = 255 \pm 71$  by fixing  $A = 0.65$ . Once these results are compared with what we measure in our sample of very massive systems, we observe that our normalizations are on average higher by 20-60 per cent, with slopes that are steeper and closer to the self-similar prediction than the values measured locally (see also Ponman et al., 2003). This result is in agreement with the fact that we are measuring the entropy distribution in massive clusters with cool-core corrected temperatures in the range 6 – 12 keV. These systems are definitely less affected from extra-gravitational, feedback processes that, on the contrary, are so relevant in groups and low-mass clusters representing the bulk in the sample of objects studied in, e.g., Piffaretti et al. (2005) and Ponman et al. (2003). Moreover, by parameterizing the evolution in redshift using

**Table 4.2.** Best fit parameters of the  $S - T$  relation by applying the Eq. (4.2). The sources are grouped into SCC, SCC+ICC and all clusters.

CC /NCC	$\delta = 0.1$		$\delta = 0.3$	
	A	$\alpha$ keV cm <sup>2</sup>	A	$\alpha$ keV cm <sup>2</sup>
SCC	$0.76 \pm 0.24$	$468 \pm 70$	$0.91 \pm 0.19$	$1380 \pm 154$
	1 (fixed)	$440 \pm 10$	1 (fixed)	$1409 \pm 146$
	0.65 (fixed)	$494 \pm 20$	0.65 (fixed)	$1567 \pm 155$
SCC+ICC	$1.18 \pm 0.16$	$380 \pm 28$	$1.17 \pm 0.22$	$1202 \pm 94$
	1 (fixed)	$399 \pm 14$	1 (fixed)	$1186 \pm 85$
	0.65 (fixed)	$432 \pm 15$	0.65 (fixed)	$1242 \pm 89$
all	$1.33 \pm 0.20$	$354 \pm 20$	$1.41 \pm 0.26$	$1023 \pm 77$
	1 (fixed)	$415 \pm 11$	1 (fixed)	$1140 \pm 50$
	0.65 (fixed)	$460 \pm 14$	0.65 (fixed)	$1216 \pm 59$

a  $(1+z)^B$  dependence (see Chapter 3 for further details on this approach), we did not observe any hints of evolution of the entropy-temperature relation within our sample. A very significant positive evolution ( $B \approx 2 \pm 0.1$  but with a reduced  $\chi^2$  of 5; see Fig. 4.3) is instead measured in the relation between the entropy estimated at  $0.1R_{200}$  and  $T_{\text{ew}}$  when our CC (SCC+ICC) objects are compared to the best-fit local results in Pratt et al. (2006). Although the local best-fits refer to objects distributed over a wider range in temperature, the systematic larger values measured at higher redshift is noticeable and definitely more evident at  $0.1R_{200}$  than at  $0.3R_{200}$  where we measure  $B \approx 1 \pm 0.2$  with a reduced  $\chi^2$  of about 1.

### 4.3.2 Properties of the entropy profiles

To characterize the gas entropy profile, we follow Donahue et al. (2006) and fit two different models. The first one reproduces the radial entropy profile with a power law plus a constant  $S_0$ :

$$S(r) = S_0 + S_{0.1} \left( \frac{r}{0.1 r_{200}} \right)^\alpha \quad (4.3)$$

In the second functional form, we set  $S_0 = 0$ , modeling the entropy profile with a pure power law. The best fit parameters on the radial profile are determined by applying the  $\chi^2$  statistic to the Eq. (4.3) over the radial entropy profile between  $0.1R_{200}$  and  $0.3R_{200}$ , whereas BCES(Y|X) is used when  $S_0$  is fixed to zero and the region within  $0.1R_{200}$  is excluded from the fit because it is strongly affected by the cooling process. The outermost bins of the fit are excluded by the fit, being noisy and likely affected by systematic errors due to subtraction of the noise in the data reduction (see Chapter 3). Our best-fit results are quoted in Table 4.1.

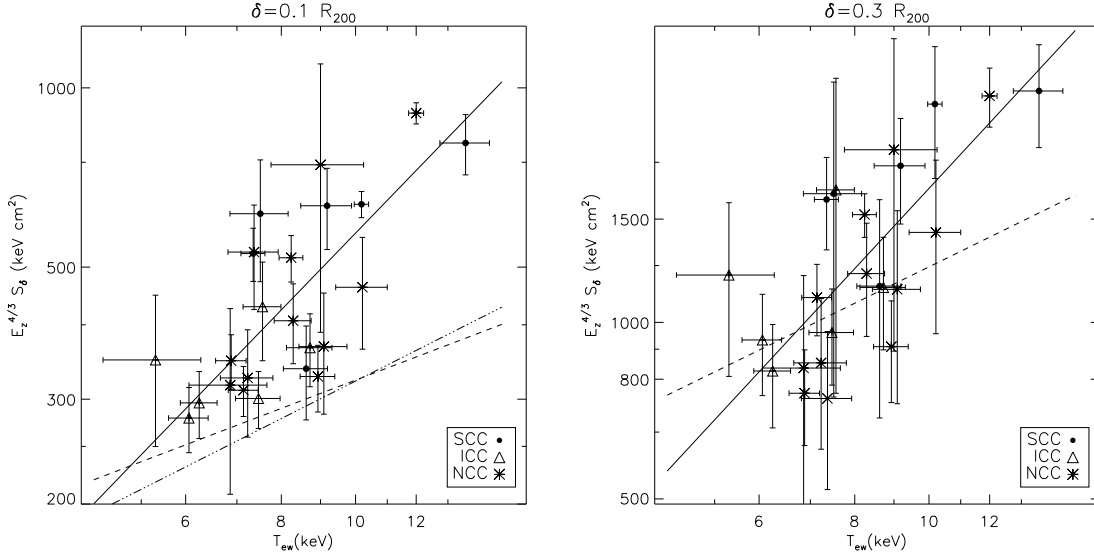


**Figure 4.3.** The  $S-T$  relation at different fraction  $\delta$  of  $R_{200}$ :  $\delta = 0.1 R_{200}$  (left panel) and  $\delta = 0.3 R_{200}$  (right panel). In each panel the filled circles represent the strong cooling core sources (SCC), the triangles the intermediate cooling core clusters (ICC), while the stars the non-cooling core clusters (NCC). The solid line refers to the best-fit relation obtained when considering all the clusters of our sample, while the dashed one represents the best-fit obtained by Pratt et al. (2006) and the dot-dashed by Piffaretti et al. (2005).

The entropy profiles show a regular behaviour (see Fig. 4.3.2), once the quantities are rescaled to the characteristic value  $K_{2500}$  at the overdensity of  $2500^2$  for adiabatic clusters (see, e.g., Eq. 2 in Voit et al., 2005b). Profiles of CC clusters are similar down to the inner resolved regions, whereas NCC systems show large deviations in the central parts. These profiles are well reproduced by the functional form with a power law plus a constant for which we obtain a  $\chi_{\text{red}}^2$  always less than or of the order of unity, apart from A2390. In particular, SCC sources show a very tight range of values of the entropy pedestal  $S_0$  ( $S_0 \lesssim 15 \text{ keV cm}^2$ ) in agreement with the value found by Donahue et al., and a power-law behaviour which is roughly preserved on the entire range of the radial entropy profile, even in the cooling region (see right panel of Figure 4.3.2). The average slope determined from the second method ( $\alpha = 1.18 \pm 0.11$ ) is very similar to the theoretical value of 1.1 predicted by Tozzi & Norman (2001) by using analytic models of shock dominated spherical collapse. Concerning  $S_{0.1}$ , it shows values in the range  $270 - 600 \text{ keV cm}^2$ : if we adopt the definition of  $S_{100}$  in Donahue et al. as the normalization at 100 kpc, we have  $S_{100} \sim 90 - 150 \text{ keV cm}^2$ , mildly lower than than the range found by them ( $S_{100} \sim 90 - 240 \text{ keV cm}^2$ ).

The ICC clusters show higher and wider range of  $S_0$ , with a typical value of  $\sim 30 \text{ keV cm}^2$ . The power-law behaviour is preserved just on large scale, i.e. outside the cooling region. The average slope is still in agreement with above theoretical predictions ( $\alpha = 1.07 \pm 0.16$ ), but it is a little lower than the value measured in SCC clusters.

In NCC objects, we observe a more scattered radial profile, which is likely self-similar

<sup>2</sup> $R_{2500}$  is  $\sim 0.25 R_{200}$ , i.e.  $\approx 400 - 600$  kpc.

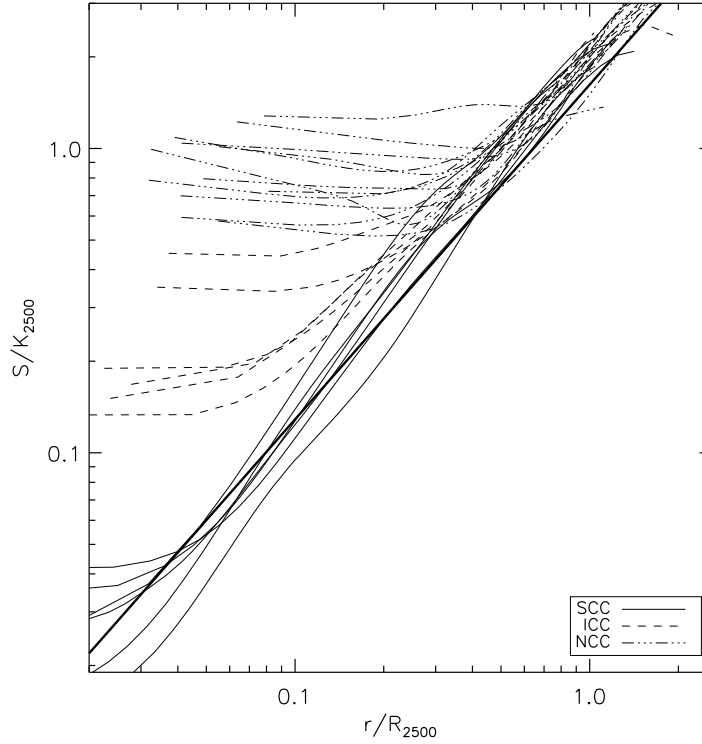


**Figure 4.4.** Profiles of  $S/K_{2500}$  as a function of  $r/R_{2500}$ . The dashed line represents the intermediate cooling core clusters (ICC), the solid the strong cooling clusters (SCC), and the dot-dashed the non-cooling core clusters (NCC). The thick solid line represents the profile of Voit et al. (2005b),  $S/K_{2500} = 1.62(r/r_{2500})^{1.1}$  (see their Fig. 1, where we have renormalized their entropy profile from  $\Delta = 200$  to  $\Delta = 2500$ ).

beyond the central regions ( $\sim 0.5 R_{2500} \approx 200 - 300$  kpc). In the inner regions, we notice a very high dispersion on the entropy pedestal value ( $\sim 80 - 400 \text{ keV cm}^2$ ), larger than the values found in the CC clusters. The average slope is mildly lower than the one determined in the CC-only subsample ( $\alpha \sim 0.95 \pm 0.21$ ).

We point out that  $\alpha$  rises by considering NCC, ICC and SCC sources, respectively ( $\alpha^{\text{SCC}} = 1.18 \pm 0.11$ ,  $\alpha^{\text{ICC}} = 1.07 \pm 0.16$  and  $\alpha^{\text{NCC}} = 0.95 \pm 0.21$  for the power-law model). As we will see in Sect. 4.3.3, this trend is probably due to the effect of non-gravitational sources on large scale, which justify the flatter radial behaviour of the entropy profile in NCC clusters.

It is worth noticing the behaviour of the entropy pedestal  $S_{0.1}$  in the different subsamples:  $S_{0.1}^{\text{NCC}} = 300.7 \pm 110.3 \text{ keV cm}^2$ ;  $S_{0.1}^{\text{ICC}} = 57.8 \pm 50.7 \text{ keV cm}^2$ ;  $S_{0.1}^{\text{SCC}} = 6.0 \pm 5.9 \text{ keV cm}^2$ . The trend of the gas density and temperature profile (see central and left panel of Figure 4.1) can justify the progressively greater value of the entropy in the inner regions by considering SCC, ICC and NCC clusters, respectively. We observe higher normalization of the entropy in SCC sources (see Figure 4.3.2 and the value of the parameter  $A$  in Table 4.1). This behaviour is due to the fact that the SCC sources show steeper density profiles, i.e. at the same fraction of  $R_{200}$ , as long as we consider radii greater than  $0.1 R_{200}$ ,

the density of the SCC sources is lower. Even though the temperature profiles in the SCC sources are a bit steeper than in the ICC and NCC objects, the overall effect is that the gas entropy tends to be higher in SCC clusters. We note that the unrelaxed morphology of the NCC sources cannot account for systematic changes in, e.g., the determination of  $R_\Delta$ .

On the evolution with redshift of the best-fit parameters of Eq. (4.3), we note that only for  $S_{0.1}^{\text{ICC}}$  we obtain a marginal evidence of negative evolution (Spearman's rank coefficient  $r_s = -0.60$  for 22 d.o.f. with probability of null correlation  $p = 0.28$ ). On the contrary,  $\alpha$  shows a positive evolution for the ICC clusters:  $r_s^{\text{ICC}} = 0.90$ , with  $p = 0.37$ , while for the SCC and NCC sources there is not apparent evolution.

We have calculated the weighted average value of the slopes of the best-fit parameters of the local sample of clusters determined by Donahue et al. (2006), so as to compare it with our estimate at higher redshift: they measure  $\alpha = 1.00 \pm 0.01$  (when  $S_0 = 0$ ) and  $\alpha = 1.23 \pm 0.01$  (by accounting for  $S_0$ ), while we obtain  $\alpha = 1.10 \pm 0.01$  and  $\alpha = 1.27 \pm 0.01$ , respectively, by applying their procedure<sup>3</sup>. These results, confirmed also including in the sample the ICC sources, suggest that entropy profiles in nearby CC systems are slightly flatter than in CC clusters at higher redshift, providing some marginal hints on the evolutionary trends present in the entropy distribution.

In Figure 4.3.2, we plot the break radius  $r_{\text{break}}$  present in the entropy profile  $S(r)$ , i.e. the radius where  $S_0 = S_{0.1} (r_{\text{break}} / (0.1 r_{200}))^\alpha$  in Eq. (4.3), as a function of the redshift. We found the following average values for  $r_{\text{break}}/r_{200}$ :  $r_{\text{break}}^{\text{SCC}}/r_{200} = 0.005 \pm 0.004$ ,

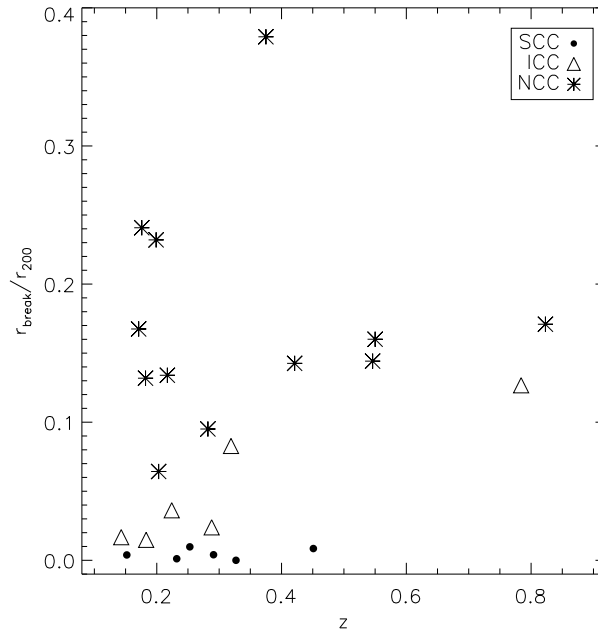


**Figure 4.5.** Normalized break radius  $r_{\text{break}}/r_{200}$  as a function of the redshift.

$r_{\text{break}}^{\text{ICC}}/r_{200} = 0.050 \pm 0.045$  and  $r_{\text{break}}^{\text{NCC}}/r_{200} = 0.172 \pm 0.082$ . The NCC sources show value

<sup>3</sup>The errors refer to the average value.

of  $r_{\text{break}}/r_{200}$  definitely higher than the CC clusters, defining the scale where the non-gravitational energy breaks the self-similarity ( $r_{\text{break}}^{\text{NCC}} \sim 0.1 - 0.4r_{200} \sim 200 - 600$  kpc). We do not observe significant evolution for  $r_{\text{break}}$ , except for the CC objects (Spearman's rank coefficient of  $r_s = 0.89$ , probability of null correlation  $p = 0.019$ ).

### 4.3.3 Gas and dark matter temperature profiles

In this section, we define a temperature associated to the dark matter component following the method presented in Ikebe et al. (2004); Hansen & Piffaretti (2007). We define the temperature of the dark matter halo,  $T_{\text{DM}}$ , as:

$$kT_{\text{DM}} \equiv \frac{1}{3} (\sigma_r^2 + 2\sigma_\theta^2) \mu m_p \quad (4.4)$$

where  $\mu$  is the mean molecular weight of the ICM,  $m_p$  is the proton mass,  $\sigma_\theta$  and  $\sigma_r$  are the 1-dimensional tangential and radial velocity dispersions of the dark matter. The radial velocity dispersions has been obtained by solving the Jeans equation:

$$\frac{GM(\mathbf{q})}{R} = -\sigma_r^2 \left( \frac{d \ln \rho_{\text{DM}}(\mathbf{q})}{d \ln R} + \frac{d \ln \sigma_r^2}{d \ln R} + 2\beta(\mathbf{q}) \right), \quad (4.5)$$

where a velocity anisotropy parameter is defined,  $\beta(\mathbf{q}) = 1 - \sigma_\theta^2/\sigma_r^2$ . N-body simulations for a variety of cosmologies shows that  $\beta$  has roughly an universal radial profile (Cole & Lacey, 1996), which is given by the following relation:

$$\beta(\mathbf{q}) = \beta_m \frac{4r_n}{r_n^2 + 4} \quad (4.6)$$

where  $r_n = r/r_{200}(\mathbf{q})$ , and  $\beta_m \approx 0.3 - 0.5$  (Carlberg et al., 1997). The dark matter profile is estimated as  $\rho_{\text{DM}} = \rho_{\text{tot}} - \mu m_p n_{\text{gas}}$ , where  $\rho_{\text{tot}}$  and  $n_{\text{gas}}$  has been determined from the analysis in Chapter 3. We will compare the dark matter temperature to the gas temperature,  $T_{\text{gas}}$ , recovered by applying the hydrostatic equilibrium equation <sup>4</sup>.

We solve Eq. (4.5) for  $\beta_m = \{0, 0.4\}$ , corresponding to the case of isotropy of the DM and to the central value of the above-mentioned range, respectively, to recover  $\sigma_r^2$  and therefore  $T_{\text{DM}}$ . As boundary condition in Eq. (4.5), we assume  $T_{\text{DM}}$  equal to  $T_{\text{gas}}$  at  $R_{\text{spec}}$ . We have checked that uncertainties on the DM temperature assumption at  $R_{\text{spec}}$  are almost negligible on the DM temperature profile in the inner and central regions ( $R \lesssim R_{2500} \sim 0.25R_{200}$ ), being  $R_{\text{spec}} \sim 0.3 - 0.5R_{200}$ , making our results up to  $R_{2500}$  reliable and not affected from the assumed value at the boundary. The errors are estimated by looking to the regions of the parameter space that satisfy the condition  $\chi^2 - \chi_{\text{min}}^2 < 2.3$  after the analysis described in Chapter 3. Examples of the gas and DM temperature profiles for SCC, ICC and NCC objects are shown in Fig. 4.6.

Because only the baryonic component is expected to be prone to non-gravitational energy effects in galaxy clusters, the difference between  $T_{\text{gas}}$  and  $T_{\text{DM}}$ ,  $\Delta kT$ , is a powerful tool to trace the thermal history of the ICM. We show in Fig. 4.6 how  $\Delta kT$  varies as a

<sup>4</sup>Following the notation in Sect. 4.2,  $n_{\text{gas}} = n_j$  and  $T_{\text{gas}} = T_j$ .

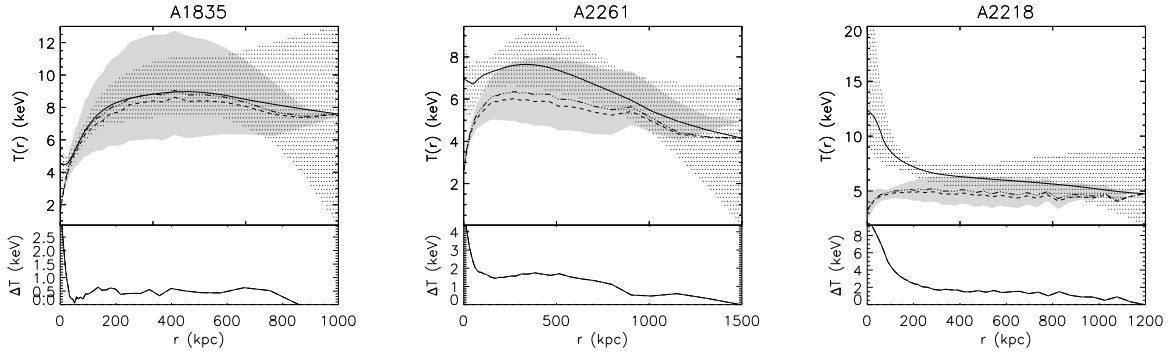


**Figure 4.6.** Temperature profiles of the gas (solid line) and of the dark matter (dashed and dot-dashed line for  $\beta_m = 0$  and  $\beta_m = 0.4$ , respectively). The error bands are represented by the gray shaded region for the gas, and hatched region for the DM for the case where  $\beta_m = 0$ . The clusters are A1835 (SCC), A2261 (ICC), and A2218 (NCC), from the left to the right.

function of the radius. The NCC clusters show a clear trend of  $\Delta kT$ , with values always greater than zero:  $\Delta kT \approx 1 - 2 \text{ keV}$  outside the central region ( $\gtrsim 200 - 400 \text{ kpc}$ ) and it is a few keV in the inner region. Near the cluster observed boundary, DM anisotropies might make  $T_{\text{DM}}$  roughly in agreement with  $T_{\text{gas}}$ , even though large statistical errors are present and our boundary condition holds. A similar trend is observed in ICC clusters, where a less significant disagreement between  $T_{\text{gas}}$  and  $T_{\text{DM}}$  is however observed. In SCC clusters, on the contrary,  $T_{\text{gas}}$  is well in agreement with  $T_{\text{DM}}$ , especially in the inner and central regions.

We notice here that the strong negative evolution measured in the scaling relations between  $y_\Omega$  and the X-ray/SZ quantities presented in Chapter 3, where  $y_\Omega$  is the integrated Compton parameter over a fixed angular distance, supports the observed radial behaviour of  $\Delta kT$ . Indeed, the measured SZ effect within a fixed angular size samples larger physical regions at higher redshifts. This demonstrates that the effect of non-gravitational processes is relatively more pronounced if the SZ flux is measured within smaller physical radii, indicating the physical scale over which the non-gravitational processes are more relevant. When we perform, instead, the same analysis integrating the Compton parameter within a physical radius (as done with the quantity  $y_\Delta$ ), we observe definitely lower negative evolution.

We have also estimated the global excess of energy  $\Delta U_{2500}$  defined in this way:

$$\Delta U_{2500} = \int_0^{R_{2500}} \frac{3}{2} \Delta kT(r) n_{\text{gas}}(r) 4\pi r^2 dr \quad (4.7)$$

We find that  $\Delta U_{2500} \gtrsim 10^{62} \text{ erg}$  in NCC sources (corresponding to about 15-20 per cent of the total thermal energy), that is a factor between 4 and 10 higher than the measured excess in SCC clusters.

We refer to Sect. 4.4 for a discussion of the observational evidence presented in these two last sections.

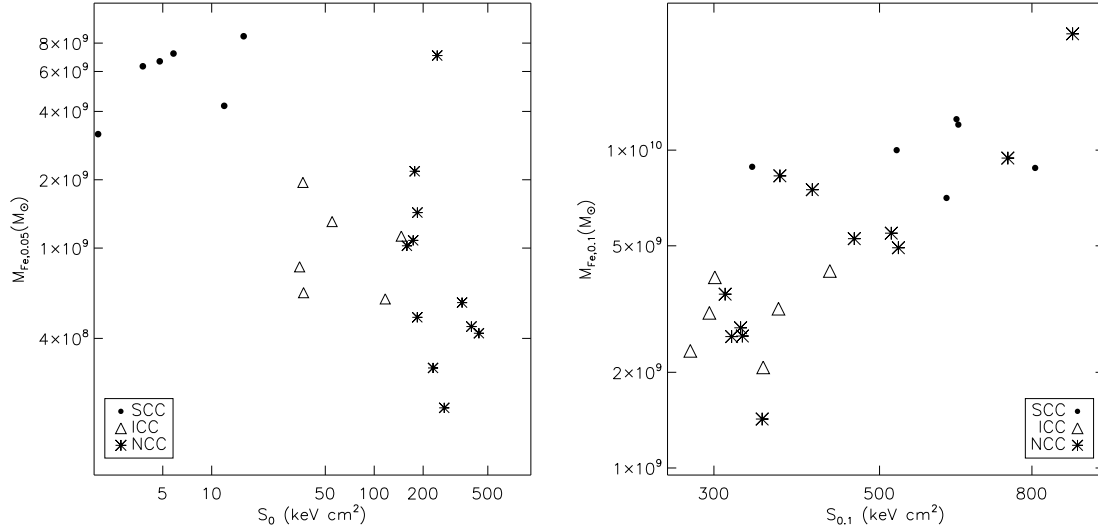


**Figure 4.7.** Correlation between  $M_{\text{Fe},0.05}$  and the entropy pedestal  $S_0$  (left),  $M_{\text{Fe},0.1}$  and  $S_{0,1}$  (right).

#### 4.3.4 Relations between gas entropy and metallicity

The ICM iron mass is a key observable to constrain the cumulative past star formation history in galaxy clusters. Its relations with other observables such as the cluster optical light, total cluster mass, stellar mass and gas entropy, together with its redshift evolution, allow to study the enrichment processes. Moreover, while the production of metals is linked to processes of star formation, its radial profile is determined by different physical processes, such as ram-pressure stripping, galactic winds powered by supernovae and AGN activity, merger mechanism (Gnedin, 1998).

Following the work of De Grandi et al. (2004) on local clusters, we present measured iron abundances in the ICM, their evolution with the redshift  $z$  and their correlation with the entropy. We adopt the solar abundance ratios from Anders & Grevesse (1989) with  $Z_{\odot} = \text{Fe}/\text{H} = 4.68 \times 10^{-5}$  by number.

We first have determined measures of projected metallicity profiles  $Z_{\text{Fe}} = Z_{\text{Fe}}(r) = n_{\text{Fe}}/n_{\text{H}}$ , (in units of  $Z_{\odot}$ , that is the solar abundance of iron), where  $n_{\text{Fe}}$  and  $n_{\text{H}}$  are the iron and hydrogen densities (by number) respectively. Notice  $Z_{\text{Fe}}^{\text{proj}}$  has been integrated up to  $R_{\text{spec}}$  without masking the cooling region, to compare our results with the literature available. In our sample, we find hints of possible negative evolution with redshift, with Spearman's rank coefficient of  $r_s = -0.12$  for 22 d.o.f. (probability of null correlation  $p = 0.59$ ), in rough agreement with Balestra et al. (2007), whose sample covers a wider range of  $z$ . After the deprojection of the spectral results (see Chapter 3), we have calculated the iron mass enclosed within a sphere of radius  $R$  by integrating the iron mass density,  $\rho_{\text{Fe}}$ , over the cluster volume. The total iron mass in solar units can be then written as:

$$M_{\text{Fe}}(< R) = 4\pi A_{\text{Fe}} m_{\text{H}} \frac{Z_{\odot}}{M_{\odot}} \int_0^R Z_{\text{Fe}}(r) n_{\text{H}}(r) r^2 dr, \quad (4.8)$$

where  $A_{\text{Fe}}$  is the atomic weight of iron and  $m_{\text{H}}$  is the atomic unit mass. To integrate the observed profiles at any radius, we have linearly interpolated the metallicity mass profiles within overdensities  $R_{\delta} = 0.05 R_{200}$ ,  $R_{\delta} = 0.1 R_{200}$  and  $\Delta = 2500$ , which roughly correspond to 100 – 150, 200 – 300 and 400 – 600 kpc for our sample, respectively.

No significant evolution with  $z$  of  $M_{\text{Fe}}(< R_{2500})$  (probability of null correlation  $p = 0.94$ ) and  $M_{\text{Fe}}(< R_{0.05})$  ( $p = 0.52$ ) is measured. Instead, we observe a strong segregation between SSC, ICC and NCC sources, with SCC clusters that tend to have higher metallicity mass by a factor of  $\sim 2$  within  $R_{2500}$  and by an order of magnitude within  $R_{0.05}$ , which roughly corresponds to the cooling region. The iron mass excess associated with cool core regions could be entirely produced by the brightest cluster galaxy (BCG), which is always found at the centre of cool core clusters, via SN- or AGN- induced winds (De Grandi et al., 2004). Moreover, we confirm the existence of a correlation between  $M_{\text{Fe},\delta}$  and  $S_{\delta}$ . In Fig. 4.7, we present the correlation between the  $M_{\text{Fe},0.05}$  as a function of the entropy pedestal  $S_0$  (see Sect. 4.3.2): we can see an anti-correlation between the two quantities, as expected in a picture where the cooling is the likely predominant physical process in the cooling region. Enrichment from recent Supernovae type Ia in the cD galaxies can explain the central metal abundance excess observed in cooling core clusters (De Grandi et al., 2004; Böhringer et al., 2004). On the contrary, outside the cooling region, we observe again nearly self-similar relation between  $M_{\text{Fe},0.1}$  and  $S_{0.1}$  (see Fig. 4.7) as we have seen in Sect. 4.3.1 for the  $S_{\delta} - T_{\text{ew}}$  relation.

Assuming a synthesized iron mass per SNIa event  $m_{\text{Ia}}$  of  $0.74 M_{\odot}$  (Nomoto et al., 1997) and an energy output of  $10^{51}$  erg, we estimate that  $1 - 3 \times 10^{10}$  SNIa events in the region inside  $R_{2500}$  are required to produce  $M_{\text{Fe},2500} \gtrsim 0.8 \times 10^{10} M_{\odot}$  observed in NCC clusters. This number of SNe corresponds to a global energy output of  $1 - 3 \times 10^{61}$  erg over the entire lifetime of the cluster, that is lower by a factor 2-4 than the excess of energy  $\Delta U_{2500}$  estimated in Sect. 4.3.3 ( $\Delta U^{\text{NCC}} \sim 10^{62}$  erg), suggesting the action of other sources of non-gravitational energy to fully account for this observed excess.

## 4.4 Discussion

The main results emerging from our study of the entropy profiles in hot ( $kT_{\text{gas}} > 6$  keV) galaxy clusters at  $z > 0.1$  are that these profiles, although similar in the outskirts where they behave as a power law with slope 1.0 – 1.2, are remarkably discrepant in the central regions, with SCC objects that show a power-law behaviour down to the innermost spatially resolved regions and NCC clusters having profiles that flatten to a constant value at  $r < 0.3 R_{2500}$  (Fig. 4.3.2). Accordingly, the comparison between gas and dark matter temperature profiles (Fig. 4.1) reveals that SCC clusters do not present any significant energy excess at any radius, whereas ICC and, more dramatically, NCC objects show  $\Delta E = 3/2 \Delta kT$  larger than few keV in the cooling region and above. Note that the situation near the boundary of the sources is unclear, because the statistical errors are very large, the effect of possible anisotropies in the DM are there more prominent and we are assuming some constraints on the dark matter temperature at  $R_{\text{spec}}$ . This excess of energy with respect to the 'gravitational energy floor' associated to the DM

temperature profile can be interpreted as an indication of the presence of some form of non-gravitational energy that can constrain the mechanisms affecting the ICM thermal history and the observed entropy profiles. Indeed, in agreement with  $\Delta E \approx 0$  over the entire radial range, we observe that SCC clusters have very low entropy pedestal values  $S_0$  of few keV cm<sup>2</sup>, while the higher and more scattered values of  $S_0$  measured in ICC and, particularly, in NCC systems can be justified by an injection of energy  $\Delta E$  of 1-10 keV, that, distributed over scales  $\lesssim 100 - 300$  kpc, explains also their flatter entropy profiles. The regular behaviour of the entropy profiles outside  $0.1 R_{200}$  is also in agreement with the fact that  $\Delta E$  is low at these radii, where we have to consider the limitations of our analysis near  $R_{\text{spec}}$  as mentioned above. This scenario is also supported from our results on the  $S - T$  relation, where we observe an higher normalization, more significant in the inner regions ( $\delta = 0.1$ ; see Table 4.3) of the SCC subsample with respect to ICC and NCC sources. We note hints of larger entropy values at higher redshift when our measurements in CC clusters are compared to the best-fit results obtained in nearby samples, with a more significant deviations observed at  $0.1 R_{200}$  than at  $0.3 R_{200}$ , suggesting that cores in our CC objects are not yet well defined from the radiative processes. Moreover, the observed mild differences in the slopes of the entropy profile, with  $\alpha$  that becomes slightly higher by considering NCC, ICC, and SCC sources, respectively ( $\alpha^{\text{SCC}} = 1.18 \pm 0.11$ ,  $\alpha^{\text{ICC}} = 1.07 \pm 0.16$  and  $\alpha^{\text{NCC}} = 0.95 \pm 0.21$  for the power-law model) can be explained by looking at the temperature and density profiles (Figure 4.1), which are a bit flatter for non-cooling core systems: this trend can be justified with small energy excess ( $\Delta E \sim 1-2$  keV) at large scale in the NCC objects compared to the NCC and SCC ones. The radial behaviour of  $\Delta E(r)$  is also confirmed by the analysis made in Chapter 3, where we noticed a strong negative evolution in the  $y_\Omega - \text{X-ray}$  and  $y_\Omega - \text{SZ}$  scaling relations (see Sect. 4.3.3).

All our systems are the products of the hierarchical scenario, how is suggested from the similar behaviour of the gas temperature, density, entropy and dark matter profiles in the regions above the cores. On the contrary, the cooling region characterizes SCC, ICC, and NCC systems. In particular, continuous interplay between cooling and some form of (pre-)heating can explain the variety of the properties observed, with SCC dominated from the cooling phase and, on the other end, NCC still subjected to some effects of heating.

Theoretical models must predict the magnitude of the observed  $\Delta E(r)$ , and the impact of the non-gravitational processes associated to this excess in the central regions. These models fall into three main classes: preheating, where the gas collapsing into the dark matter potential well is preheated by some mechanism, before clusters were assembled at an early epoch (Kaiser, 1991; Balogh et al., 1999; Tozzi & Norman, 2001; Borgani et al., 2005); local heating by AGN activity, star formation or supernovae (Bialek et al., 2001; Brighenti & Mathews, 2006; Babul et al., 2002; Borgani et al., 2002); cooling, which seems to be able to remove low-entropy gas in the centre of the clusters, producing a similar effect to non-gravitational heating (Bryan, 2000; Muanwong et al., 2002; Borgani, 2004). Hereafter, we review the main characteristics of these models and discuss how they are consistent with our observational constraints.

### 4.4.1 Preheating models

Models of pre-heating, where a constant energy input is injected either prior of the cluster collapse (0.1 – 0.3 keV per particle, e.g. Navarro et al., 1995; Tozzi & Norman, 2001) or after the cluster formation (1 – 3 keV per particle, e.g. Metzler & Evrard, 1994; Loewenstein, 2000; Wu et al., 2000; Bower et al., 2001), could justify, only partially in NCC objects, the observed magnitude of  $\Delta E(r)$ , but not its radial behaviour. Nevertheless, as pointed out by Borgani et al. (2005) by studying hydrodynamical simulated clusters, there is no possibility to inject a large quantity of energy per particle ( $\lesssim 1$  keV), unless a large isentropic core is produced in the entropy profile, core that is not observed in our profiles in agreement with other works (Ponman et al., 2003; Pratt & Arnaud, 2003; Pratt & Arnaud, 2005).

Ponman et al. (2003) suggest that any raise of the temperature and/or decrease of the density in the gas inside the primordial structures due to preheating can get largely raised by the accretion shock. Following the model of Dos Santos & Doré (2002), Ponman et al. (2003) estimated that a mild raise of the entropy of the gas confined to filaments ( $\sim 10 - 100 \text{ keV cm}^2$ , corresponding to a temperature of  $\sim 10^{-1}$  keV) can be boosted by the accretion shock to the observed value of  $S$  ( $\sim 100 - 1000 \text{ keV cm}^2$ ). They point out that an interplay between shock and smoothing of the primordial gas due to a preheating can justify the observed properties of the gas entropy, given the above upper limits on the energy budget of the preheating and being the slope of the entropy profile close to the value predicted from shock heating.

Preheating prior of the cluster collapse should be a energetically favorable mechanism compared to *in situ* heating to cast further energy into the gas before it is concentrated in the gravitational potential well of the DM halo, since less energy is required to increase the entropy of the gas by a given amount when its density is lower as in the filaments. In fact we observe that in the shock dominated collapse scenario, a mild injection of energy through preheating can greatly amplify the final energy  $E_{\text{fin}}$  of the post-shocked particles, being  $E_{\text{fin}} \propto E_{\text{in}}$ , with  $E_{\text{in}}$  the initial energy. Borgani et al. (2005) show that smoothing the accretion pattern by preheating in the case of simulations without radiative physics amplifies the entropy generation out to the radius where the accretion shock acts. Nevertheless, the effect seems to be substantially reduced when cooling is also taken into account.

However, our estimates of  $\Delta E(r)$  show not a constant profile but instead a declining one outwards. This behaviour cannot be explained by any preheating mechanism, either prior or after cluster collapse, even though entropy is amplified through subsequent shock heating. Results for X-ray bright nearby objects by Pratt et al. (2006) support this conclusions, because their scaled entropy profiles show increasing scatter in the inner regions, with a dispersion ( $\sim 60$  per cent) definitely higher than the value found in simulations including filamentary preheating ( $\sim 30$  per cent, see Voit 2005a).

### 4.4.2 Heating models

In principle, heating can amplify the boosting of the entropy out to the radius where accretion shocks are taking place, especially in low mass systems, since they are accreted by smaller subhalos where the gas is more smoothed by the extra heating. As pointed out by Borgani et al. (2005), local heating due to star formation activity is not able alone to prevent overcooling and to reproduce the predicted star formation as low as measured (Muanwong et al., 2002) and the observed entropy profile: maybe we have to appeal to further sources of non-gravitational energy, like AGN, not taken into account in such hydrodynamical simulations, or different physical mechanisms to distribute the energy inside the ICM.

The need of this further source of non-gravitational energy is also confirmed by the analysis made in Sect. 4.3.4, where we observe that the number of supernovae we require to reproduce the observed metallicity is not able to account for all the excess of energy  $\Delta U_{2500}$ .

A gentle, transonic heating process, such as the weak shocks detected in the Perseus cluster (Fabian et al., 2003), can provide a framework by which one can explain all the observed properties, like the flattening of the entropy profile in the innermost regions ( $\lesssim$  a few tens of kpc) even of SCC clusters, and the spikes of metallicity measured in the centre of SCC sources (see Fig. 4.7). Weak shocks are indeed likely not able to prevent metals' accumulation in the innermost regions. Donahue et al. (2005, 2006) pointed out that the central cooling time of the SCC galaxies ( $\sim 10^8$  yr) is consistent with the time scale of the activity of radio sources ( $\sim$  a few  $10^7$  yr) at the centre of clusters. Energy casted by the radio jet ( $\sim 10^{45}$  erg/s) can then produce the observed flattening of the entropy profiles on scale of a few tens of kpc. Gasdynamical models of jets flows proceeding from a central supermassive black hole and entering surrounding gas may heat the ICM by casting mass and energy outwards till scale  $\sim$  hundreds of kpc, possibly lowering the cooling rate (Brighenti & Mathews, 2006). Nevertheless the above picture does not explain the excess of energy  $\Delta E$  in the regions outside the core, where we have probably to require some other form of heating, like e.g. shocks induced from merging activity.

Whatever sources of non-gravitational energy we have to appeal, they must fuel energetically the ICM in such a way to reproduce the magnitude and the radial behaviour of  $\Delta E(r)$ , casting energy (in the order of few keV) and metals preferentially in the innermost regions.

### 4.4.3 Cooling models

Cooling plays a key role to explain the observed excess of energy  $\Delta E(r)$ . In fact,  $\Delta E(r)$  is higher in the central regions moving from SCC to ICC and to NCC systems. Cooling can easily account for this trend through radiative losses of the accumulated thermal energy. In the SCC clusters,  $T_{\text{gas}}$  is roughly equal to  $T_{\text{DM}}$  suggesting either that a perfect balance between cooling and heating is established, permitting the radiative losses of the only amount of energy in excess with respect to the one associated to the DM, or that heating is episodic and we are observing structures in their undisturbed phase.

In a similar manner, Voit et al. (2002) have argued that the entropy responsible for the break of the self similarity is not a global property of the ICM, but rather a property set by radiative cooling: they point out that the observed entropy value at the core radii of groups and clusters is near to the entropy at which  $t_{\text{cool}} \approx t_{\text{Hubble}}$ .

A model to explain the observed features in the entropy profile is that proposed by Voit & Bryan (2001). They show how cooling and supernovae heating act to eliminate high compressible gas with  $S < S_c$ , being  $S_c$  the cooling threshold, from the X-ray phase. Much of the condensation and the feedback is prior of the epoch of clusters' formation, balancing these processes reciprocally: more the cooling is effective, more the star formation is active with release of energy to the ICM and consequent reduction of the cooling itself. This picture is likely not wholly adequate, leading to a very large isentropic core in the entropy profiles, which are not observed.

## 4.5 Summary and conclusions

We have presented *Chandra* observations of the entropy profiles and scaling properties of a sample of 24 galaxy clusters spanning the redshift range 0.14–0.82 and classified accordingly to their central cooling time in strong (SCC), intermediate (ICC) and non-cooling core (NCC) systems. We have performed a spatially resolved spectral analysis and recovered the gas density, temperature  $T$  and entropy  $S$  profiles at high spatial resolution and in a non-parametric way. We have shown that those entropy profiles are remarkably similar outside the central regions with a typical entropy level at  $0.1 R_{200}$  of  $100 - 500 \text{ keV cm}^2$ , and have a central entropy plateau covering a wide range of values ( $\sim$  a few– $200 \text{ keV cm}^2$ ), with the highest values associated to NCC objects. The CC clusters show larger values of the entropy than the one measured in nearby luminous systems, with a more significant deviations observed at  $0.1 R_{200}$  than at  $0.3 R_{200}$  with respect to the best-fit results in Pratt et al. (2006), suggesting that the core in our CC objects are not yet well defined from the cooling processes.

We have studied the radial behaviour of the temperature of the gas ( $T_{\text{gas}}$ ) and of the dark matter ( $T_{\text{DM}}$ ). We have found that  $T_{\text{gas}}$  is always higher than  $T_{\text{DM}}$ : for the SCC clusters, the difference of temperature  $\Delta kT = kT_{\text{gas}} - kT_{\text{DM}}$  is negligible, while it is large for the non-cooling core clusters (up to  $\sim 10 \text{ keV}$  per particle), with  $\Delta kT(r)$  that declines outwards.

We conclude that none of the models of (pre-)heating and cooling discussed in literature is able to explain alone the observed trends of the entropy profiles and of  $\Delta E(r)$ . Likely, we have to require an interplay of these processes. A scenario with shock dominated collapse and preheating in the primordial filaments might account for most of the extra-gravitational energy, as confirmed by the slopes of the entropy profiles near the theoretical value of 1.1 expected in the accretion shock picture (Tozzi & Norman, 2001). As described in Sect. 4.4.1, this should be an energetically favorable mechanism compared to the *in situ* heating, amplifying significantly the final energy  $E_{\text{fin}}$  of the post-shocked particles. On the other side, gentle, sub-sonic heating processes, e.g. supported from AGN's jets, can account for many of the observed properties, but not for excess of energy

still measured outside the core (see Sect. 4.3.3).

The relaxed environment of SCC clusters is required to enhance the central metal abundance and total iron mass in correspondence of low entropy regions (see Sect. 4.3.4). There, the cooling is so efficient to remove on short time scale the excess of energy per particle of the ICM, permitting (i)  $T_{\text{gas}}$  to approach the dark matter value  $T_{\text{DM}}$  and (ii) the other physical parameters used in describing the entropy profile, like, e.g.,  $S_0$ ,  $r_{\text{break}}$ , to vary.

Overall, the different observed behaviour of the entropy profiles of SCC, ICC and NCC massive clusters suggest that we are observing the end products of the hierarchical model for structure formation. They represent different stages of the relative relevance of heating and cooling in regulating the feedback that shapes the ICM distribution: galaxy clusters are identified either as NCC objects when heating, probably due to a residual merging activity and feedback from AGNs triggered from the merger itself, is predominant, or as SCC systems when the radiative losses are energetically prominent, being ICC objects an intermediate case between the two.



## Chapter 5

# Bayesian inference in X-ray galaxy clusters with Sunyaev Zel'dovich measurements - Physical properties of the gas out to $R_{200}$

**T**his chapter aims at presenting a Bayesian approach to combine X-ray and Sunyaev Zel'dovich (SZ) data, observed with Chandra and the Cosmic Background Imager (CBI), respectively. We show that combining X-ray and SZ allows to study the outskirts of the clusters out to  $R_{200}$ , well beyond the regions accessible with X-ray observations ( $\leq 0.3 - 0.5 R_{200}$ ), thanks to the great field of view of CBI and the strong dependence of the SZ interferometric signal on the external regions. In particular we show how it is possible to recover the density, the temperature and the entropy of the gas in the outskirts in a non-parametric way through a Reversible Jump Markov Chain Monte Carlo technique (RJMCMC).

### 5.1 INTRODUCTION

Although in the last few years the modeling of the formation of the structures in the Universe has made enormous progresses, a complete understanding of the connections between the physical properties and the observables of galaxy clusters is far from being reached.

The observational X-ray data of the last years showed that the physics of the intracluster medium is much more complex than it was thought, highlighting several discrepancies with theoretical predictions that are currently being analyzed with hydrodynamical simulations.

On one side, X-ray observations have proved that the so-called self-similar model (Kaiser , 1986; Evrard & Henry, 1991, and Sect. 3.4), where the gravity is the only responsible for the physical properties of galaxy clusters, is not able to describe the scaling relations of galaxy clusters, especially for low-mass systems: this indicates that

the gravitational collapse is not the only process that significantly influences the formation of structures. It is widely believed that some sort of feedback is able to affect the thermodynamics of the gas and that a complete understanding of this aspect will solve the discrepancy between observations and theory. The recent improvements in the physical modeling of the ICM with simulations (the addition of non-gravitational physics, e.g. radiative cooling, star formation, feedback from supernovae and AGNs, galactic winds) were able to explain the breaking of the self-similarity but could not solve the problem completely.

Beside the X-ray analysis the thermal SZ effect (Sunyaev & Zeldovich, 1970) offers a powerful tool for investigating the same physical properties of the ICM, being the electron component of cosmic baryons responsible of both the X-ray emission and the SZ effect. The advantage of the latter on the former is the possibility of exploring clusters at higher redshift, because of the absence of the cosmological dimming. Moreover, since the SZ intensity depends linearly on the density, unlike the X-ray flux, which depends on the squared density, with the SZ effect it is possible to obtain estimates of the physical quantities of the sources reducing the systematic errors originated by the presence of sub-clumps and gas in multi-phase state and to study the physics of the ICM in a complementary way to the X-ray analysis. A joint X-ray and SZ analysis allows to study the external volumes of the clusters well beyond the regions resolved with X-ray observations ( $\leq 0.3 - 0.5 R_{200}$ ), thanks to the great field of view of SZ bolometers like CBI ( $\sim 45$  arcmin) and the strong dependence of the SZ interferometric signal on the external regions. So it is possible to study the radial behaviour of the deprojected physical cluster properties, like temperature, density, entropy, gas mass and total mass up to the virial radius.

In this Chapter we aim at understanding the properties of the ICM and DM in the outskirts of the galaxy clusters. In particular, we will concentrate on the distribution of matter in galaxy clusters, which is a fundamental question on structure formation in an expanding universe, so as to understand which of these models better reproduces the observed physical properties. Early works on this matter have been addressed just on simulations (see Merritt et al., 2006; Roncarelli et al., 2006), since just X-ray data cannot observe the outskirts of the clusters, and through a likelihood method: on the contrary we adopt a more convenient Bayesian analysis.

The Chapter is organized as follows. In Sect. 5.2 we discuss why it is possible to study the outskirts of galaxy clusters through interferometric Sunyaev-Zel'dovich data. Sect. 5.3 is devoted to a general discussion about the Bayesian statistics, while in Sect. 5.4 we describe the cluster sample and the analysis adopted. In Sect. 5.5 we present a test of our Bayesian X-ray+SZ method on mock observations, while in Sect. 5.6.1 we summarize our main conclusions. We leave to the Appendix B the discussion of some technical detail of our method.

## 5.2 The Sunyaev-Zel’dovich effect

### 5.2.1 Determination of the Sunyaev-Zel’dovich quantities

In Sect. 2.4 we have shown that the thermal SZ effect is a very small distortion of the spectrum of the cosmic microwave background (CMB), due to the Inverse Compton scattering between the photons of the CMB and the hot ( $\sim 10^7 - 10^8$  K) electrons of the ICM trapped in the gravitational potential well of the dark matter halo (Sunyaev & Zeldovich, 1970; Birkinshaw, 1999). The magnitude of this effect can be evaluated by considering the Compton parameter  $y(\theta)$ , defined as

$$y(\theta) = \frac{\sigma_T}{m_e c^2} \int P_e(\vec{r}) dl , \quad (5.1)$$

which is proportional to integral of the electronic pressure  $P_e$  of the ICM along the line of the sight  $l$  (see Sect. 2.4).

We also remember that the best fit models are usually computed using visibilities (i.e. data in the Fourier domain) instead of intensity (i.e. data in the image domain). The visibility  $V(u, v)$  in the  $uv$ -plane is the Fourier transform ( $\mathcal{FT}$ ) of the brightness  $I(\varphi, \theta)$  (Sect. 2.4). In the case of radial symmetry, where the  $\mathcal{FT}$  transform becomes the Hankel transform ( $\mathcal{HT}$ ),  $V(u, v)$  reads:

$$\begin{aligned} V(\vec{u}) &= \int_{-\infty}^{\infty} d\vec{\varphi} B(\vec{\varphi}) I(\vec{\varphi}) e^{i2\pi\vec{\varphi}\cdot\vec{u}} = \\ &2\pi \int_0^{\infty} B(\varphi) I(\varphi) J_0^k(2\pi\varphi u) \varphi d\varphi . \end{aligned} \quad (5.2)$$

Given the poor coverage of the  $uv$ -plane of the actual SZ observations, the best way to constrain the physical parameter is to work in the Fourier domain, by performing an  $\mathcal{HT}$  of the X-ray model and comparing it with the observed visibilities.

### 5.2.2 Why to study the outskirts through interferometric Sunyaev-Zel’dovich data?

Here we discuss briefly why SZ data can constrain the physical properties of the gas and DM in the outskirts of galaxy clusters. As in the last years a lot of X-ray data becomes available, most of the observational research in galaxy clusters is mainly based on X-ray observations. Nevertheless X-ray observations are subject to several limitations: i) the cosmological dimming of the X-ray surface brightness ( $\sim (1+z)^{-4}$ ); ii) difficulty in observing the external regions ( $\gtrsim 1/3 - 1/2$  of the virial radius) of clusters; iii) systematics in the reconstructed physical properties due to wrong background subtraction.

All of these problems can be overcome by studying the Sunyaev Zel’dovich effect (SZ). In fact advantages of dealing with SZ data are:

- 1. Bias-free determination of the physical properties.** Since the SZ intensity depends linearly on the density, unlike the X-ray flux, which depends on the squared density,

with the SZ effect it is possible to obtain estimates of the physical quantities of the sources reducing the systematic errors originated by the presence of sub-clumps and gas in multi-phase state.

2. **Independence of the SZ signal of  $z$ .** The advantage of the SZ effect on the X-ray measurements is the possibility of exploring clusters at higher redshift, because of the absence of the cosmological dimming.
3. **Contamination of the unresolved sources of background.** The contribution of unresolved sources of background below the detection limit of the CBI to the total noise is equal to zero in SZ interferometric data, unlike the X-ray ones. So working on the Fourier domain instead of the image one allows to overcome the problem of the contamination, for example, originated by the cosmic filaments along the line of the sight which have angular dimension  $\gtrsim 1/(2u_i) \sim 45'$ , being  $u_i$  the shortest baselines of CBI.
4. **Properties of the background.** In interferometric data the noise is not due to unresolved sources of background, as in X-ray data, but just to thermal noise, i.e. due to the electronic components of the instrument. So in an X-ray source we must subtract a background of value  $\mu_x \pm \sigma_x$  to the data, while in a SZ interferometric dataset we must not subtract any background, being the thermal noise equal to  $0 \pm \sigma_{SZ}$ , i.e. with mean value equal to zero. This is very important because, for example, the subtraction of the noise can lead to large systematic errors in the determination of the physical properties of the gas near the boundary of X-ray observations, due to uncertainties in the determination of the level of the same X-ray background: using interferometric data avoids this problem.

In this sense, by analyzing mock clusters (see Sect. 5.5), it is interesting to show that just  $\sim 5$  per cent of the total X-ray photons of a cluster is outside  $R_{\text{spec}}$ , and moreover it is inaccessible, being overwhelmed by the X-ray background.

5. **Energy distribution.** First, by considering Eq. (5.2), we see that the zero-th baseline  $V(0)$  can be rewritten as:

$$V(0) = \int_{-\infty}^{\infty} d\vec{\Phi} B(\vec{\Phi}) I(\vec{\Phi}) \simeq D_a^{-2} \int_V P dV , \quad (5.3)$$

where in the second equality we have neglected the effects of the primary beam, and where  $D_a$  is the diameter distance. So the physical meaning of  $V(0)$  is that *the zero-th baseline is proportional to the total energy budget of the clusters*. More in general, the shortest baselines  $u_i$  of CBI near to the zero-th baseline are sampling regions in the image plane on angular scales  $\sim 1/(2u_i) \lesssim R_{200}/D_a$ , and therefore are strictly related to the total energy budget of the clusters. In Figure 5.2.2 we plot the cumulative energy function  $E(< r)$  normalized to  $E_{200}$  as a function of  $r/r_{200}$ . As we can see, just  $\sim 60$  per cent of the total energy is accessible to the X-ray observations ( $R_{\text{spec}} \lesssim 0.3 - 0.5 R_{200}$ ), while the remaining part is confined in the outskirts, accessible just through SZ data (the SZ boundary is  $\sim 2.5$  times the X-ray

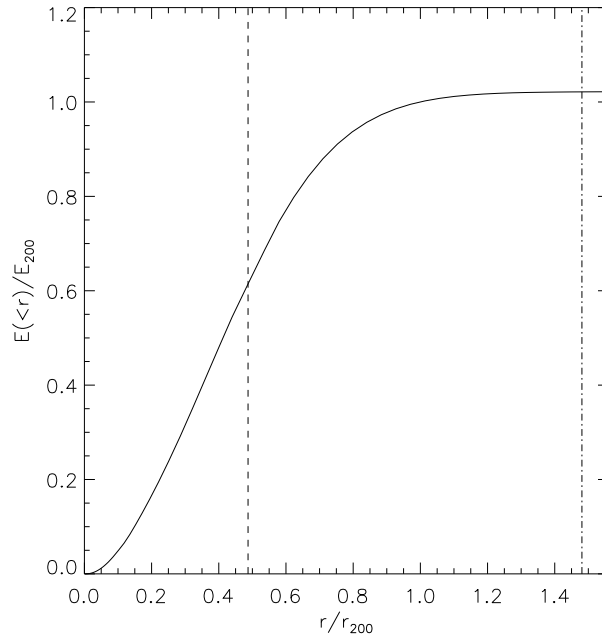


**Figure 5.1.** Cumulative energy function normalized to  $E_{200}$  as a function of  $r/r_{200}$ . The dashed line represents the X-ray boundary, while the dot-dashed refers to the SZ boundary.

one). So the more we are observing on larger angular scales till  $\sim R_{200}/D_a$ , the more we are collecting an higher total energy  $E(<r)$ , i.e. the more the signal  $V_i$  on the shortest baselines  $u_i$  (and the signal to noise ratio of  $V_i$ ) increases, being the errors on  $V_i$  (the thermal noise) roughly independent of the angular scale. So we have that the SZ boundary is  $\sim 2.5$  times the X-ray one (see Figure 5.2.2).

The above physical behaviour is wholly antithetic to the one of the brightness in X-ray data, in the image domain: the X-ray brightness drops very fast by moving towards  $R_{\text{spec}}$  like  $\sim n^2\Lambda(T)$ , so we have that near the X-ray boundary the significance of our measurements is low, possibly affected by systematics due to non accurate estimates of the X-ray background.

## 5.3 Bayesian inference

### 5.3.1 The Bayes theorem

We start by reviewing briefly the basic principles of Bayesian inference. Given some dataset  $\mathbf{D}$ , suppose we are interested in estimating the values of a set of parameters  $\boldsymbol{\theta}$  in some underlying model of the data. For any given model, one may write down an expression for the *likelihood*  $P(\mathbf{D}|\boldsymbol{\theta}, \mathcal{H}_i)$  of obtaining the data vector  $\mathbf{D}$  given a particular set of values for the parameters  $\boldsymbol{\theta}$ . In addition to the likelihood function, one may impose a *prior*  $P(\boldsymbol{\theta}|\mathcal{H}_i)$  on the parameters, which represents our state of knowledge (or prejudices)

regarding the values of the parameters *before* analysing the data  $\mathbf{D}$ . Bayes' theorem then reads,

$$P(\boldsymbol{\theta}|\mathbf{D}, \mathcal{H}_i) = \frac{P(\mathbf{D}|\boldsymbol{\theta}, \mathcal{H}_i)P(\boldsymbol{\theta}|\mathcal{H}_i)}{P(\mathbf{D}|\mathcal{H}_i)} , \quad (5.4)$$

that is

$$\text{Posterior} = \frac{\text{Likelihood} \times \text{Prior}}{\text{Evidence}} , \quad (5.5)$$

which gives the *posterior* distribution  $P(\boldsymbol{\theta}|\mathbf{D}, \mathcal{H}_i)$  in terms of the likelihood, the prior and the *evidence*  $P(\mathbf{D}|\mathcal{H}_i)$  (which is also often called the marginalized likelihood).

Two levels of inference can be often distinguished in the process of data modeling. At the first level of inference we assume that a particular model is true, and we fit that model to the data, i.e. we infer what values its free parameters should plausibly take, given the data. The results of this inference are often summarized by the most probable parameter values, and error bars on those parameters. This analysis is repeated for each model. The second level of inference is the task of model comparison. Here we wish to compare the models in the light of the data, and assign some sort of preference or ranking to the alternatives. We write down the Bayes' theorem for two levels of inference described below, so as to see explicitly how Bayesian model comparison works.

- 1. Model fitting.** At the first level of inference, we assume that a model,  $\mathcal{H}_i$ , say, is true, and we infer what the model's parameters  $\boldsymbol{\theta}$  might be, given the data  $\mathbf{D}$ . Using Bayes' theorem, the posterior probability of the parameters  $\boldsymbol{\theta}$  is given by Eq. (5.4): thus one normally works instead with the 'unnormalised posterior'

$$\bar{P}(\boldsymbol{\theta}|\mathbf{D}, \mathcal{H}_i) = P(\mathbf{D}|\boldsymbol{\theta}, \mathcal{H}_i)P(\boldsymbol{\theta}|\mathcal{H}_i) , \quad (5.6)$$

where we have written  $\bar{P}$  to denote the fact that the probability distribution on the left-hand side is not normalized to unit volume. The normalizing constant  $P(\mathbf{D}|\mathcal{H}_i)$  is commonly ignored, since it is irrelevant to this level of inference, i.e., the inference of  $\boldsymbol{\theta}$ ; but it becomes important in the second level of inference, and we name it the evidence for  $\mathcal{H}_i$ .

- 2. Model selection.** At the second level of inference, we wish to infer which model is most plausible given the data. To rank alternative models  $\mathcal{H}_i$ , a Bayesian approach evaluates the evidence  $P(\mathbf{D}|\mathcal{H}_i)$ . The posterior probability of each model is:

$$P(\mathcal{H}_i|\mathbf{D}) = \frac{P(\mathbf{D}|\mathcal{H}_i)P(\mathcal{H}_i)}{P(\mathbf{D})} , \quad (5.7)$$

where  $P(\mathbf{D}) = \sum_i P(\mathbf{D}|\mathcal{H}_i)P(\mathcal{H}_i)$ . Notice that the data-dependent term  $P(\mathbf{D}|\mathcal{H}_i)$  is the evidence for  $\mathcal{H}_i$ , which appeared as the normalizing constant in (5.7). For the model  $\mathcal{H}_i$ , the probability density for an observed data vector  $\mathbf{D}$  is given by

$$P(\mathbf{D}|\mathcal{H}_i) = \int \bar{P}(\boldsymbol{\theta}|\mathbf{D}, \mathcal{H}_i) d\boldsymbol{\theta} = \int P(\mathbf{D}|\boldsymbol{\theta}, \mathcal{H}_i)P(\boldsymbol{\theta}|\mathcal{H}_i) d\boldsymbol{\theta} . \quad (5.8)$$

The second term,  $P(\mathcal{H}_i)$ , is the subjective prior over our hypothesis space, which expresses how plausible we thought the alternative models were before the data arrived. Assuming that we choose to assign equal priors  $P(\mathcal{H}_i)$  to the alternative models, models  $\mathcal{H}_i$  are ranked by evaluating the evidence, being

$$K = P(\mathcal{H}_i|\mathbf{D})/P(\mathcal{H}_j|\mathbf{D}) = P(\mathbf{D}|\mathcal{H}_i)/P(\mathbf{D}|\mathcal{H}_j) , \quad (5.9)$$

where  $K$  is called Bayesian factor. A value of  $K > 1$  means that  $H_i$  is more strongly supported by data under consideration than  $H_j$ .

So we can rewrite the Bayes' theorem as:

$$\begin{array}{lcl} \text{Prior} \times \text{Likelihood} & = & \text{Posterior} \times \text{Evidence} \\ \text{assumptions \& measurements} & \Rightarrow & \text{inference(I,II)} \end{array} \quad (5.10)$$

where with inference(I,II) we indicate the above two levels of inference.

### 5.3.2 Model fitting: the MCMC algorithm

#### The Component-Wise Hastings algorithm

A Markov chain is a series of random variables,  $x^1 ; x^2 ; \dots , x^t$  in which the distribution of  $x^{t+1}$  at a given time  $t + 1$  is mediated entirely by the value of  $x^t$  at time  $t$ . The Markov Chain Monte Carlo (MCMC) method is a robust technique to build these chains and it can be used to obtain the probability distribution function of model parameters based on observational data (Skilling, 1998; Neal, 1993).

To construct the Markov chain, we choose candidate parameter values  $x^t = (x_1^t, x_2^t, \dots, x_p^t) \in \mathbb{R}^p$ , drawing samples  $x_i^t$  from the whole allowed parameter space by assuming a convenient distribution  $\pi_i$  of these proposal density. When we have a sufficiently high number of iterations, the frequency of the occurrence of the parameter tends to the true probability distribution function (e.g. Gilks et al., 2003; MacKay, 1997), so we can determine the expectation values and their errors by considering the percentiles of the distribution.

Here we will concentrate on the Component-Wise Hastings algorithm (Levine et al., 2005), to determine the distribution of the best-fit parameters. The Component-Wise Hastings algorithm proceeds by splitting the state vector into a number of components and updating each in turn by a series of Component-Wise Hastings transitions. For simplicity we put  $x = x^t$ . Suppose that we split the  $p$ -dimensional vector  $x$  into  $k \leq p$  components, so that  $x = (x_1, \dots, x_k) \in \mathbb{R}^p$ . Having selected component  $x_i$  to be updated, the Component-Wise Hastings transition kernel involves sampling a new state  $x' = (x_1, \dots, x_{i-1}, y, x_{i+1}, \dots, x_k)$ , sampling  $y$  from the conditional distribution of  $x_i$  given the other variables: if we denote by  $\pi(x_i | x_{(i)})$  the conditional distribution of  $x_i$ , given the values of the other components  $x_{(i)} = (x_1, \dots, x_{i-1}, x_{i+1}, \dots, x_k)$ ,  $i = 1, \dots, k$ ,  $1 < k \leq p$ , then a single Component-Wise Hastings transition updates  $x^t$  by sampling a new value for  $x_i$  from  $\pi(x_i | x_{(i)}^t)$ . To complete an entire Component-Wise Hastings transition from a state  $x^t$  to  $x^{t+1}$  we need to pick new values for each component in turn, given the values for

the others. We remand to the literature for a detailed discussion about the acceptance probability of a new state  $x_i$  to be updated (Levine et al., 2005).

The basic operation used in the Component-Wise Hastings sampling algorithm is the generation of a random value for some component of the state,  $x_l$ , from its conditional distribution given the current values of all other components,  $x_{(l)}$ . The speed of the algorithm depends crucially on whether this operation can be done quickly. The conditional distribution  $\pi(x_l | x_{(l)})$  can be expressed through a probability density function  $f = f(x_l, \mathbf{C}_{l,(l)})$ , i.e. with expectation value  $x_l$  and covariance  $\mathbf{C}_{l,(l)}$ , being  $\mathbf{C}$  given by:

$$\mathbf{C} = \begin{pmatrix} \sigma_1^2 & \rho_{1,2} \sigma_1 \sigma_2 & \dots & \rho_{1,p} \sigma_1 \sigma_p \\ \rho_{2,1} \sigma_2 \sigma_1 & \sigma_2^2 & \dots & \rho_{2,p} \sigma_2 \sigma_p \\ \vdots & \vdots & \ddots & \vdots \\ \rho_{p,1} \sigma_p \sigma_1 & \rho_{p,2} \sigma_p \sigma_2 & \dots & \sigma_p^2 \end{pmatrix}, \quad (5.11)$$

where  $\sigma_l^2$  the variance associated with  $x_l$ ,  $\rho_{i,j}$  the coefficient of linear correlation between  $x_i$  and  $x_j$ . So the usual approach is to simply calculate the joint probabilities  $f(x_l, \mathbf{C}_{l,(l)})$  of all the states in which  $x_l$  takes on its various possible values, while the other  $x_{(l)}$  remain fixed at their current values. The function  $f(x_l, \mathbf{C}_{l,(l)})$  can be used to construct a proposal probability density function in the Component-Wise Hastings sampler. In Appendix B.1 we present a general method to generate  $p$  correlated random numbers which enter in  $f(x_l, \mathbf{C}_{l,(l)})$ .

### Annealing schedule

Looking at Eq. (5.5) we see that in the Bayesian framework the chain  $x^t$  should converge to the posterior probability, starting from the prior, when the system will reach the equilibrium. Unfortunately, the states of  $x^t$  can be regarded as samples from the stationary distribution given by the posterior only after some initial *burn-in* period required for the chain to reach equilibrium.

Here we consider an approach, defined *annealing*, which allows us to i) define the length of the burn-in period; ii) evaluate the Bayesian evidence; iii) sample larger regions of the posterior to better estimate the parameters. The general idea is to use the same MCMC sampling in the burn-in period to evaluate the evidence, without adding further computational costs. In this framework we work with a modified likelihood  $P^\lambda(\mathbf{D}|\boldsymbol{\theta}, \mathcal{H}_i)$ , being  $\lambda$  a numerical coefficient. Setting  $\lambda = 0$  switches the likelihood off ( $P^0(\mathbf{D}|\boldsymbol{\theta}, \mathcal{H}_i) = 1$ ), so the modified posterior is just the prior. Setting  $\lambda = 1$  switches the likelihood on ( $P^\lambda(\mathbf{D}|\boldsymbol{\theta}, \mathcal{H}_i) = \text{likelihood}$ ), so the modified posterior is simply the true posterior. Increasing  $\lambda$  mildly from 0 to 1 according to some annealing schedule, we can construct a set of finite steps between:

$$\begin{array}{ccc} \text{prior} & \longrightarrow & \text{posterior} \\ \lambda = 0 & & \lambda = 1 \end{array} \quad (5.12)$$

So this allows the chain to sample from remote regions of the posterior distribution and to arrange for the end of the burn-in period to coincide with the point at which  $\lambda$  reaches unity.

Here we present an updated version of the annealing schedule proposed by Geman & Geman (1990):

$$\underbrace{t_1, \dots, t_m}_{\Delta t^1}, \underbrace{t_{m+1}, \dots, t_{2m}}_{\Delta t^2}, \dots, \underbrace{t_{n-m+1}, \dots, t_n}_{\Delta t^p} \quad (5.13)$$

$$\lambda(\Delta t^1) \quad \lambda(\Delta t^2) \quad \lambda(\Delta t^p)$$

being  $t_i$  the generic time at which the state  $x^i$  refers, and  $\Delta t^j = t_{k+m-1} - t_k$  the generic interval of time at which it is associated the transition from the initial state  $x^k$  at  $t = t_k$  to the final one  $x^{k+m-1}$  at  $t = t_{k+m-1}$ . In particular for  $\lambda(t)$  we consider the following schedule:

$$\lambda(\Delta t) = \begin{cases} \propto \log(\Delta t), & \lambda(\Delta t) \in [0, 1] & \text{for } \Delta t \leq t^* \\ 1 & & \text{for } \Delta t > t^* \end{cases} \quad (5.14)$$

where with  $t^*$  we have indicated the length of the burn-in period.

We define the transitions involving a change of state from  $x^t$  to  $x^{t+m-1}$ , with  $x^t$  and  $x^{t+m-1} \in \Delta t^s$ , as *minor chains*, the ones involving a change of state from  $x^k$  to  $x^{k+1}$  belonging to contiguous intervals of time  $\Delta t^i$  and  $\Delta t^{i+1}$ , as *major chains*. So we can think a MCMC algorithm as a succession of finite steps, the major chains, with a *non-stationary distribution* from the prior to the posterior (Eq. 5.12), while an intermediate transition, a minor chain, is characterized by the same value of  $\lambda(\Delta t)$ , i.e. for a sufficient number of iterations  $m$  ( $m \sim 10^3$ ) it tends to have a *stationary distribution* intermediate between the distribution of prior and the posterior depending on the value of  $\lambda(\Delta t)$ .

### The RJMCMC algorithm

In the classical Bayesian framework we assume particular models to fit the data, and to perform the two level of inference described in Sect. 5.3.1. In this picture every model  $\mathcal{H}_i \in \mathbb{R}^p$  is known a priori, and obviously it is known its dimensionality  $p$  as well. Sometime it is necessary to specify a model in such a way that the number of parameters  $p$  of the model is, in itself, a parameter: so we would like to infer  $\mathcal{H}' = (\mathcal{H}, p) \in \mathbb{R}^p \times \{p\}$ . Green (1995) proposed a general framework, known as the reversible jump MCMC (RJMCMC) method, to solve the above problem. The general idea is to propose a new model  $\mathcal{H}'$ , described at a given time  $t$  by a state  $(x^t, p) = (x_1^t, x_2^t, \dots, x_p^t, p) \in \mathbb{R}^p \times \{p\}$ , by attempting steps between state spaces of different dimensionality, say, from  $(x^t, p)$  to  $(y^t, r) \in \mathbb{R}^r \times \{r\}$ . If the model  $(\mathcal{H}, r)$  at time  $t$  is proposed, a reversible move has to be considered in order to preserve the detailed balance equations of the Markov chain. This transition is implemented by drawing a vector of continuous random variables  $u$ , independent of  $x^t$  and with proposal distribution  $q(u)$ , and setting the new state  $(y^t, r) = d((x^t, p), u)$ , where  $d$  is an invertible and deterministic function.

Here we consider just the so called *Birth-and-death transitions*, where we just increase or decrease the number of parameters by one parameter  $x_r^t$ ,  $r \in \{p-1, p+1\}$ . For the above deterministic transformation we have:  $u = x_{p+1}^t$ ,  $d := (x_1^t, x_2^t, \dots, x_p^t, p) \rightarrow (x_1^t, x_2^t, \dots, x_p^t, x_{p+1}^t, p+1)$ ,  $y = (x_1^t, x_2^t, \dots, x_p^t, x_{p+1}^t)$  and  $r = p+1$  for the birth transition. Similar considerations hold for the death transition. It is possible to show (see Umstätter

et al., 2005) that the acceptance probability for the birth transition is:

$$\alpha_{birth} = \min \left\{ 1, \frac{P(p+1)P(x_{p+1}|\mathcal{H})P(\mathbf{D}|y, p+1, \mathcal{H})}{P(p)P(\mathbf{D}|x, p, \mathcal{H})q(u)} \right\} \quad (5.15)$$

and that for the death transition is:

$$\alpha_{death} = \min \left\{ 1, \frac{P(p)P(\mathbf{D}|x, p, \mathcal{H})q(u)}{P(p-1)P(x_{p-1}|\mathcal{H})P(\mathbf{D}|y, p-1, \mathcal{H})} \right\} \quad (5.16)$$

being  $P(p)$  our prior on the number of components: we set  $P(p) = P(r)$ .

We use a normal proposal distribution  $N(0, \sigma^2)$  for  $q(u)$ . To determine the values for  $\sigma^2$  we set  $\sigma^2$  roughly equal to the noise level of the current status  $y$ . Transitions characterized by tighter proposal distribution would have a negligible effect on the likelihood but they would be more easily rejected (accepted) due the higher values of the proposal distribution for birth (death) transitions; on the other hand, a larger proposal distribution would be still likely rejected because the larger areas of the allowed parameter space with low values of the likelihood.

We use a uniform proposal distribution  $\mathcal{U}(0, \sigma'^2)$  for the prior  $P(x_r|\mathcal{H})$ , with  $\sigma'^2$  suitable value of the allowed range of  $x_r$ .

An advantage of the RJMCMC over other evidence-based stopping criteria, i.e. for determining the number of signals they consider the value of the Bayesian factor  $K = P(\mathbf{D}|\mathcal{H}, p+1)/P(\mathbf{D}|\mathcal{H}, p)$  (see Eq. 5.9), is that the RJMCMC does not require any evidence calculation, which is computationally very expensive. Moreover, a further interesting possibility is to describe a physical phenomenon in a *non-parametric way*: for example, for the Fourier theorem we can describe a signal as sum of sinusoidal functions, being the amplitudes, frequencies and the total number of sinusoids the parameters to be estimated through a RJMCMC method.

We observe that the RJMCMC method provides a general framework, encompassing other algorithms. For example, when we consider only subspaces of the same dimension, the RJMCMC algorithm reduces to the Metropolis-Hastings algorithm.

## 5.4 The dataset and analysis

We have considered 6 objects (A2204, A2163, A85, A401, A478, A1651) at intermediate redshift ( $z \sim 0.1 - 0.2$ ) for which we have X-ray data coming from the Chandra archive and SZ ones from the Cosmic Background Imager (CBI). For four of these sources (A85, A401, A478, A1651) we also have the density profiles coming from the *ROSAT* archive. From the images of the ROSAT Position Sensitive Proportional Counter (PSPC) we have recovered the density profiles by deprojecting the counts in the 0.4 – 2.4 keV band. An advantage of introducing ROSAT data is to have brightness profiles, and so density profiles, sampled up to large radii ( $\sim 0.7 R_{200}$ ), much larger than the region mapped by Chandra ( $\lesssim 1/3 - 1/2 R_{200}$ ); a disadvantage to deal with ROSAT data is that, unlike Chandra, it is not possible to recover temperature profiles.

Details of the X-ray analysis can be found in Chapter 2. Here we approach this problem from a new direction, where we have also SZ data, which can provide further constraints on the physical parameters in the outskirts of galaxy clusters, by considering Bayesian inference through X-ray and SZ data instead of a  $\chi^2$  statistic just on X-ray data, and by implementing a MCMC to determine the distribution of the best-fit parameters, instead of a grid in the space of the parameters.

As we have seen in Sect. 5.3.1, to perform the two level of inference we are interested on we need the unnormalized Bayesian posterior  $\bar{P}(\boldsymbol{\theta}|\mathbf{D}, \mathcal{H}_i)$ . The general idea of the method we have developed is to start just by considering X-ray data, so as to have a first estimate of the parameters concerning the DM profile, which the X-ray data can provide thanks to their good quality, and then to perform a joint X-ray+SZ analysis in the likelihood, as shown below:

$$\text{Unnormalised Posterior} = \underbrace{\text{Likelihood}}_{\text{joint X-ray+SZ}} \times \underbrace{\text{Prior}}_{\text{just X-ray}} \quad (5.17)$$

to recover the unnormalized posterior which can provide the two above levels of inference.

#### 5.4.1 The prior: a X-ray analysis only

For details on the X-ray data reduction we remand to Chapter 2. Here, we remind the main characteristics of the X-ray analysis only adopted to recover the radial distribution of the ICM and the DM investigated in the present Chapter, while in Sect. 5.4.2 we present a full description of the combined X-ray and SZ analysis.

Assuming a spherically symmetric emission, (i) the electron density  $n_e(r)$  is recovered both by deprojecting the surface brightness profile and the spatially resolved spectral analysis obtaining a few tens (the total number of radial bins is between 24 and 239) of radial measurements; (ii) once a functional form of the DM density profile  $\rho = \rho(\mathbf{r}, \mathbf{q})$ , where  $\mathbf{q} = (q_1, q_2, \dots, q_h)$  are free parameters of the DM analytical model, and the gas pressure  $P_0$  at  $R_{\text{spec}}$  are assumed, the deprojected gas temperature,  $T(\mathbf{q}, P_0)$ , is obtained by integration of the hydrostatic equilibrium equation:

$$P(r, \mathbf{q}, P_0) = P_0 - \int_{R_{\text{spec}}}^r n_{\text{gas}}(s) \mu m_H \frac{G M_{\text{tot}}(\mathbf{q}, s)}{s^2} ds, \quad (5.18)$$

where  $\mu = 0.6$  is the average molecular weight,  $m_H$  is the proton mass,  $M_{\text{tot}}(\mathbf{q}, r)$  is given by:

$$M_{\text{tot}}(\mathbf{q}, r) = M_{\text{DM}}(\mathbf{q}, r) + M_{\text{gas}}(r, \mathcal{S}_{n_e}) \quad (5.19)$$

and the gas pressure  $P_0$  at  $R_{\text{spec}}$  is left as free parameter. So  $T(\mathbf{q}, P_0) = P(\mathbf{q}, P_0)/n_{\text{gas}}$  expressed in keV units. The gas mass has been calculated from the deprojected gas density up to  $R_{\text{spec}}$ , while beyond  $R_{\text{spec}}$  we have assumed an analytical model (see Morandi et al., 2007, for further details): the vector  $\mathcal{S}_{n_e}$  represents its best fit parameters.

To constrain the 3 free parameters  $\mathcal{P} = (\mathbf{q}, P_0)$  by assuming a NFW model for the DM (Navarro et al., 1997), we have proceeded to maximize the likelihood (Eq. 5.20) through a

MCMC method, by comparing the observed temperature profile  $T_{\text{proj},m}^*$  in a lower number  $n^*$  of bins (with  $n^* \sim 4 - 10$ ) with the projection of  $T_j(\mathbf{q}, P_0)$ ,  $T_{\text{proj},m}(\mathbf{q}, P_0)$ , by applying the spectroscopic-like temperature definition (Mazzotta et al., 2004):

$$\mathcal{L}_x^* = \frac{\exp\{-\chi^2/2\}}{(2\pi)^{n^*/2}(\sigma_1 \sigma_2 \dots \sigma_{n^*})}, \quad (5.20)$$

with  $\chi^2$  equal to:

$$\chi^2 = \sum_{m=1}^{n^*} \frac{(T_{\text{proj},m}(\mathbf{q}, P_0) - T_{\text{proj},m}^*)^2}{\sigma_{T_{\text{proj},m}}^2} \quad (5.21)$$

So we can determine some physical parameter of the cluster,  $T_j = T_j(\mathbf{q}, P_0)$  and  $P_j = P_j(\mathbf{q}, P_0)$  till  $R_{\text{spec}}$ , and  $M(< R_\Delta) = M(\mathbf{q})(< R_\Delta)$ , just by relying on the spherical geometry assumption, on the hydrostatic equilibrium equation and on robust results of the numerical simulations on the DM profiles.

In particular, just through a X-ray analysis only we can have a first estimate of the marginal distribution of  $\mathbf{q}$  given the parameters  $\mathcal{P} = (\mathbf{q}, P_0)$ , which we can use to put constraints through the Bayesian prior on the parameters of our DM models.

We observe, however, at this point we still have a strong degeneracy of  $\mathcal{P} = (\mathbf{q}, P_0)$ , due to the small dimension of the observed X-ray region ( $R_{\text{spec}} \sim 1/3 - 1/2 R_{200}$ ).

#### 5.4.2 The likelihood: a joint X-ray+SZ analysis

The SZ effect and the X-ray emission both depend on the properties of the hot cluster plasma, because the electrons of the cosmic baryons are responsible both of the X-ray emission and the SZ effect. In this sense we construct the likelihood performing a joint analysis for SZ and X-ray data, that describes all the relevant spatial and spectral characteristics in the image domain, and spatial characteristics in the Fourier one, to constrain the properties of the physical parameters of the ICM and of the underlying DM density profile.

We use the estimate of  $(\mathbf{q}, P_0)$  in the Bayesian prior as proposal distribution to start a new MCMC simulation and to jump from the same prior to the posterior, where we account for the SZ data: this makes the calculation faster, because the X-ray data alone can constrain  $(\mathbf{q}, P_0)$ .

The method works by constructing a joint X-ray+SZ likelihood:

$$\mathcal{L} = \mathcal{L}_x \cdot \mathcal{L}_{\text{SZ}} \quad (5.22)$$

being  $\mathcal{L}_x$  and  $\mathcal{L}_{\text{SZ}}$  the likelihoods coming from the X-ray and SZ data, respectively (see below).

We observe that a X-ray analysis only can determine the density till  $R_{\text{spec}}$ . SZ data can, in principle, constrain the pressure beyond  $R_{\text{spec}}$ , being the field of view of CBI better than that one of Chandra. Anyway we point out that if we add the hydrostatic equilibrium hypothesis, assumed an analytical model for the DM, and some parameterization for the density in the outskirts, we are able to measure both the density and the temperature

beyond  $R_{\text{spec}}$ . We remand to Sect. 5.4.3 for a detailed description of the parameterization of the density in the outskirts.

Assuming a NFW model for the DM (Navarro et al., 1997), we apply the hydrostatic equilibrium equation:

$$P(r, \mathbf{q}, P_{\text{SZ}}) = P_{\text{SZ}} - \int_{R_{\text{SZ}}}^r n_{\text{gas}}(s) \mu m_H \frac{G M_{\text{tot}}(\mathbf{q}, s)}{s^2} ds, \quad (5.23)$$

being  $P_{\text{SZ}}$  (this is a free parameter) and  $R_{\text{SZ}}$  the pressure and the linear size of the SZ boundary, respectively;  $M_{\text{tot}}(\mathbf{q}, r)$  is given by Eq. (5.19), with  $\mathcal{S}_{n_e}$  equal to the parameters of the density in the outskirts (Sect. 5.4.3).

So we have the density  $n_{\text{gas},i}(\mathcal{S}_{n_e})$ , temperature  $T_j(\mathbf{q}, P_{\text{SZ}}, \mathcal{S}_{n_e})$  and therefore pressure profile  $P_j(\mathbf{q}, P_{\text{SZ}}, \mathcal{S}_{n_e})$  for the  $i$ -th MCMC step up to  $R_{\text{SZ}}$ . The proposed sample of the parameters becomes  $\mathcal{P} = (\mathbf{q}, P_{\text{SZ}}, \varepsilon, \mathcal{S}_{n_e})$ , where  $\varepsilon$  is a factor of the order of unity which accounts for wrong assumptions on the cosmological model or on the geometry of the cluster in the determination of the theoretical parameters (see Sect. 5.4.4).

By projecting the pressure profile (Eq. 5.23) we obtain the theoretical Compton parameter  $y = y(\vec{\mathcal{P}}, \varphi)$  (Eq. 5.1); by performing its  $\mathcal{HT}$  (Eq. 5.2) and using Eq. (2.22) we obtain the theoretical visibility  $\tilde{V}((\mathbf{q}, P_{\text{SZ}}, \mathcal{S}_{n_e}), u)$ . We define a corrected theoretical visibility  $V(\mathcal{P}, u) = \varepsilon \tilde{V}((\mathbf{q}, P_{\text{SZ}}, \mathcal{S}_{n_e}), u)$ .

So  $\mathcal{L}_{\text{SZ}}$  becomes:

$$\mathcal{L}_{\text{SZ}} = \frac{\exp\left\{-\frac{1}{2}[(V_m(\mathcal{P}) - V_m^*)]^t \mathbf{C}'^{-1} [(V_m(\mathcal{P}) - V_m^*)]\right\}}{(2\pi)^{m^*/2} |\mathbf{C}'|^{1/2}}, \quad (5.24)$$

where  $\mathbf{C}'$  is the covariance matrix referred to the SZ data (it has an expression similar to Eq. (5.11), but it refers to SZ measurements),  $V_m^*$  is the  $m$ -th observed visibility,  $V_m(\mathcal{P})$  the theoretical one,  $m^*$  the total number of visibilities.

For  $\mathcal{L}_x$  holds an expression similar to Eq. (5.20), with  $\chi^2$  given by:

$$\chi^2 = \sum_{m=1}^{n^*} \frac{(T_{\text{proj},m}(\mathbf{q}, P_{\text{SZ}}, \mathcal{S}_{n_e}) - T_{\text{proj},m}^*)^2}{\sigma_{T_{\text{proj},m}}^2} \quad (5.25)$$

being  $T_{\text{proj},m}(\mathbf{q}, P_{\text{SZ}}, \mathcal{S}_{n_e})$  the convenient projection of  $T_j(\mathbf{q}, P_{\text{SZ}}, \mathcal{S}_{n_e})$ .

So we can think the parameter vector  $\mathcal{P} = (\mathbf{q}, P_{\text{SZ}}, \varepsilon, \mathcal{S}_{n_e})$  in this way:

$$\mathcal{P} = \begin{cases} \text{gas properties in the outskirts} & P_{\text{SZ}}, \mathcal{S}_{n_e} \\ \text{dark matter density} & \mathbf{q} \\ \text{geometry/cosmology} & \varepsilon \end{cases} \quad (5.26)$$

We start by considering the gas properties in the outskirts, and then we will explore the constraints on the DM, and at last the possibility of determining the cluster geometry and cosmological parameters.

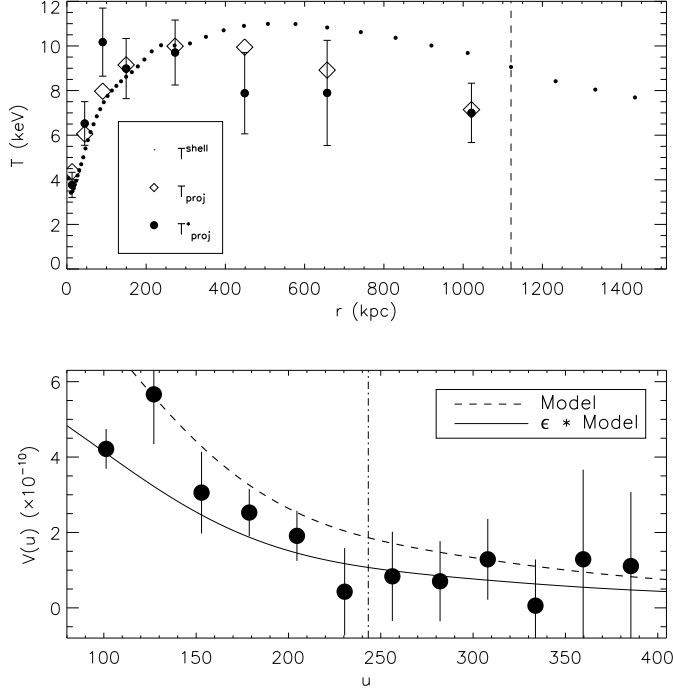


**Figure 5.2.** Example of joint X-ray and SZ analysis (Eq. 5.22). In the upper panel we display the two quantities which enter in the Eq. (5.25) in the spectral deprojection analysis to retrieve the physical parameters: the observed spectral projected temperature  $T_{\text{proj},m}^*$  (big circles with errorbars) and the theoretical projected temperature  $T_{\text{proj},m}(\mathbf{q}, P_{\text{SZ}}, S_{n_e})$  (triangles). We also show the theoretical deprojected temperature  $T_j(\mathbf{q}, P_{\text{SZ}}, S_{n_e})$  (points), which generates  $T_{\text{proj},m}(\mathbf{q}, P_{\text{SZ}}, S_{n_e})$  through convenient projection techniques. The dashed vertical line represents the X-ray boundary. In the lower panel we display the two quantities which enter in the Eq. (5.24): the observed visibilities  $V_m^*$  (big points with errorbars) and the theoretical one  $V_m(P)$  (solid line). The dashed line refers to  $\tilde{V}((\mathbf{q}, P_{\text{SZ}}, S_{n_e}), u)$ . The dot-dashed vertical line refers to the above X-ray boundary in the Fourier domain.

### 5.4.3 Gas properties in the outskirts

As seen in the previous section, an X-ray analysis can determine the density only out to  $R_{\text{spec}}$ . By accounting SZ data we can improve our information of the cluster by studying regions out to  $R_{200}$ . To measure the density in the outskirts we observe that we can always define an exponent  $\alpha(r)$ ,  $\alpha(r) \equiv -d \ln n_{\text{gas}}(r) / d \ln r$ : the general idea is to recover  $\alpha(r)$  as series expansion, i.e.

$$\alpha(r) = \alpha_0 + \alpha_1 z + \alpha_2 z^2 + \dots + \alpha_h z^h, \quad (5.27)$$

with  $z = (r - R_{\text{spec}}) / R_{\text{spec}}$ ,  $\alpha_0 = \alpha(R_{\text{spec}})$  and under the condition  $d \ln \alpha(r) / d \ln r \geq 0$  and being  $h$  the unknown number of components. We point out that the density has a power-law behaviour in the external regions, with  $\alpha(r)$  mildly increasing with the radius ( $\alpha(r) \approx 1.5 - 3$  for  $r \gtrsim R_{\text{spec}}$ ), so we can likely recover it with a few terms of the above series expansion. So the problem is to recover  $(\alpha_0, \alpha_1, \dots, \alpha_h, h)$ : a convenient approach has been presented in Sect. 5.3.2 through a reversible jump MCMC method, in particular through Birth-and-death transitions (see Sect. 5.4.5 for details on the parameter

sampling). As pointed in Sect. 5.3.2, this gives us a *non-parametric* description of the density in the outskirts, being the series expansion in Eq. (5.27) applicable to any convenient function.

So, if we indicate with  $n^{\text{Ch}}(r)$  ( $n^{\text{Ro}}(r)$ ) the measured gas density through an X-ray analysis with Chandra (ROSAT) inside  $R_{\text{spec}}^{\text{Ch}}$  ( $R_{\text{spec}}^{\text{Ro}}$ ), we can recover the density up to  $\sim R_{200}$ :

$$n_{\text{gas}}(r) = \begin{cases} n^{\text{Ch}}(r) & r \leq R_{\text{spec}}^{\text{Ch}} \\ n^{\text{Ro}}(r) & R_{\text{spec}}^{\text{Ch}} \leq r \leq R_{\text{spec}}^{\text{Ro}} \\ n(R_{\text{spec}}^{\text{Ro}}) \left(\frac{r}{R_{\text{spec}}^{\text{Ro}}}\right)^{-\alpha(r)} & r > R_{\text{spec}}^{\text{Ro}} \end{cases} \quad (5.28)$$

with always  $R_{\text{spec}}^{\text{Ch}} \sim 1/3 - 1/2 R_{200} \lesssim R_{\text{spec}}^{\text{Ro}} \sim 0.7 R_{200}$ . For the two sources A2204 and A2163, for which we do not have ROSAT data, we describe the density beyond  $R_{\text{spec}}^{\text{Ch}}$  just through the above RJMCMC method.

#### 5.4.4 Constraints on the cosmology/geometry

Another interesting key point is the introduction of the parameter  $\varepsilon$ . We assume that the observed Compton parameter  $q = q(r)$  and the theoretical one  $p = p(r)$  are related by the following expression:

$$q = \varepsilon p = (\varepsilon_{\text{str}} + \varepsilon_{\text{cosm}}) p . \quad (5.29)$$

being  $\varepsilon_{\text{str}}$  the uncertainty due to a wrong assumption about the geometry,  $\varepsilon_{\text{cosm}} = (D_{\text{true}}/D_{\text{ass}})^{1/2}$  due to the uncertainties about the cosmology entering in the assumed diameter distance  $D_{\text{ass}}$ . So the MCMC algorithm can provide us information about the geometry and the cosmology, being  $\varepsilon$  a direct output of the algorithm. In other words, if we consider a sample of clusters, we have  $\langle \varepsilon \rangle = \langle (\varepsilon_{\text{str}} + \varepsilon_{\text{cosm}}) \rangle \approx \langle \varepsilon_{\text{cosm}} \rangle$ , being the systematic errors due to the wrong geometry symmetric if we consider a complete sample of clusters; if we assume that the errors about  $\Omega$  and  $\Lambda$  are negligible compared with the one on  $H$ ,  $\varepsilon_{\text{cosm}} = h^{-1/2}$ , and therefore we can derive directly the Hubble constant like an output of the MCMC algorithm.

#### 5.4.5 The unnormalized posterior: model fitting

We start by pointing out that we used the annealing schedule presented in Sect. 5.3.2, through a sequence of minor (stationary statistical systems) and major chains (non-stationary statistical systems).

We remember that in the Component-Wise Hastings sampler (Sect. 5.3.2) we split the  $p$ -dimensional vector  $x$  into  $k \leq p$  components, so that  $x = (x_1, \dots, x_k) \in \mathbb{R}^p$ : referring to Eq. (5.26), we have  $k = 3$  (gas properties in the outskirts, dark matter density and geometry/cosmology) and  $x = \mathcal{P}$ . To complete an entire Component-Wise Hastings transition from a state  $x^t$  to  $x^{t+1}$ , a minor chain, we need to pick new values for each component group in turn, given the values for the other ones. Given the strong correlation between the above 3 parameter groups, in particular between gas density and DM density, the Component-Wise Hastings sampler is a very robust means to sample the space

parameters breaking the degeneracy between them. An intuitive way to understand this is to point out that the gas density and the DM density, for example, are strictly correlated: the more the DM density is higher in the external regions, the more the gas density must be lower in the outskirts. At the  $i$ -th MCMC transition the conditional distribution of  $\mathcal{P}$ ,  $\pi(\mathbf{q} \mid \boldsymbol{\varepsilon}, \mathcal{S}_{n_e}, P_{sz})$ , involving an update of  $\mathbf{q}$  but with  $(\mathcal{S}_{n_e}, \boldsymbol{\varepsilon}, P_{sz})$  fixed, retains also the information coming from the density in the external regions, better determining the mass profiles, and so on.

Concerning the parameter group of the gas density ( $\mathcal{S}_{n_e}$ ), as already said we use a RJMCMC method, which can be thought just as a more general approach of the Component-Wise Hastings transition involving  $\mathcal{S}_{n_e}$ . For every major chain (Sect. 5.3.2) we attempt a birth and a death transition, updating the dimensionality of  $\mathcal{S}_{n_e} = (\alpha_0, \alpha_1, \dots, \alpha_h, h)$ , while for every minor chain we consider only subspaces of the same dimension, i.e. the RJMCMC algorithm reduces to the above Component-Wise Hastings transition involving  $\mathcal{S}_{n_e}$  with conditional distribution  $\pi(\mathcal{S}_{n_e}, P_{sz} \mid \boldsymbol{\varepsilon}, \mathbf{q})$ .

The above MCMC simulation was implemented on an Intel Pentium IV 3 GHz processor. In 10 min of CPU time the posterior distribution can be evaluated  $\sim 10^4$  times. The total analysis requires  $\sim 2$  hrs of CPU time for each of the sources.

## 5.5 Application to mock clusters

To test our method we apply our Bayesian X-ray+SZ method on mock observations. The fake clusters are constructed by considering the density profiles from real objects out to  $R_{\text{spec}}^{\text{Ro}}$  ( $R_{\text{spec}}^{\text{Ch}}$ ) and adding an analytical model in the outskirts, which aims to mimic the density profiles coming from hydrodynamical simulations (Roncarelli et al., 2006). The deprojected temperature has been recovered by considering a NFW model of parameters  $(c, r_s)$  fixed and applying the hydrostatic equilibrium equation. The so recovered temperature has been projected to simulate a real observed projected temperature profiles  $T_{\text{proj},m}^*$ . The recovered mock pressure profile has been also used to recover fake visibilities. The errors on the fake temperature and visibilities have been determined in such a way to reproduce the ones of real data. We present results of the above method in Figure 5.5 by simulating data which mimic the source A2204, by using a double power law to model the density in the outskirts, whose parameters have been set in order to reproduce the results of Roncarelli et al. (2006).

As we can see, we found a good agreement between the parameters given in input and the outputs of our program. In particular, given a double power-law model in input for the density in the outskirts, the program is able reproduce this model through 2-3 components via the RJMCMC method.

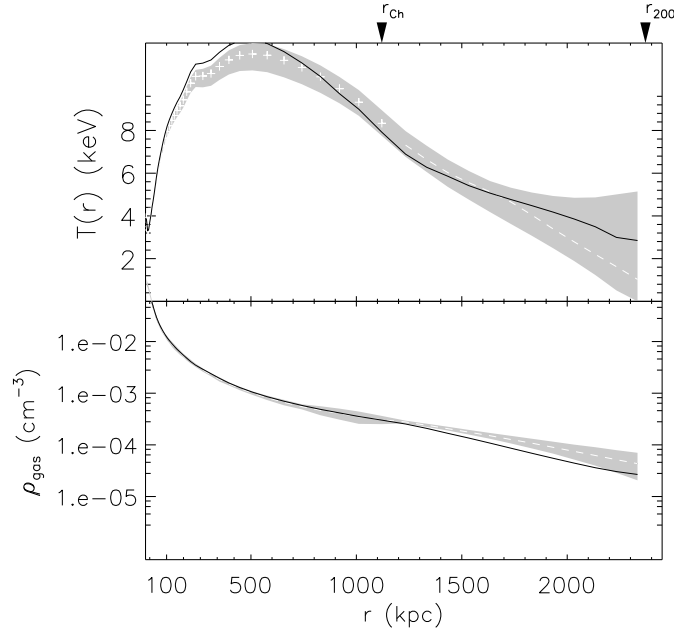


**Figure 5.3.** Comparison between the properties recovered by applying our Bayesian X-ray+SZ analysis on mock observations produced so as to mimic the physical properties of A2204. We present density (lower panel) and temperature (upper panel) profiles for mock data, which are represented by circles (out to  $R_{\text{spec}}$ ) and dashed line (for  $r \gtrsim R_{\text{spec}}$ ). The solid line refers to the values recover through our method, whose errors are represented by the gray shaded region.

## 5.6 Results on the properties of the ICM

### 5.6.1 Recovering the physical properties: prior versus posterior comparison

Here we focus on the differences in the determination of the physical properties recovered by applying an X-ray analysis only and a Bayesian X-ray+SZ one.

In Figure 5.4 (left panel) we present a comparison between the temperature measured by applying an X-ray analysis only (the prior)  $T(\mathbf{q}, P_0)$  (see Sect. 5.4.1), through a Bayesian X-ray+SZ one (the posterior distribution)  $T_j(\mathbf{q}, P_{\text{sz}}, S_{n_e})$  (Sect. 5.4.2), and the deprojected temperature recovered by the standard deprojection techniques  $T_{\text{deproj,m}}^*$  (see Morandi et al., 2007) for A2204. We have chosen A2204 because it is one of the sources for which we are able to measure the physical properties through X-ray Chandra data just out to  $\sim 0.5R_{200}$ : this object, being at intermediate redshift ( $z = 0.152$ ), does not suffer for the small field of view of Chandra, so it is an ideal case to see also, for example, the weight of the X-ray systematics in determining the temperature or mass near  $R_{\text{spec}}$  boundary (see Sect. 5.2.2).

As we can see, we have a good agreement between the three above temperatures, being the one recovered by a Bayesian X-ray+SZ analysis the temperature with the smallest

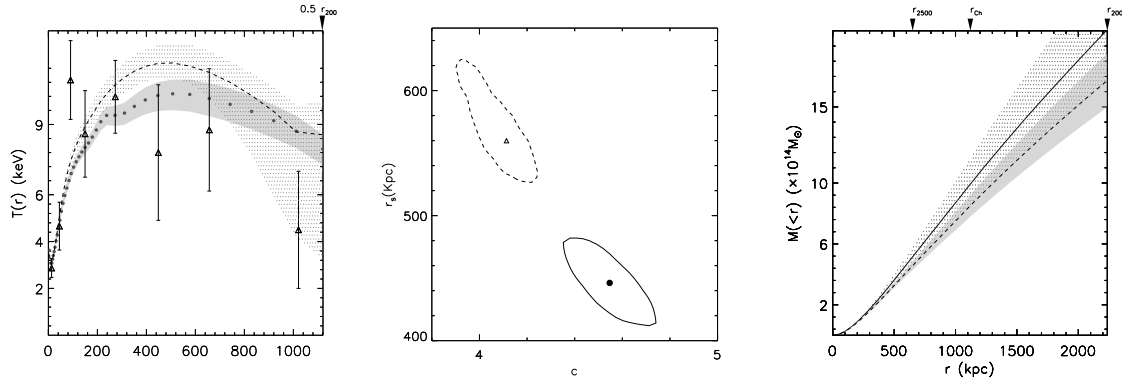


**Figure 5.4.** Left panel: comparison between the temperature measured by applying a just X-ray analysis (the prior)  $T(\mathbf{q}, P_0)$  (dashed line), through a Bayesian X-ray+SZ one (the posterior distribution)  $T_j(\mathbf{q}, P_{SZ}, \mathcal{S}_{n_e})$  (solid lines), and the deprojected temperature recovered by the standard deprojection techniques  $T_{\text{deproj},m}^*$  (triangles with errorbars). The error bands are represented by the gray shaded region for the posterior, and hatched region for the prior. Central panel: comparison between the parameters  $c$  and  $r_s$  of a NFW model for the prior and the posterior distribution. The 1- $\sigma$  contours and the average values refers to the prior (dashed line and triangle, respectively) and the posterior (solid line and point, respectively). Right panel: cumulative total mass profile of a NFW model for the prior (dashed line) and the posterior (solid line) distribution. The dashed and hatched regions hold the same meaning of the left panel.

statistical errors. Is it possible to see that  $T_j(\mathbf{q}, P_{SZ}, \mathcal{S}_{n_e})$  and  $T(\mathbf{q}, P_0)$  present a mild difference of temperature in the central regions (300-600 Kpc), due to non very good determination of the parameters  $(c, r_s)$  and to large uncertainties in the value of the pressure at the boundary  $P_0$ . Near the X-ray boundary  $R_{\text{spec}}$  the statistical errors on the prior are very large and the temperature in these regions is also possibly affected by systematics related to  $T_{\text{proj},m}^*$  near the same boundary (Eq. 5.21). In fact the last point of the deprojected temperature  $T_{\text{deproj},m}^*$  is likely affected by systematics related to a background subtraction, being the number of net counts of photons from the source in the (0.5-5.0 keV) band  $\sim 200$ -1000 and the signal-to-noise ratio is  $\gtrsim 2$  in the last annulus.

A Bayesian X-ray+SZ temperature  $T_j(\mathbf{q}, P_{SZ}, \mathcal{S}_{n_e})$  overcomes this problem, because in a SZ interferometric dataset we must not subtract any background, being the thermal noise equal to  $0 \pm \sigma_{SZ}$ , i.e. with mean value equal to zero (see Sect. 5.2.2). The statistical errors we have in  $T_j(\mathbf{q}, P_{SZ}, \mathcal{S}_{n_e})$  are also the smallest ones, especially near the X-ray boundary.

In Figure 5.4 (central and right panel) we present a comparison between the parameters  $c$  and  $r_s$  (central panel) and the cumulative total mass profile (right panel) of a NFW model for the prior and the posterior distribution. As we can see, the 1- $\sigma$  contours are systematically different ( $\sim 2\sigma$ ) between the prior and the posterior: this leads to systematics in the mass profiles which are significant for  $r \gtrsim R_{2500}$ . In other words, we can trust the mass reconstructed through a X-ray analysis only just till  $R_{2500} \sim 1/4 R_{200}$ , given that the X-ray measurements are out to  $R_{\text{spec}} \sim 1.5 R_{2500}$  and they are possibly affected by systematics near the X-ray boundary  $R_{\text{spec}}$  due to inaccurate background subtraction. For  $M_{\text{tot}}(<r)$  in the posterior distribution, we can see also lower statistical errors for  $r \gtrsim R_{2500}$ .

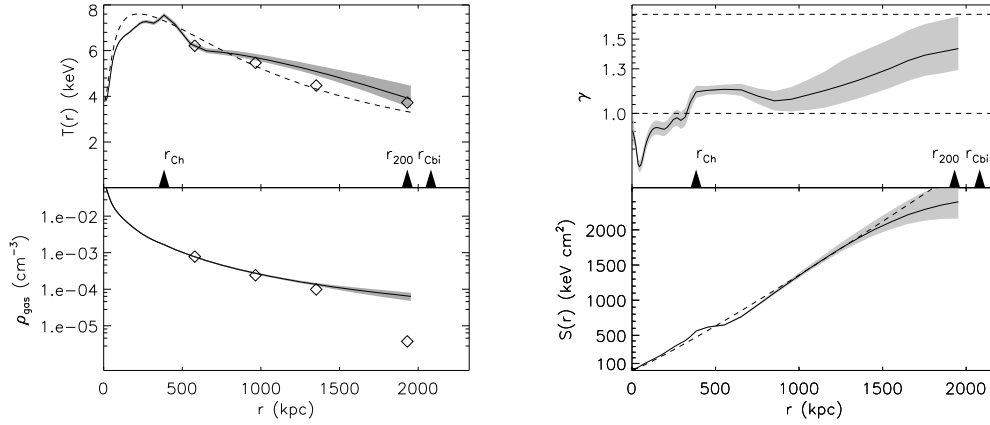


**Figure 5.5.** Results of a Bayesian X-ray and SZ analysis for A478. Figure on the right: we display the gas temperature (upper panel) and gas density (lower panel) recovered by combining X-ray and SZ data. The solid line represents the expectation value of the temperature (density), while the error bands at  $1\text{-}\sigma$  are represented by the gray shaded region. The diamonds represent the predictions from Roncarelli et al. (2006) from hydrodynamical numerical simulations, while the dashed line in the upper panel indicates the functional form that reproduces the behaviour of the deprojected X-ray temperature profile of the sources presented in Vikhlinin et al. (2006). Figure on the left: polytropic index  $\gamma$  (upper panel) and entropy profiles  $S$  (lower panel) for A478 recovered by combining X-ray and SZ data. The solid line represents the expectation value for  $\gamma(S)$ , while the error bands at  $1\text{-}\sigma$  are represented by the gray shaded region. In the upper panel the two horizontal dashed lines represent the value  $\gamma = 1$  and  $\gamma = 5/3$ , while in the lower panel the dashed line represents the predictions of Voit et al. (2005b), where the entropy is defined as  $S(r) = K_{200} 1.32(r/r_{200})^{1.1}$ , being  $K_{200}$  a characteristic value of the entropy at the overdensity of 200 (see, e.g., Eq. 2 in Voit et al., 2005b). For all the figures the arrows at the top represent the Chandra ( $r_{\text{Ch}}$ ), CBI ( $r_{\text{Cbi}}$ ) boundary, respectively, and  $r_{200}$ .

### 5.6.2 Physical properties in the outskirts

In this section we present results on the properties of the ICM up to the virial radius and beyond, in the radial range well above the central regions accessible to X-ray observations. In particular we compare our findings with the results of hydrodynamical numerical simulations for the density and temperature profiles (left panel of Figure 5.5). Here we will concentrate on the physical parameters recovered by using a NFW model.

For the gas density we observe a mildly flatter behaviour in regions ( $\gtrsim R_{500}$ ) than the predictions of Roncarelli et al. (2006) by re-normalizing their profiles to ours at  $0.3R_{200}$ , with a slope between  $R_{500} - R_{200}$  of  $1.8 - 2.5$ .

Concerning the temperature, we observe a good agreement of our measurements with the theoretical predictions, with a drop of a factor of 2 from the maximum value of the same temperature profile to  $R_{200}$ , where  $T(r_{200}) \approx 3$  keV.

The most pronounced deviation is at  $R_{200}$ , where simulations predict a density which is lower than the observed one. A possible explanation of this disagreement at  $R_{200}$  is that in the above simulation Roncarelli and collaborators masked out condensed regions in the simulation volume (see their work for further details on the adopted criterion), being they interested in a comparison with X-ray observations, where these small clumps are generally masked out. On the contrary, in SZ data it is not possible to mask these dense

regions, being the SZ observations in the Fourier domain. This could lead to lower values for the density at  $R_{200}$  in simulations compared to real X-ray+SZ data.

For what concerns the temperature profile, a comparison can be done also with the functional form that reproduces the behaviour of the deprojected X-ray temperature profile at  $r \gtrsim 0.05R_{200}$  of the sources presented in Vikhlinin et al. (2006, see their equation 9):

$$T(d) \propto \frac{(d/0.045)^{1.9} + 0.45}{(d/0.045)^{1.9} + 1} \frac{1}{(1 + (d/0.6)^2)^{0.45}}, \quad (5.30)$$

where  $d \equiv r/R_{500}$ . We overplot this function fitted on the values of the spectral deprojected temperature to our profiles in Fig. 5.5. We still observe a steeper behaviour than the above functional form for  $r \gtrsim 0.4R_{200}$ . A possible explanation of this disagreement is that this function is determined in the local sample of sources of Vikhlinin et al. (2006), where the X-ray observations are limited to the central regions ( $\lesssim 0.5R_{200}$ ), likely affected by systematics related to the background subtraction near the X-ray boundary.

In Figure 5.5 (right panel) we also present entropy  $S(r)$  and polytropic index  $\gamma(r)$  profiles for A478. The polytropic index shows a very complex behaviour, far away from being constant and being always between 1 and 5/3 outside the cooling regions, as expected for a non-convective gas. For the entropy profiles it is interesting to point out that there is a flattening for  $r \gtrsim 0.7R_{200}$  and the value of  $S(r)$  is lower than the predictions for adiabatic clusters from Voit et al. (2005b) for  $r \gtrsim 0.75R_{200}$ , suggesting that our data are likely affected by dense cold regions in the outskirts, as already noticed by comparing our density with the predictions from the numerical simulations. In the spatial range  $0.4 - 0.75R_{200}$  we find a good agreement with the adiabatic predictions of Voit et al. (2005b) by considering SPH simulations through the GADGET code (Springel et al., 2001; Springel & Hernquist, 2002), where the entropy is defined as

$$S(r) = K_{200} 1.32(r/r_{200})^{1.1}, \quad (5.31)$$

being  $K_{200}$  a characteristic value of the entropy at the overdensity of 200 (see, e.g., Eq. 2 in Voit et al., 2005b). Voit and collaborators also consider the semi-analytical models by using clusters simulated by the AMR code ENZO (Bryan, 1999; Norman & Bryan, 1999; O’Shea et al., 2004): in the latter case the normalization of the above theoretical relation is  $\sim 10$  per cent higher than in the SPH simulations, in disagreement with our constraints.

## 5.7 Summary and conclusions

We have presented a Bayesian approach to combine X-ray and Sunyaev Zel’dovich (SZ) data, observed with Chandra and the Cosmic Background Imager (CBI), respectively, in order to investigate the radial behaviour of the deprojected physical cluster properties, like temperature, density, entropy, gas mass and total mass up to the virial radius. We showed that a joint X-ray and SZ analysis allows to study the physical properties of the ICM in the outskirts of the clusters out to  $R_{200}$ , well beyond the boundary ( $1/3 - 1/2$  of the virial

radius) of the present X-ray observations. This has been made possible thanks to the large field of view of CBI and the strong dependency of the interferometric SZ signal on the external regions of the clusters. In particular we discussed how it is possible to recover the physical parameters of the gas in the outskirts in a non-parametric way through a Reversible Jump Markov Chain Monte Carlo technique.

We have compared our findings with the results of hydrodynamical numerical simulations for the density and temperature profiles (e.g. Roncarelli et al., 2006) or semi-analytical models (e.g. Voit et al., 2005b). We discussed the systematics which can affect our data, the discrepancies of our results on the density, temperature and entropy profiles with respect to the theoretical predictions. In particular, the combination of the Chandra data at high spatial resolution, capable to resolve the cluster core, with the SZ ones, more sensitive to the cluster outer volume, allows to characterize the level and the gradient of the gas entropy distribution in the whole cluster, breaking the degeneracy between the physical models describing the thermal history of the ICM.



# CONCLUSIONS

In this Thesis we focused our research on the context of understanding the physics of the structures' formation in the Universe through X-ray and Sunyaev Zel'dovich observations and on the comparison of our findings with numerical simulations from the literature. We have presented our work on a sample of galaxy clusters to describe the properties of the X-ray and SZ signals, aiming at determining the physical properties of the intracluster gas.

Here we conclude the presentation of this Thesis by summarizing our main results.

## **X-ray and Sunyaev-Zel'dovich scaling relations in galaxy clusters**

SZ and X-ray scaling relations are a robust means to probe the physical properties of the clusters and their evolution in redshift, by tracing out the thermodynamical history of the intracluster medium. We have pointed out that the X-ray laws are steeper than the relations predicted from the adiabatic model: these deviations from self-similar expectations call for further feedback processes leading to non-gravitational gas heating. Our results on the X-ray and SZ scaling relations showed a tension between the quantities more related to the global energy of the system (e.g. gas temperature, gravitating mass) and the indicators of the structure of the ICM (e.g. gas density profile, central Compton parameter  $y_0$ ), showing an evolution of the physical parameters and suggesting a scenario in which the ICM at higher redshift has lower X-ray luminosity and lower pressure in the central regions than the expectations from gravitational processes only.

## **Entropy profiles in X-ray luminous galaxy clusters at $z > 0.1$**

Another tool to constrain the thermal history of the gas is the entropy distribution, which reflects both the accretion history of the gas and the processes of feedback. The entropy distributions provide hints of non-gravitational energy. We have studied the profiles and the scaling properties of the gas entropy in massive X-ray galaxy clusters at high redshift ( $0.14 \leq z \leq 0.82$ ) and showing different states of relaxation. We showed that the entropy profiles are remarkably similar outside the core and can be described by simple powerlaws, with a central plateau which spans a wide range of values ( $\sim$  a few–200 keV cm<sup>2</sup>) depending on the state of relaxation of the source. The entropy values resolved at given fraction of the virial radius are

proportional to the gas temperature in these hot systems and appear larger at higher redshift with respect to the local estimates. To characterize the energetic of the central regions, we have compared the radial behaviour of the temperature of the gas with the temperature of the dark matter ( $T_{\text{DM}}$ ), by estimating the excess of energy  $\Delta E = 3/2 k(T_{\text{gas}} - T_{\text{DM}})$ . We have found that  $\Delta E$  ranges from  $\approx 0$  in typical cooling-core clusters to few keV within 100 kpc in non-cooling core systems. Furthermore we have measured a significant correlation between the total iron mass and the entropy outside the cooling region, whereas in the inner regions they strongly anti-correlate. We have found that none of the current models in literature including non-gravitational energy is able to explain entropy, metallicity and gas+dark matter temperature profiles we have obtained. We have also checked whether hydrostatic equilibrium is a tenable hypothesis in galaxy clusters by comparing the temperature recovered through the application of the hydrostatic equilibrium equation with the spectral measurements, and by exploring the deviations observed in few non-cooling core clusters in the inner regions.

### **Bayesian inference in X-ray galaxy clusters with Sunyaev Zel'dovich measurements - Physical properties of the gas out to $R_{200}$**

We have presented a code to combine X-ray and Sunyaev Zel'dovich (SZ) data, observed with Chandra and the Cosmic Background Imager (CBI), respectively. We showed that a joint X-ray and SZ analysis allows to study the external regions of clusters well beyond the volumes resolved with X-ray observations ( $\leq R_{500}$ ), thanks to the large field of view of CBI and the strong dependence of the SZ interferometric signal on the external regions. We studied the radial behaviour of the deprojected physical cluster properties, like temperature, density, entropy, gas mass and total mass up to the virial radius, well beyond the X-ray boundary ( $1/3 - 1/2$  of the virial radius). We have investigated the density and temperature profile in the external regions, comparing our findings with results from numerical hydrodynamical simulations. We showed how it is possible to trace out the density, temperature and entropy of the gas in the outskirts and putting constraints on the non-gravitational processes which affect the thermal history of the gas.

## **Future works**

In the near future we are going to extend the above work on entropy profiles on massive clusters at high redshift, by considering local groups of galaxies. The non-gravitational energy having more pronounced influence on the intergalactic gas of groups of galaxies, we expect to find a stronger deviation from the self-similar expectations.

We are extending the line of research previously presented by combining X-ray and SZ data, focusing our research on understanding the physics of the structures' formation in the Universe. As already observed, a joint X-ray and SZ analysis allows us to study the outer regions of the clusters. In this sense one can address many different key aspects that are still debated and offer solutions to ticklish problems not yet solved. In particular our

current research aims at exploring the following topics:

**Constraints on the properties of clusters outskirts** - We are extending the sample of galaxy clusters presented in Chapter 4 by including further sources observed with the upgraded CBI2 instrument. So we will be able to investigate the radial behaviour of the deprojected physical cluster properties, like temperature, density, entropy, gas mass and total mass in the outskirts, in a larger sample and with data of better quality with respect to the CBI archival data.

**Constraints on  $f_{\text{gas}}$**  - In the last years the universal baryonic mass fraction ( $\Omega_b/\Omega_m$ ) has been constrained using X-ray observations of galaxy clusters (Ettori et al., 2006; LaRoque et al., 2006; Allen et al., 2008). At the larger observable radius in X-ray data ( $\lesssim R_{500} \sim 1/2R_{200}$ ), these measurements indicate a gas mass fraction that is roughly 30 per cent lower than  $\Omega_b/\Omega_m$  inferred from WMAP 3-yr data (e.g. Spergel et al., 2007; McCarthy et al., 2007). Combining X-ray and SZ data allows to measure the gas fraction  $f_{\text{gas}}$  far away of the actual X-ray observations, out to  $R_{200}$ , and compare it with the primordial gas fraction. In this way, our current work aims at measuring the depletion parameter  $\mathcal{Y} = f_{\text{gas}}/(\Omega_b/\Omega_m)$  at various overdensity out to  $R_{200}$ , and to compare it with the value constrained from hydrodynamical numerical simulations (e.g. Ettori et al., 2004a; Frenk et al., 1999; Kravtsov et al., 2005; Gottlöber & Yepes, 2007). Precise observational measurements of  $\mathcal{Y}$  at  $R_{200}$  allow to address the baryon fraction issue in a new light, understanding the physical processes acting inside the clusters and possibly putting further constraints on  $\Omega_m$  and on other cosmological parameters.

**Investigating the systematics on observed results: towards a more realistic description of galaxy clusters** - When we deal with X-ray clusters we make some a-priori assumptions, like that of hydrostatic equilibrium, spherical geometry and the absence of substructures. Some of these assumptions have been tested through hydrodynamical numerical simulations (see Rasia et al., 2006, for a study of the systematics on the recovered mass profiles) or through a parametric combination of X-ray and Sunyaev-Zel'dovich effect measurements (see De Filippis et al., 2005, for a discussion of the systematics related to spherical assumption), but only for the inner regions of the clusters ( $\lesssim R_{500}$ ) accessible to X-ray observations. We are involved in a project in which we have acquired weak lensing measurements: the desired properties of clusters are then over-constrained by X-ray+SZ+lensing observations, providing critical insights to our understanding of clusters, and critical tests of current models for the formation and evolution of galaxy clusters. Extending the critical insights developed in Chapter 4, our goal is that to understand the goodness of the hydrostatic equilibrium assumption on the whole cluster, to infer which model of the DM coming from hydrodynamical numerical simulations better represents the data and provide constraints on the geometry of the sources.

We can then use these measurements as calibration of cluster masses at  $R_{200}$ , with

important implications in the use of galaxy clusters as cosmological probes.

# Appendix A

## A.1 Spectral deprojection technique

The deprojection technique decomposes the observed X-ray emission of the  $i$ -th annulus into the contributions from the volume fraction of the  $j$ -th spherical shells with  $j \leq i$ , by fixing the spectrum normalization of the outermost shell to the corresponding observed values. We can construct an upper triangular matrix  $\mathcal{V}_i^j$ , where the column vectors  $\mathcal{V}^1, \mathcal{V}^2, \dots, \mathcal{V}^n$  represent the “effective” volumes, i.e. the volume of the  $j$ -th shell contained inside the  $i$ -th annulus (with  $j \geq i$ ) and corrected by the gradient of  $n_e^2$  inside the  $j$ -th shell (see Appendix B for more detail), so as:

$$K_i \propto \int_{j \geq i} n_{e,j}^2 dV = \left( \mathcal{V} \# \vec{n}_e^2 \right)_i. \quad (\text{A.1})$$

In the previous equation  $\vec{n}_e \equiv (n_{e,1}, n_{e,2}, \dots, n_{e,n})$ , being  $n$  the total number of annuli, having internal (external) radius  $r_{\text{in},1}, r_{\text{in},2}, \dots, r_{\text{in},n}$  ( $r_{\text{out},1}, r_{\text{out},2}, \dots, r_{\text{out},n}$ ), with  $n \sim 15 - 40$ ;  $K_i$  is the MEKAL normalization of the spectrum in the  $i$ -th annulus; the operator # indicates the matrix product (rows by columns). Notice that the integral  $\int_{j \geq i} n_{e,j}^2 dV$  is of the order of the emission measure inside the  $i$ -th ring.<sup>1</sup> The inversion of this matrix allows us to determine  $n_{e,i}$ .

The values of  $K_i$  are obtained by rescaling by the observed number of counts in the  $i$ -th ring the faked *Chandra* spectrum with absorption, temperature and metallicity measured in that ring. The errors are computed by performing 100 Monte Carlo simulations of the observed counts. We pointed out that the uncertainties in the estimates of the projected temperature do not reflect into high systematic errors in the determination of  $K_i$ , because of the mild dependence on  $T$  of the cooling function  $\Lambda(T)$  integrated in the considered band (0.5 – 5 keV):  $\Lambda(T) \propto T^{-\alpha}$ , with  $0.1 \lesssim \alpha \lesssim 0.2$  for  $T \sim 7 - 12$  keV.

This approach is very powerful, because does not require any “real” spectral analysis, which could suffer of the poorness of the statistics and would need at least  $\sim 2000$  net counts per annulus: we can determine the projected density in annuli even with very small

---

<sup>1</sup>Hereafter we assume that the index  $j$  ( $i$ ) indicates the shell (ring) of the source of radius ( $r_{\text{in}}, r_{\text{out}}$ ).

counts ( $\sim 200 - 1000$ ). In other words we have an improvement (of about one order of magnitude) of the spatial resolution in the spectral analysis.

Concerning the temperature analysis, we have determined its value  $T_j$  in the  $j$ -th shell, by assuming analytic relations for the mass density profiles:  $\rho = \rho(\mathbf{r}, \mathbf{q})$ , where  $\mathbf{q} = (q_1, q_2, \dots, q_h)$  are suitable parameters. As discussed in Section 2.4, we consider two functional forms, a NFW profile with  $\mathbf{q} \equiv (c, r_s)$  and a RTM profile with  $\mathbf{q} = (x_s^*, r_{\text{vir}})$ .

We performed a spectral deprojection of the observed temperature  $T_{\text{shell}}^*$  in a set of  $n^*$  annuli with width much larger than the previous ones, with internal (external) radius  $r_{\text{in},1}^*, r_{\text{in},2}^*, \dots, r_{\text{in},n^*}^*$  ( $r_{\text{out},1}^*, r_{\text{out},2}^*, \dots, r_{\text{out},n^*}^*$ ) corresponding to the ones of the rings in which we have estimated the projected temperature (see Sect. 3.2.2), with  $n^* \ll n$  ( $n^* \sim 3 - 8$ ), so as to have at least 2000 counts per annulus. The deprojection method works in this way:

$$\vec{T}_{\text{ring},m}^* = \left( \mathcal{V}^* \# \left( \vec{T}_{\text{shell}}^* \cdot \vec{\epsilon}^* \right) \right)_{\text{m}} / L_{\text{ring},m}^*, \quad (\text{A.2})$$

where

the operator “ $\cdot$ ” indicates the product:  $\vec{T}_{\text{shell}}^* \cdot \vec{\epsilon}^* = (T_{\text{shell},1}^* \epsilon_1^*, T_{\text{shell},2}^* \epsilon_2^*, \dots, T_{\text{shell},n^*}^* \epsilon_{n^*}^*)$ . In eq.(A.2),  $\vec{\epsilon}^* = \mathcal{V}^{*-1} \# L_{\text{ring}}^*$  is the emissivity,  $\mathcal{V}^* = [\mathcal{V}^1, \mathcal{V}^2, \dots, \mathcal{V}^{n^*}]$ ,  $L_{\text{ring},m}^*$  is the luminosity of the  $m$ -th ring,<sup>2</sup> and the generic parameter  $\mathcal{P}^*$  has the same meaning as above, but it is evaluated in  $n^*$  annuli. The inversion of the matrix in eq.(A.2) allows us to finally estimate the deprojected temperature  $T_k^*$ .

We computed the theoretical temperature  $T_j$  by numerically integrating the equation of the hydrostatic equilibrium (eq. 3.1), assuming spherical geometry ( $\vec{r} \equiv r$ ). Then we constructed a grid of values for  $P_0$  and for the parameters  $\mathbf{q}$  entering the DM density profiles, so as  $T_j = T_j(\mathbf{q}, P_0)$ . In particular for  $P_0$  we have considered the range  $\hat{P}_0 - 3\sigma_{P_0} \leq P_0 \leq \hat{P}_0 + 3\sigma_{P_0}$ , where  $\hat{P}_0$  is the expectation value of  $P_0$ . So we can estimate the temperature  $kT_j(\mathbf{q}, P_0) = P(r)/n_{\text{gas}}(r)$ .

Since the temperature  $T_j(\mathbf{q}, P_0)$  obtained in this way is given on a set of  $n$  annuli with spatial resolution much better than the deprojected temperature  $T_{\text{shell},k}^*$  defined in the  $n^*$  annuli only, we perform a (gas mass-weighted) average to calculate the temperature  $T_k^{\text{ave}}(\mathbf{q}, P_0)$  in the  $k$ -th shell:

$$T_k^{\text{ave}}(\mathbf{q}, P_0) = \frac{\sum_{r_k \leq r_j < r_{k+1}} w_j T_j(\mathbf{q}, P_0) dV_j}{\sum_{r_k \leq r_j < r_{k+1}} w_j dV_j}, \quad (\text{A.3})$$

where  $w_j = n_j$  and  $dV_j$  represents the volume of the  $j$ -th shell, so as to reproduce a mass-weighted temperature. A  $\chi^2$ -minimization between  $T_k^{\text{ave}}(\mathbf{q}, P_0)$  and  $T_{\text{shell},k}^*$  (with error  $\sigma_{T_{\text{shell},k}^*}$ ),

$$\chi^2 = \sum_{k=1}^{n^*} (T_k^{\text{ave}}(\mathbf{q}, P_0) - T_{\text{shell},k}^*)^2 / \sigma_{T_{\text{shell},k}^*}^2 \quad (\text{A.4})$$

<sup>2</sup>Hereafter we assume that the index  $k$  ( $m$ ) indicates the shell (ring) having radius  $(r_{\text{in}}^*, r_{\text{out}}^*)$ .

provides us the best estimate of  $(\mathbf{q}, P_0)$ .

We also considered an alternative approach to determine  $(\mathbf{q}, P_0)$ . Following Mazzotta et al. (2004), we perform a weighted average of  $T_k(\mathbf{q}, P_0)$  to compute a projected spectral-like temperature  $T_{\text{proj},m}(\mathbf{q}, P_0)$  in the  $m$ -th ring to be compared with the observed temperature  $T_{\text{proj},m}^*$  of the  $m$ -th ring:

$$T_{\text{proj},m}(\mathbf{q}, P_0) = \left( \tilde{\mathcal{V}}^{\#} \left( T^{\text{ave}}(\mathbf{q}, P_0) \cdot \vec{w}(\mathbf{q}, P_0) \right) \right) / \mathcal{L}_{\text{ring},m}, \quad (\text{A.5})$$

where  $w_j = n_j^2 T_j^{-\alpha}(\mathbf{q}, P_0)$ ,  $\alpha = 3/4$ ,  $\vec{\mathcal{L}}_{\text{ring}}(\mathbf{q}, P_0) = \tilde{\mathcal{V}}^{\#} \vec{w}(\mathbf{q}, P_0)$ ;  $\tilde{\mathcal{V}}^{\#} = [\mathcal{V}^1, \mathcal{V}^2, \dots, \mathcal{V}^{n^*}, \mathcal{V}^{n^*+1}, \dots, \mathcal{V}^{n^*+h}]$  is an extension of the volume matrix  $\mathcal{V}^*$  which takes into account the contributions (up to a distance of 10 Mpc) coming from the  $h$  annuli external to  $R_{\text{spat}}$ . We have to use the following fitting function, which is a simplified of the functional form of Vikhlinin et al. (2005):

$$n_e(r) = \frac{n_0 (r/r_c)^{-\alpha} (1 + r^\gamma/r_s^\gamma)^{-\epsilon/\gamma}}{(1 + r^2/r_c^2)^{3/2\beta - \alpha/2}} \quad (\text{A.6})$$

with  $\gamma = 3$ , and (3.1) to extrapolate  $n_e(R)$ , the pressure and temperature in regions outside  $R_{\text{spat}}$ . Notice that the previous definition of temperature is a very powerful way to remove observational biases: in fact we are weighting different regions along the line of sight using different temperatures which are obtained by performing a spectral fit of a single-temperature model. With this approach we have a robust determination of the deprojected temperature profile. The best estimate of  $(\mathbf{q}, P_0)$  is obtained through a  $\chi^2$ -minimization between  $T_{\text{proj},m}(\mathbf{q}, P_0)$  and  $T_{\text{proj},m}^*$ :

$$\chi^2 = \sum_{m=1}^{n^*} \frac{(T_{\text{proj},m}(\mathbf{q}, P_0) - T_{\text{proj},m}^*)^2}{\sigma_{T_{\text{proj},m}}^2 + \sigma_{T_{\text{proj},m}}^2}. \quad (\text{A.7})$$

Here  $\sigma_{T_{\text{proj},m}}^2$  accounts for the statistical errors in eq.(3.1) coming from the measured errors for  $n_{\text{gas}}(r)$ . The reduced  $\chi^2$  resulting from this method is better than in previous case: this is likely due to the fact that the deprojected temperature  $T_{\text{shell}}^*$  strongly relies on assumptions, like spherical symmetry and uniform density profile, which are not completely satisfied in real clusters. Moreover the values of  $T_{\text{shell},k}^*$  are not independent: in fact we relate the deconvolved temperature, gas density and spectra normalization of the outermost shell to its observed values and then we compute the physical parameters in the  $m$ -th annulus by opportunely accounting for the contributions of the  $k$ -th shell ( $k \geq m$ ): this could propagate possible systematic errors from the external regions, where the determination of the physical properties cannot be so adequate because of the bad statistic. All the deprojected quantities presented in the present work refer to the second approach ( $T_{\text{proj}}$ ) only.

## A.2 Determining the Effective volume

Kriss et al. (1983) computed the geometrical volume of the  $j$ -th shell intercepted by the  $i$ -th annulus (with  $j \geq i$ ) as:

$$V_i^j = 4\pi \int_{r_{\text{in}_i}}^{r_{\text{out}_i}} dr r \int_{(r_{\text{out}_j}^2 - r^2)^{1/2}}^{(r_{\text{in}_j}^2 - r^2)^{1/2}} dz. \quad (\text{A.8})$$

Notice that when we use a geometrical volume to deproject the physical parameters (like the density as example) we are assuming that they are nearly constant in the shell. This introduces a systematic bias in the deprojected quantity, that tends to be increased when the gradient of the physical parameter is not negligible or when the rings are wide. McLaughlin (1999) partially corrected this bias by referring the density to an average radius,  $r_{\text{ave}} \equiv ((r_{\text{out}}^{3/2} + r_{\text{in}}^{3/2})/2)^{2/3}$ .

Here we introduce a new definition of the volume, the effective volume  $\mathcal{V}$ , which takes into account the real gradient of the physical parameters as a function of the radius. We assumed that we are weighting the unknown physical parameter  $\mathcal{P}$  in the  $j$ -th shell using a function  $w(R)$ , whose gradient is only due to the case of the squared density ( $w(R) \propto n_e^2$ ).

We have modeled the density inside the  $j$ -th shell as a local power-law,  $n(R) = n_{e,j} f(R)^{-\alpha}$ , where  $f(R) = (R/r_{\text{ref}_j})$ ,  $r_{\text{ref}_j} \equiv (r_{\text{in}_j} + r_{\text{out}_j})/2$ ,  $\alpha(R) = -\log(n^{j+1}/n^j)/\log(r_{\text{ref}_{j+1}}/r_{\text{ref}_j}) + O(\alpha)$ . We first calculated  $\alpha(R)$  by relying on the initial density obtained from the geometric volume-deprojection on a radius  $r_{\text{ref}_i}$ : in this way the introduced errors on  $\alpha$  are negligible ( $O(\alpha)$ ).

We define  $r$  as the projection of  $R$  on the sky plane, with  $R^2 = r^2 + z^2$ , being  $z$  the distance along the line of the sight. So, if  $n(r_{\text{ref}_j})$  is the density in the  $j$ -th shell, the observed parameter  $\mathcal{P}^*$  is related to the theoretical one by:

$$\begin{aligned} \vec{\mathcal{P}}^* &= \int dV \vec{\mathcal{P}} w(R) = \int dV \vec{\mathcal{P}} n_e^2(R) = \\ &= \left( \int dV f(R)^{-2\alpha} \right) \# \left( n_{e,j}^2 \vec{\mathcal{P}} \right) = \mathcal{V} \# \left( n_{e,j}^2 \vec{\mathcal{P}} \right). \end{aligned} \quad (\text{A.9})$$

So we can re-write the effective volume  $\mathcal{V}$  as:

$$\mathcal{V}_i^j = \int_{j \geq i} dV f(R)^{-2\alpha} = 4\pi \int_{r_{\text{in}_i}}^{r_{\text{out}_i}} dr r \int_{(r_{\text{out}_j}^2 - r^2)^{1/2}}^{(r_{\text{in}_j}^2 - r^2)^{1/2}} dz f(R)^{-2\alpha}. \quad (\text{A.10})$$

The effective volume  $\mathcal{V}_i^j$  is equal to the geometric one  $V_i^j$  if  $\alpha = 0$ , i.e. when we have negligible gradients of  $n(R)^2$  in the  $j$ -th shell. This is approximately true only in the case in which we have a good spatial resolution, for example when we consider  $n$  annuli ( $n \sim 15 - 40$ ) in the brightness image (see Section 3.2.3). But this is false when we have  $n^*$  annuli, with  $n^* \ll n$  ( $n^* \sim 3 - 8$ ) in the spectral analysis, for which a larger statistics (at least  $\sim 2000$  net counts per annulus) is required. In this last case, for example, it is possible to underestimate the true density in the external regions by 5 – 10 per cent by

using the geometrical volume instead of the effective one: this corresponds to set  $\vec{P}$  equal to  $I$  (being  $I$  the identity matrix) in eq.(A.9), and  $\vec{P}^* \propto K$  (see eq. A.1). The analysis we performed shows that the case in which adopting the effective volume is important is in eq.(A.2): using an effective volume can avoid to introduce systematic errors in the determination of the cluster masses.



# Appendix B

## B.1 Generating correlated random numbers in the Component-Wise Hastings sampler

We present a method to generate  $p$  random numbers with probability density function  $f = f(x_l, \mathbf{C}_{l,(l)})$ , i.e. with expectation value  $x_l$  and covariance  $\mathbf{C}_{l,(l)}$ , being  $\mathbf{C}$  the covariance matrix given by eqn. 5.11. This is useful to construct a proposal probability density function in the Component-Wise Hastings sampler. The general idea is to build  $p$  *correlated* random numbers taking into account their covariance. The covariance matrix  $\mathbf{C}$  can be diagonalized with a convenient change of reference system. Given a coordinates system  $\mathcal{X}$  which describes the  $p$  parameters under consideration, it is possible to work in a new reference system  $\mathcal{X}'$  described by the coordinate change matrix  $\mathcal{R}' = [\mathcal{R}^1, \mathcal{R}^2, \dots, \mathcal{R}^p]$ , being  $\mathcal{R}^1, \mathcal{R}^2, \dots, \mathcal{R}^p$  the eigenvectors of  $\mathbf{C}$ . In the system reference  $\mathcal{X}'$  the covariance matrix appears to be diagonal, i.e.  $\mathbf{C}' = \text{diag}(\sigma_1^{2'}, \sigma_2^{2'}, \dots, \sigma_p^{2'})$  with eigenvalues  $\sigma_1^{2'}, \sigma_2^{2'}, \dots, \sigma_p^{2'}$  and the  $p$  parameters are uncorrelated, so we can generate quite simply  $p$  *uncorrelated* random numbers to construct the proposal probability density function in  $\mathcal{X}'$ :  $f' = f'(x_l', \mathbf{C}')$ . To obtain the proposal probability density function  $f = f(x_l, \mathbf{C}_{l,(l)})$  in the coordinates system  $\mathcal{X}$  we use the following relation:

$$\mathbf{C} = \mathcal{R}' \# \mathbf{C}' \quad (\text{B.1})$$

being '#' the matrix product (rows per columns). In figure B.1 we present an example of application in the case of two variables.

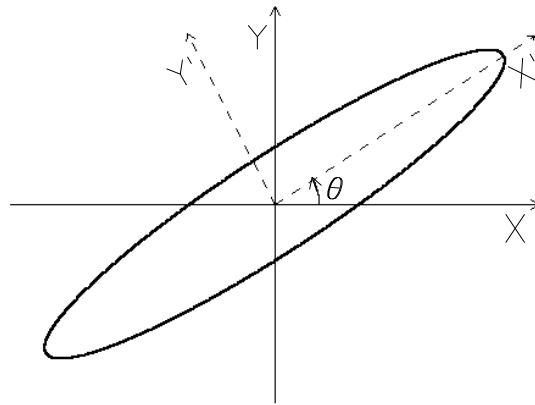


**Figure A-1.** Example of generation 2 *correlated* random variables. The ellipse represents the  $1\text{-}\sigma$  region of the proposal joint density function  $f = f(x_l, \mathbf{C}_{l,(l)})$ . The ellipse is rotated by an angle  $\theta$  (see figure) in the reference system  $\mathcal{X} = (X, Y)$ , with  $\tan(\theta) = \rho_{xy} \sigma_y / \sigma_x$ , being  $\rho_{xy}$  the correlation coefficient between the two variables  $x$  and  $y$ . In the reference system  $\mathcal{X}' = (X', Y')$  rotated of  $\theta$  with respect to  $\mathcal{X}$  the major and minor axes of the above ellipse are oriented along the cartesian axes, i.e. the two random variables  $x'$  and  $y'$  are *uncorrelated*. The eigenvectors of  $\mathbf{C}$  represent the rotation matrix of an angle  $\theta$  between  $\mathcal{X}$  and  $\mathcal{X}'$ .

## Bibliography

- Abell G. O., 1958, *ApJS*, 3, 211
- Akritas M. G., Bershadsky M. A., 1996, *ApJ*, 470, 706
- Allen S. W., Fabian A. C., 1998, *MNRAS*, 297, L57
- Allen S. W., Fabian A. C., 1997, in *Astronomical Society of the Pacific Conference Series*, Vol. 115, *Galactic Cluster Cooling Flows*, Soker N., ed., pp. 1–+
- Allen S. W., Rapetti D. A., Schmidt R. W., Ebeling H., Morris R. G., Fabian A. C., 2008, *MNRAS*, 383, 879
- Allen S. W., Schmidt R. W., Fabian A. C., 2001, *MNRAS*, 328, L37
- Anders E., Grevesse N., 1989, *GeCoA*, 53, 197
- Arnaud K. A., 1996, in *ASP Conf. Ser. 101: Astronomical Data Analysis Software and Systems V*, Jacoby G. H., Barnes J., eds., pp. 17–+
- Arnaud M., Pointecouteau E., Pratt G. W., 2005, *A&A*, 441, 893
- Astier P., et al., 2006, *A&A*, 447, 31
- Babul A., Balogh M. L., Lewis G. F., Poole G. B., 2002, *MNRAS*, 330, 329
- Bahcall N. A., Cen R., 1993, *ApJ*, 407, L49
- Bahcall N. A., Lubin L. M., 1994, *ApJ*, 426, 513
- Balestra I., Tozzi P., Ettori S., Rosati P., Borgani S., Norman V. M. C., Viola M., 2007, *A&A*, 462, 429
- Balogh M. L., Babul A., Patton D. R., 1999, *MNRAS*, 307, 463
- Balogh M. L., Pearce F. R., Bower R. G., Kay S. T., 2001, *MNRAS*, 326, 1228
- Benson B. A., Church S. E., Ade P. A. R., Bock J. J., Ganga K. M., Henson C. N., Thompson K. L., 2004, *ApJ*, 617, 829
- Bialek J. J., Evrard A. E., Mohr J. J., 2001, *ApJ*, 555, 597
- Birkinshaw M., 1999, *Phys. Rep.*, 310, 97
- Böhringer H., Matsushita K., Churazov E., Finoguenov A., Ikebe Y., 2004, *A&A*, 416, L21
- Böhringer H., Matsushita K., Churazov E., Ikebe Y., Chen Y., 2002, *A&A*, 382, 804
- Bonamente M., Joy M. K., LaRoque S. J., Carlstrom J. E., Reese E. D., Dawson K. S., 2006, *ApJ*, 647, 25

- Borgani S., 2004, *Ap&SS*, 294, 51
- Borgani S., Dolag K., Murante G., Cheng L.-M., Springel V., Diaferio A., Moscardini L., Tormen G., Tornatore L., Tozzi P., 2006, *MNRAS*, 367, 1641
- Borgani S., Finoguenov A., Kay S. T., Ponman T. J., Springel V., Tozzi P., Voit G. M., 2005, *MNRAS*, 361, 233
- Borgani S., Governato F., Wadsley J., Menci N., Tozzi P., Quinn T., Stadel J., Lake G., 2002, *MNRAS*, 336, 409
- Borgani S., Murante G., Springel V., Diaferio A., Dolag K., Moscardini L., Tormen G., Tornatore L., Tozzi P., 2004, *MNRAS*, 348, 1078
- Bower R. G., Benson A. J., Lacey C. G., Baugh C. M., Cole S., Frenk C. S., 2001, *MNRAS*, 325, 497
- Brighenti F., Mathews W. G., 2001, *ApJ*, 553, 103
- Brighenti F., Mathews W. G., 2006, *ApJ*, 643, 120
- Bryan G. L., 2000, *ApJ*, 544, L1
- Bryan G. L., 1999, *Comput. Sci. Eng.*, Vol. 1, No. 2, p. 46 - 53, 1, 46
- Bryan G. L., Norman M. L., 1998, *ApJ*, 495, 80
- Bullock J. S., Kolatt T. S., Sigad Y., Somerville R. S., Kravtsov A. V., Klypin A. A., Primack J. R., Dekel A., 2001, *MNRAS*, 321, 559
- Carlberg R. G., Yee H. K. C., Ellingson E., Morris S. L., Abraham R., Gravel P., Pritchet C. J., Smecker-Hane T., Hartwick F. D. A., Hesser J. E., Hutchings J. B., Oke J. B., 1997, *ApJ*, 485, L13+
- Carlstrom J. E., Holder G. P., Reese E. D., 2002, *ARA&A*, 40, 643
- Cavaliere A., Fusco-Femiano R., 1976, *A&A*, 49, 137
- Cavaliere A., Menci N., Tozzi P., 1998, *ApJ*, 501, 493
- Cavaliere A., Menci N., Tozzi P., 1999, *MNRAS*, 308, 599
- Cole S., Lacey C., 1996, *MNRAS*, 281, 716
- da Silva A. C., Kay S. T., Liddle A. R., Thomas P. A., 2004, *MNRAS*, 348, 1401
- Davis M., Peebles P. J. E., 1983, *ApJ*, 267, 465
- De Filippis E., Sereno M., Bautz M. W., Longo G., 2005, *ApJ*, 625, 108
- De Grandi S., Molendi S., 2002, *ApJ*, 567, 163
- De Grandi S., Etori S., Longhetti M., Molendi S., 2004, *A&A*, 419, 7

- De Grandi S., Molendi S., 2001, *ApJ*, 551, 153
- Diaferio A., Borgani S., Moscardini L., Murante G., Dolag K., Springel V., Tormen G., Tornatore L., Tozzi P., 2005, *MNRAS*, 356, 1477
- Dickey J. M., Lockman F. J., 1990, *ARA&A*, 28, 215
- Donahue M., Horner D. J., Cavagnolo K. W., Voit G. M., 2006, *ApJ*, 643, 730
- Donahue M., Voit G. M., O’Dea C. P., Baum S. A., Sparks W. B., 2005, *ApJ*, 630, L13
- Dos Santos S., Doré O., 2002, *A&A*, 383, 450
- Dressler A., 1980, *ApJ*, 236, 351
- Ettori S., De Grandi S., Molendi S., 2002, *A&A*, 391, 841
- Ettori S., Dolag K., Borgani S., Murante G., 2006, *MNRAS*, 365, 1021
- Ettori S., Tozzi P., Borgani S., Rosati P., 2004, *A&A*, 417, 13
- Ettori S., Borgani S., Moscardini L., Murante G., Tozzi P., Diaferio A., Dolag K., Springel V., Tormen G., Tornatore L., 2004a, *MNRAS*, 354, 111
- Evrard A. E., Henry J. P., 1991, *ApJ*, 383, 95
- Evrard A. E., Metzler C. A., Navarro J. F., 1996, *ApJ*, 469, 494
- Fabian A. C., 1994, *ARA&A*, 32, 277
- Fabian A. C., Nulsen P. E. J., Canizares C. R., 1991, *A&A Rev.*, 2, 191
- Fabian A. C., Sanders J. S., Allen S. W., Crawford C. S., Iwasawa K., Johnstone R. M., Schmidt R. W., Taylor G. B., 2003, *MNRAS*, 344, L43
- Finoguenov A., Reiprich T. H., Böhringer H., 2001, *A&A*, 368, 749
- Frenk C. S., White S. D. M., Bode P., Bond J. R., Bryan G. L., Cen R., Couchman H. M. P., Evrard A. E., Gnedin N., Jenkins A., Khokhlov A. M., Klypin A., Navarro J. F., Norman M. L., Ostriker J. P., Owen J. M., Pearce F. R., Pen U.-L., Steinmetz M., Thomas P. A., Villumsen J. V., Wadsley J. W., Warren M. S., Xu G., Yepes G., 1999, *ApJ*, 525, 554
- Gardini A., Rasia E., Mazzotta P., Tormen G., De Grandi S., Moscardini L., 2004, *MNRAS*, 351, 505
- Geman S., Geman D., 1990, *Stochastic relaxation, Gibbs distributions, and the Bayesian restoration of images*. Morgan Kaufmann Publishers Inc., San Francisco, CA, USA, pp. 452–472
- Giacconi R., Murray S., Gursky H., Kellogg E., Schreier E., Tananbaum H., 1972, *ApJ*, 178, 281

- Gilks W., Richardson S., Spiegelhalter D., 2003, *Markov Chain Monte Carlo in Practice*. Chapman & Hall, London
- Girardi M., Giuricin G., Mardirossian F., Mezzetti M., Boschin W., 1998, *ApJ*, 505, 74
- Gnedin N. Y., 1998, *MNRAS*, 294, 407
- Gottlöber S., Yepes G., 2007, *ApJ*, 664, 117
- Green P., 1995, *Reversible jump markov chain monte carlo computation and bayesian model determination*
- Gunn J. E., Hoessel J. G., Oke J. B., 1986, *ApJ*, 306, 30
- Hansen S. H., Piffaretti R., 2007, *A&A*, 476, L37
- Heymans C., et al., 2005, *MNRAS*, 361, 160
- Hoekstra H., Mellier Y., van Waerbeke L., Semboloni E., Fu L., Hudson M. J., Parker L. C., Tereno I., Benabed K., 2006, *ApJ*, 647, 116
- Ikebe Y., Böhringer H., Kitayama T., 2004, *ApJ*, 611, 175
- Itoh N., Kohyama Y., Nozawa S., 1998, *ApJ*, 502, 7
- Jones C., Forman W., 1984, *ApJ*, 276, 38
- Kaastra J. S., 1992, *An X-Ray Spectral Code for Optically Thin Plasmas (Internal SRON-Leiden Report, updated version 2.0)*
- Kaiser N., 1986, *MNRAS*, 222, 323
- Kaiser N., 1991, *ApJ*, 383, 104
- Kay S. T., Thomas P. A., Theuns T., 2003, *MNRAS*, 343, 608
- King I., 1962, *AJ*, 67, 471
- Kofman L. A., Gnedin N. Y., Bahcall N. A., 1993, *ApJ*, 413, 1
- Kotov O., Vikhlinin A., 2005, *ApJ*, 633, 781
- Kravtsov A. V., Nagai D., Vikhlinin A. A., 2005, *ApJ*, 625, 588
- Kriss G. A., Cioffi D. F., Canizares C. R., 1983, *ApJ*, 272, 439
- LaRoque S. J., Bonamente M., Carlstrom J. E., Joy M. K., Nagai D., Reese E. D., Dawson K. S., 2006, *ApJ*, 652, 917
- Levine R. A., Yu Z., Hanley W. G., Nitao J. J., 2005, *Computational Statistics & Data Analysis*, 48, 363
- Liedahl D. A., Osterheld A. L., Goldstein W. H., 1995, *ApJ*, 438, L115

- Lloyd-Davies E. J., Ponman T. J., Cannon D. B., 2000, MNRAS, 315, 689
- Loewenstein M., 2000, ApJ, 532, 17
- Lynden-Bell D., 1967, MNRAS, 136, 101
- MacKay D., 1997, Ensemble learning for hidden markov models
- Markevitch M., 1998, ApJ, 504, 27
- Massey R., Refregier A., Bacon D. J., Ellis R., Brown M. L., 2005, MNRAS, 359, 1277
- Mathiesen B. F., Evrard A. E., 2001, ApJ, 546, 100
- Maughan B. J., 2007, ApJ, 668, 772
- Maughan B. J., Jones L. R., Ebeling H., Scharf C., 2006, MNRAS, 365, 509
- Mazzotta P., Rasia E., Moscardini L., Tormen G., 2004, MNRAS, 354, 10
- McCarthy I. G., Bower R. G., Balogh M. L., 2007, MNRAS, 377, 1457
- McCarthy I. G., Babul A., Holder G. P., Balogh M. L., 2003a, ApJ, 591, 515
- McCarthy I. G., Holder G. P., Babul A., Balogh M. L., 2003b, ApJ, 591, 526
- Merritt D., Graham A. W., Moore B., Diemand J., Terzić B., 2006, AJ, 132, 2685
- Metzler C. A., Evrard A. E., 1994, ApJ, 437, 564
- Mohr J. J., Mathiesen B., Evrard A. E., 1999, ApJ, 517, 627
- Morandi A., Etori S., 2007, MNRAS, 380, 1521
- Morandi A., Etori S., Moscardini L., 2007, MNRAS, 379, 518
- Motl P. M., Hallman E. J., Burns J. O., Norman M. L., 2005, ApJ, 623, L63
- Muanwong O., Thomas P. A., Kay S. T., Pearce F. R., 2002, MNRAS, 336, 527
- Nagai D., 2006, ApJ, 650, 538
- Navarro J. F., Frenk C. S., White S. D. M., 1995, MNRAS, 275, 720
- Navarro J. F., Frenk C. S., White S. D. M., 1997, ApJ, 490, 493
- Navarro J. F., Hayashi E., Power C., Jenkins A. R., Frenk C. S., White S. D. M., Springel V., Stadel J., Quinn T. R., 2004, MNRAS, 349, 1039
- Neal R. M., 1993, Probabilistic inference using Markov chain Monte Carlo methods. Tech. Rep. CRG-TR-93-1, University of Toronto
- Nomoto K., Iwamoto K., Nakasato N., Thielemann F.-K., Brachwitz F., Tsujimoto T., Kubo Y., Kishimoto N., 1997, Nuclear Physics A, 621, 467

Norman M. L., Bryan G. L., 1999, in *Astrophysics and Space Science Library*, Vol. 240, Numerical Astrophysics, Miyama S. M., Tomisaka K., Hanawa T., eds., pp. 19–+

O’Shea B. W., Bryan G., Bordner J., Norman M. L., Abel T., Harkness R., Kritsuk A., 2004, *ArXiv Astrophysics e-prints*

Pearce F. R., Jenkins A., Frenk C. S., White S. D. M., Thomas P. A., Couchman H. M. P., Peacock J. A., Efstathiou G., 2001, *MNRAS*, 326, 649

Pearson T. J., Mason B. S., Readhead A. C. S., Shepherd M. C., Sievers J. L., Udomprasert P. S., Cartwright J. K., Farmer A. J., Padin S., Myers S. T., Bond J. R., Contaldi C. R., Pen U.-L., Prunet S., Pogosyan D., Carlstrom J. E., Kovac J., Leitch E. M., Pryke C., Halverson N. W., Holzzapfel W. L., Altamirano P., Bronfman L., Casassus S., May J., Joy M., 2003, *ApJ*, 591, 556

Peres C. B., Fabian A. C., Edge A. C., Allen S. W., Johnstone R. M., White D. A., 1998, *MNRAS*, 298, 416

Peterson J. R., Ferrigno C., Kaastra J. S., Paerels F. B. S., Kahn S. M., Jernigan J. G., Bleeker J. A. M., Tamura T., 2002, *ArXiv Astrophysics e-prints*

Piffaretti R., Jetzer P., Kaastra J. S., Tamura T., 2005, *A&A*, 433, 101

Ponman T. J., Cannon D. B., Navarro J. F., 1999, *Nat*, 397, 135

Ponman T. J., Sanderson A. J. R., Finoguenov A., 2003, *MNRAS*, 343, 331

Pratt G. W., Arnaud M., 2003, *A&A*, 408, 1

Pratt G. W., Arnaud M., 2005, *A&A*, 429, 791

Pratt G. W., Arnaud M., Pointecouteau E., 2006, *A&A*, 446, 429

Press W. H., Schechter P., 1974, *ApJ*, 187, 425

Press W. H., Teukolsky S. A., Vetterling W. T., Flannery B. P., 1992, *Numerical recipes in C. The art of scientific computing*. Cambridge: University Press, —c1992, 2nd ed.

Rasia E., Ettori S., Moscardini L., Mazzotta P., Borgani S., Dolag K., Tormen G., Cheng L. M., Diaferio A., 2006, *MNRAS*, 369, 2013

Rasia E., Mazzotta P., Borgani S., Moscardini L., Dolag K., Tormen G., Diaferio A., Murante G., 2005, *ApJ*, 618, L1

Rasia E., Tormen G., Moscardini L., 2004, *MNRAS*, 351, 237

Raymond J. C., Smith B. W., 1977, *ApJS*, 35, 419

Reiprich T. H., Böhringer H., 2002, *ApJ*, 567, 716

- Roncarelli M., Etori S., Dolag K., Moscardini L., Borgani S., Murante G., 2006, *MNRAS*, 373, 1339
- Rosati P., Borgani S., Norman C., 2002, *ARA&A*, 40, 539
- Rybicki G. B., Hummer D. G., 1978, *ApJ*, 219, 654
- Sánchez A. G., Baugh C. M., Percival W. J., Peacock J. A., Padilla N. D., Cole S., Frenk C. S., Norberg P., 2006, *MNRAS*, 366, 189
- Sarazin C. L., 1988, *Journal of the British Astronomical Association*, 98, 212
- Skilling J., 1998, *Probabilistic data analysis; an introductory guide*
- Snowden S. L., Mushotzky R. F., Kuntz K. D., Davis D. S., 2008, *A&A*, 478, 615
- Spergel D. N., et al., 2003, *ApJS*, 148, 175
- Spergel D. N., Bean R., Doré O., Nolta M. R., Bennett C. L., Dunkley J., Hinshaw G., Jarosik N., Komatsu E., Page L., Peiris H. V., Verde L., Halpern M., Hill R. S., Kogut A., Limon M., Meyer S. S., Odegard N., Tucker G. S., Weiland J. L., Wollack E., Wright E. L., 2007, *ApJS*, 170, 377
- Spitzer L., 1978, *Physical processes in the interstellar medium*. New York Wiley-Interscience, 1978. 333 p.
- Spitzer L., 1956, *Physics of Fully Ionized Gases*. Physics of Fully Ionized Gases, New York: Interscience Publishers, 1956
- Springel V., Hernquist L., 2002, *MNRAS*, 333, 649
- Springel V., Yoshida N., White S. D. M., 2001, *New Astronomy*, 6, 79
- Sunyaev R. A., Zeldovich Y. B., 1970, *Comments on Astrophysics and Space Physics*, 2, 66
- Tegmark M., et al., 2006, *Phys. Rev. D*, 74, 123507
- Tornatore L., Borgani S., Springel V., Matteucci F., Menci N., Murante G., 2003, *MNRAS*, 342, 1025
- Tozzi P., Norman C., 2001, *ApJ*, 546, 63
- Umstätter R., Christensen N., Hendry M., Meyer R., Simha V., Veitch J., Vigeland S., Woan G., 2005, *Phys. Rev. D*, 72, 022001
- Valageas P., Silk J., 1999, *A&A*, 350, 725
- Vikhlinin A., Kravtsov A., Forman W., Jones C., Markevitch M., Murray S. S., Van Speybroeck L., 2006, *ApJ*, 640, 691
- Vikhlinin A., Markevitch M., Murray S. S., Jones C., Forman W., Van Speybroeck L., 2005, *ApJ*, 628, 655

- Vikhlinin A., McNamara B. R., Forman W., Jones C., Quintana H., Hornstrup A., 1998, *ApJ*, 502, 558
- Voit G. M., 2005a, *Reviews of Modern Physics*, 77, 207
- Voit G. M., Bryan G. L., 2001, *Nat*, 414, 425
- Voit G. M., Bryan G. L., Balogh M. L., Bower R. G., 2002, *ApJ*, 576, 601
- Voit G. M., Donahue M., 2005, *ApJ*, 634, 955
- Voit G. M., Ponman T. J., 2003, *ApJ*, 594, L75
- Voit G. M., Kay S. T., Bryan G. L., 2005b, *MNRAS*, 364, 909
- White D. A., 2000, *MNRAS*, 312, 663
- White M., Hernquist L., Springel V., 2002, *ApJ*, 579, 16
- Wood-Vasey W. M., et al., 2007, *ArXiv Astrophysics e-prints*, astro-ph/0701041
- Wu K. K. S., Fabian A. C., Nulsen P. E. J., 2000, *MNRAS*, 318, 889
- Wu X.-P., Xue Y.-J., 2002, *ApJ*, 572, L19
- Wu X.-P., Xue Y.-J., Fang L.-Z., 1999, *ApJ*, 524, 22
- Yamada M., Fujita Y., 2001, *ApJ*, 553, L145
- Zwicky F., 1937, *ApJ*, 86, 217
- Zwicky F., Herzog E., Wild P., 1966, *Catalogue of galaxies and of clusters of galaxies*, Vol. 3. Pasadena: California Institute of Technology (CIT), —c1966
- Zwicky F., Kowal C. T., 1968, "Catalogue of Galaxies and of Clusters of Galaxies", Volume VI. "Catalogue of Galaxies and of Clusters of Galaxies", 1968, Volume VI Pasadena: California Institute of Technology, CGCG6

# List of Figures

2.1	.....	19
2.2	.....	24
2.3	.....	26
2.4	.....	28
2.5	.....	30
2.6	.....	32
3.1	.....	37
3.2	.....	41
3.3	.....	54
3.4	.....	54
3.5	.....	56
4.1	.....	64
4.2	.....	64
4.3	.....	70
4.4	.....	71
4.5	.....	72
4.6	.....	74
4.7	.....	75
5.1	.....	87
5.2	.....	96
5.3	.....	99
5.4	.....	100
5.5	.....	101
A-1	.....	116



# List of Tables

1.1	.....	14
3.1	.....	36
3.2	.....	38
3.3	.....	42
3.4	.....	48
3.5	.....	49
4.1	.....	63
4.2	.....	69



